

Simulated and Observed Transport Estimates Across the Overturning in the Subpolar North Atlantic Program (OSNAP) Sections

Gokhan Danabasoglu¹, Frederic S. Castruccio¹, Burcu Boza², Alice M. Barthel³, Arne Biastoch^{4,5}, Adam Blaker⁶, Alexandra Bozec⁷, Diego Bruciaferri⁸, Frank O. Bryan¹, Eric P. Chassignet⁷, Yao Fu^{9,10}, Ian Grooms¹¹, Catherine Guiavarc'h⁸, Hakase Hayashida¹², Andrew McC. Hogg¹³, Ryan M. Holmes¹⁴, Doroteaciro Iovino¹⁵, Andrew E. Kiss¹³, M. Susan Lozier⁹, Gustavo Marques¹, Alex Megann⁶, Franziska U. Schwarzkopf⁴, Dave Storkey⁸, Luke van Roekel³, Jon Wolfe³, Xiaobiao Xu⁷, Rong Zhang^{16,17}

- 1 US National Science Foundation (NSF) National Center for Atmospheric Research (NCAR),
10 Boulder, CO, USA
- 2 Eurasia Institute of Earth Sciences, Istanbul Technical University, Istanbul, Turkiye
- 3 US Department of Energy (DOE), Los Alamos National Laboratory (LANL), Los Alamos, NM,
USA
- 4 GEOMAR Helmholtz Centre for Ocean Research Kiel, Kiel, Germany
- 15 5 Kiel University, Kiel, Germany
- 6 National Oceanography Centre, Southampton, UK
- 7 Center for Ocean-Atmospheric Prediction Studies (COAPS), Florida State University,
Tallahassee, FL, USA
- 8 UK Met Office, Exeter, UK
- 20 9 School of Earth and Atmospheric Sciences, Georgia Institute of Technology, Atlanta, GA, USA
- 10 College of Marine Science, University of South Florida, St. Petersburg, FL, USA
- 11 Applied Mathematics Department, University of Colorado Boulder, Boulder, CO, USA
- 12 Application Laboratory, Japan Agency for Marine-Earth Science and Technology, Yokohama,
Japan
- 25 13 Research School of Earth Sciences and ARC Centre of Excellence for Climate Extremes,
Australian National University, Canberra, Australia
- 14 Australian Bureau of Meteorology, Sydney, Australia
- 15 Fondazione Centro Euro-Mediterraneo sui Cambiamenti Climatici (CMCC), Bologna, Italy
- 16 Program in Atmospheric and Oceanic Sciences, Princeton University, Princeton, NJ, USA
- 30 17 National Oceanic and Atmospheric Administration (NOAA) Geophysical Fluid Dynamics
Laboratory (GFDL), Princeton, NJ, USA

Correspondence: Gokhan Danabasoglu (gokhan@ucar.edu)

40

Abstract

A comparison of simulated and observed overturning transports and related properties across the Overturning in the Subpolar North Atlantic Program (OSNAP) sections for the 2014-2022 period is presented, considering both depth and density space transports. The effort was motivated by the observational transport estimates at both OSNAP-West (OW) and OSNAP-East (OE) sections which show a minor role for the Labrador Sea (LS) in setting the mean and variability of the overturning in the subpolar North Atlantic. There are 9 participating groups from around the world, contributing a total of 18 ocean – sea-ice simulations with 6 different ocean models. The simulations use a common set of interannually varying atmospheric forcing datasets. The horizontal resolutions of the simulations range from nominal 1° to eddy-resolving resolutions of 0.1° - 0.05° . While there are many differences between the simulations and observations as well as among the individual simulations in terms of transport properties, the simulations show significantly larger transports at OE than at OW in agreement with the observations. Analyzing overturning circulations in both depth and density space together provides a more complete picture of the overturning properties and features. This analysis also reveals that, in both the simulations and observations, northward and southward flows substantially cancel each other at a given depth or density, producing much smaller residual (total) transports. Such cancellations tend to be much more prominent in depth space than in density space. In general, the observed transport features are captured better at OE than OW. The simulations generally show larger (smaller) transports with positive (negative) temperature and salinity biases in the upper ocean near the OSNAP sections, but with no such relationship with density biases. In high-resolution simulations, the transport profiles agree better with the observations, but challenges remain in some other metrics considered in our analysis. When transports are calculated using a density referenced to 2000-m depth, rather than the ocean surface, the relative contributions of transports at OW increase modestly.

65

1 Introduction

70 The Atlantic Meridional Overturning Circulation (AMOC) depicts a simplified, zonally averaged
view of rather complex, three-dimensional circulation patterns of the Atlantic Ocean, connected
to the global circulation system primarily across the basin's southern boundary. Through its
associated heat, salt, and tracer (e.g., carbon) transports and their effects on the ocean state,
particularly on decadal-to-multi-decadal time scales, the AMOC has profound impacts on the
75 climate of the surrounding areas and on the global climate (see reviews by Buckley & Marshall,
2016; Sutton et al., 2018; Zhang et al., 2019; Jackson et al., 2022 and references therein). These
impacts mainly come about through spatial and temporal variations of sea surface temperatures
(SSTs). They include impacts on Atlantic hurricane activity, shifts in the Intertropical
Convergence Zone, precipitation changes over the Sahel and Amazon, changes in summertime
80 climate over North America and Europe, and other modes of climate variability – all with
significant societal and economic impacts. Furthermore, due to the presence of low-frequency
(decadal and longer) AMOC variability seen in many model simulations (e.g., Msadek et al.,
2010; Danabasoglu et al., 2012b), the AMOC is thought to represent a major component of
dynamical memory of the climate system, thus making its proper initialization – along with
85 associated (upper-ocean) heat content anomalies in the North Atlantic – important for decadal
climate prediction simulations (see Meehl et al., 2014 and references therein). Given all these
significant impacts, there is also a growing interest in how the AMOC will change in a warming
climate with many recent studies focusing on weakening as well as the stability and collapse of
the AMOC (e.g., Caesar et al., 2018; Caesar et al., 2019; Weijer et al., 2020; van Westen et al.,
90 2024).

In the absence of continuous and trans-basin observations prior to 2004, much of our knowledge
of the mean state, spatial and temporal variability, latitudinal coherency, and variability
mechanisms of the AMOC during the historical period comes from model simulations.

Unfortunately, models remain inconsistent in their representations of the mean AMOC and its
95 variability. For example, results from about 20 ocean model simulations forced with common,
interannually varying atmospheric datasets for the 1948-2007 period as part of the second phase
of the Coordinated Ocean-ice Reference Experiments (CORE-II; Large & Yeager, 2009; Griffies
et al., 2009) show a rather large range of mean AMOC transports in both depth- and density-

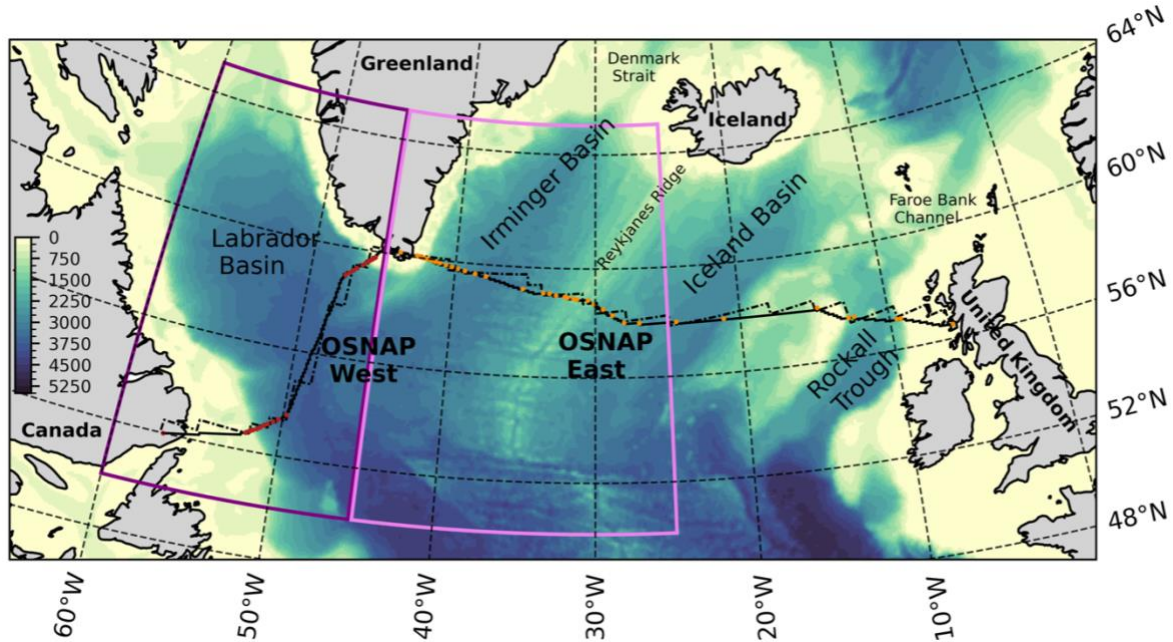
space, e.g., between ~ 5 and ~ 20 Sv at both 26.5° and 45°N in depth space (Danabasoglu et al.,
100 2014). There is a broad agreement among these simulations in their temporal depictions of
interannual-to-decadal variability and trends – despite significant differences in the spatial
structures of variability patterns – indicating that simulated variability and trends are largely
dictated by the imposed forcing (Danabasoglu et al., 2016). In both Danabasoglu et al. (2014)
and Danabasoglu et al. (2016), these AMOC differences among the simulations were attributed
105 to biases in the Labrador Sea (LS) region in upper-ocean potential temperature and salinity
distributions, mixed layer depths, and sea-ice cover. Similar inter-model differences in AMOC
properties are also seen in ocean reanalysis products for the historical period (Karspeck et al.,
2017; Jackson et al., 2019) even though each reanalysis ingests largely the same observational
datasets. In these products, differences arise due to insufficient observational data to constrain
110 the deep and abyssal oceans as well as the continental shelf regions. As such, the fidelity of the
underlying ocean model becomes as important as those used in free-running forced-ocean
simulations. Large inter-model differences in AMOC properties also exist in fully coupled
simulations participating in phases of the Coupled Model Intercomparison Project (CMIP; e.g.,
Cheng et al., 2013; Weijer et al., 2020; Bryden et al., 2024). Moreover, historical AMOC
115 variability and trends over recent decades do not necessarily agree with those from forced-ocean
simulations; the coupled simulations tend to show a somewhat stronger weakening that starts
earlier compared to the forced simulations (e.g., Danabasoglu et al., 2014; 2016; Cheng et al.,
2013; Xu et al., 2019, Weijer et al., 2020).

As discussed in Buckley & Marshall (2016), Zhang et al. (2019), Danabasoglu et al. (2019), and
120 references therein, interannual AMOC variability in model simulations is primarily dictated by
momentum fluxes, i.e., winds. In contrast, low-frequency AMOC variability is largely driven by
buoyancy fluxes at high latitudes of the North Atlantic. Specifically, a large majority of model
simulations identify deep water formation regions – usually determined by deep mixed layers –
as important regions linked to downstream AMOC variability. In many simulations, the
125 associated low-frequency variability mechanism involves surface buoyancy flux anomalies
primarily over the LS region, but also with contributions over the Irminger Sea, that arise from
long episodes of the positive phase of the North Atlantic Oscillation (NAO). These anomalies
contribute to positive upper-ocean density anomalies and subsequent deepening of mixed layers,
followed by downstream AMOC intensification, after a few years (see, e.g., Ortega et al., 2021;

130 Sidorenko et al., 2021; and above references). Evidence for such a prominent role for the LS in
low-frequency AMOC variability includes the finding that the LS remains the only active deep
water formation region after low-pass filtering of mixed layer depths (Danabasoglu, 2008), and
that low-frequency AMOC variability can be reproduced just by imposing NAO-related
buoyancy flux anomalies over the LS region (Yeager & Danabasoglu, 2014). Furthermore,
135 analysis of eddy-permitting / -resolving model simulations continue to show the LS as a key
region on decadal time scales. For example, through sensitivity experiments with spatially
refined surface forcing, Böning et al. (2023) conclude that the Irminger Sea deep water comes
from the LS region and that AMOC decadal variability is governed by the LS convection,
especially during exceptionally cold winters. This conclusion is consistent with Yeager et al.
140 (2021) who find a disproportionately large role for the LS in AMOC decadal variability.
Specifically, despite a weak mean surface diapycnal transformation, multidecadal AMOC
variability can be traced to anomalous production of dense LS Water, with buoyancy forcing in
the western subpolar gyre playing a substantial driving role. A caveat here is that models have
many biases in the North Atlantic, including potential over-production of the LS Water (Li et al.,
145 2019) and failure to adequately represent the dense water overflows from the Nordic Seas
(Danabasoglu et al., 2010). We also note that low-frequency variability associated with water
mass formations in the Greenland-Iceland-Norwegian Seas and the Arctic Ocean can impact
downstream AMOC variability (Zhao et al., 2024).

While there have been intermittent and regionally confined measurements of the AMOC or its
150 contributors at several latitudes as well as inferences from hydrographic sections (e.g., Larsen &
Sanford, 1985; Bryden et al., 2005; Toole et al., 2011; Meinen et al., 2010; Send et al., 2011),
continuous, trans-basin, and comprehensive observational efforts have gained momentum only
during the last couple of decades. The RAPID Meridional Overturning Circulation and Heat-flux
Array at 26.5°N is the first such observational program providing AMOC measurements since
155 2004 (Cunningham et al., 2007). The South Atlantic MOC Basin-wide Array (SAMBA) at
34.5°S has been operational since 2009, but it has a gap during roughly the 2011-2013 period
(Meinen et al., 2018) and a large uncertainty due to the highly variable Malvinas and Agulhas
systems. The Overturning in the Subpolar North Atlantic Program (OSNAP) array at
approximately 57°N (Fig. 1) is the third trans-basin observational effort that has been providing
160 data since August 2014 (Lozier et al., 2017). OSNAP fills a crucial missing observational piece

focusing on the northern North Atlantic, a region identified as an important source of low-frequency, buoyancy-driven AMOC variability with deep water formation areas (again see reviews by Buckley & Marshall, 2019 and Zhang et al., 2019).



165 *Figure 1.* OSNAP sections. The red and orange dots indicate the locations of the moorings at OSNAP-West and OSNAP-East, respectively. The dot-dash and solid black lines show the closest model grid lines through the OSNAP mooring locations based on the NCAR1 and NCAR10 grids, respectively (see Appendix A7). Model bathymetry from NCAR10 is also shown in color (in m). The dark and light purple boxes indicate the Labrador Sea (left) and the Irminger Sea (right) regions, respectively, used in bias analysis.

170 OSNAP observations, by design, provide estimates of overturning transport magnitudes for the LS and the eastern subpolar gyre side separately. Now available for the 8-year period from August 2014 to July 2022 (Fu et al., 2025), these observations show that conversion of warm and salty upper-ocean Atlantic waters into colder and fresher deep waters primarily occurs in the eastern subpolar gyre side, dominating both the mean and seasonal variability of the overturning
 175 circulation (Lozier et al., 2019; Li et al., 2021; Lozier, 2023; Fu et al., 2023). Thus, OSNAP observations reveal a minor role for the LS during this period in stark contrast with numerous modeling studies which connect deep water formation in the LS to downstream low-frequency AMOC variability. While a few earlier studies (Spall, 2004; Straneo, 2006; Pickart & Spall,

2007) also argued for a minor role for the LS in AMOC variability, OSNAP observations provide
180 the most compelling evidence to date with direct comparisons of transport estimates at both
OSNAP west and east sections. As alluded to above, a caveat here is that most modeling studies
typically focus on the role of the LS on decadal-to-multi-decadal time scales, whereas OSNAP
observational record is still too short to provide guidance on these longer time scales.

This finding regarding differences in the role of the LS between the OSNAP observations and the
185 long-standing view from model simulations has sparked vast interest in the scientific community
during the last few years. Published studies make use of observational datasets, both forced
ocean-only and coupled model simulations (including at eddy-rich resolutions), and ocean and
atmosphere reanalysis products – or their combinations. They primarily focus on the locations of
190 these waters with the downstream AMOC, considering the recent OSNAP period. Among these,
several studies identify the Irminger Sea or the broader eastern subpolar gyre as having the
strongest AMOC-related variability (e.g., Petit et al., 2020; Menary et al., 2020; Sidorenko et al.,
2020; Megann et al., 2021; Chafik et al., 2022; Fu et al., 2024), consistent with observations.
However, the ultimate sources of these deep waters and their variability remain unsettled. For
195 example, Petit et al. (2020) argue that local buoyancy fluxes over these basins mostly account for
these dense waters of the subpolar North Atlantic. This view is also supported in a recent study
by Fu et al. (2024) which shows that the overturning at the eastern part of OSNAP is
significantly correlated with water mass transformation forced by surface buoyancy forcing in
the Irminger and Iceland basins. Chafik et al. (2022) also indicates the Irminger Sea as the center
200 of action for subpolar AMOC variability, arguing that the NAO is the main driving mechanism
for Irminger Sea density variations on multiple time scales. However, this study finds no clear
connections between the Irminger Sea density variations and atmospheric heat losses but instead
finds that waters dominating the central Irminger Sea are cooled in the first place in the LS and
advected into the Irminger Sea. Thus, an alternative interpretation of findings of this study could
205 be that the Irminger Sea AMOC variability has its origins in the LS through direct local water
mass transformation via surface buoyancy fluxes in the LS. In another study, Menary et al.
(2020) assert that density anomalies generated by surface forcing in the Irminger Sea propagate
into the LS, where they dominate the density variability. More recently, Petit et al. (2023)
identify the LS as a key pathway for upper North Atlantic Deep Water with its waters sourced

210 from the eastern subpolar gyre, but undergoing further densification within the LS. We finally
note that using observational and reanalysis datasets, Zou et al. (2020) and Lozier (2023) show
that due to substantial compensation of thermal and saline anomalies, the volume of newly
formed dense waters exported out of the LS is relatively small over the observational period.

As indicated earlier, model fidelity remains a challenge with substantial biases in the northern
215 North Atlantic (e.g., Danabasoglu et al., 2016). The model representations of diapycnal mixing,
the Nordic Seas overflows, complex flow pathways, and local recirculations are found to be
important contributing factors that impact model biases (e.g., Lozier et al., 2022; Buckley et al.,
2023; Lozier, 2023). Some of these processes are represented in closer agreement with
observations in high-resolution models compared to their low-resolution counterparts (Hirschi et
220 al., 2020). Using the OSNAP observations, Li et al. (2021) show that while both the Labrador
Current and West Greenland Current exhibit large density anomalies, these anomalies are
strongly correlated, resulting in only modest variability for overturning in the LS. Accurately
representing such correlations; temperature, salinity, and current properties, along with their
pathways, with minimal departures from observations is a rather high bar for both low- and high-
225 resolution ocean models to achieve. Indeed, Jackson & Petit (2022) find that models with a more
saline LS tend to produce stronger water formation in this region, with correspondingly stronger
connections with downstream AMOC. Nevertheless, they conclude that coupled models analyzed
in their study are generally in good agreement with the OSNAP transport observations.

In the present study, we take a step back and provide a basic, yet much-needed evaluation of
230 simulated transports against OSNAP observations for the 2014-2022 period using a large set of
forced ocean – sea-ice (FOSI) simulations. Our effort aims to produce an assessment of model
fidelity as well as a benchmark for simulated transports and related properties at the OSNAP
sections in comparison to these observations. The simulations largely follow the Ocean Model
Intercomparison Project (OMIP) protocol (Griffies et al., 2016; Tsujino et al., 2020) and are
235 forced using the atmospheric datasets based on the Japanese Atmospheric Reanalysis product,
suitably adjusted to run such FOSI experiments (JRA55-do; Tsujino et al., 2018). This protocol is
intended to provide a controlled and coordinated framework to evaluate ocean components of
coupled models that participate in CMIPs (Griffies et al., 2009; Danabasoglu et al., 2014). There
are 9 participating groups / centers from around the world, contributing a total of 18 simulations
240 with 6 different ocean models in this study. The horizontal resolutions of the simulations range

from nominal non-eddy-resolving 1° to eddy-resolving resolutions of 0.1° - 0.05° . Thus, a goal is to assess how the representation of overturning transports at OSNAP changes with model horizontal resolution. The transports are evaluated in depth, σ_0 , and σ_2 spaces – in the latter two, potential densities are referenced to the surface and 2000-m depth, respectively. The present manuscript is largely descriptive. We mainly provide a catalog of model solutions; detailed analyses of individual model results and specific reasons for their differences from and similarities to the observations are not fully covered here. However, an analysis of water mass formations and transformations will be presented in a separate subsequent study. Finally, we note that because the observational record is short, we cannot yet address the relative roles of the LS vs. the eastern subpolar gyre in AMOC variability on decadal and longer time scales. An analysis of such low-frequency variability and its relationship to shorter timescale variability in these simulations in comparison to available observations in the northern North Atlantic is the subject of a separate ongoing study.

The manuscript is organized as follows. In Sect. 2, we summarize the OSNAP observing system, model simulations and the forcing datasets, how the transport lines are determined, and how the AMOC is calculated in depth and density space. We then present results for transport timeseries in Sect. 3; time-mean transports in σ_0 space in Sect. 4; time-mean transports in depth and σ_2 space in Sect. 5; transport variability in Sect. 6; temperature and salinity diagrams in Sect. 7; and temperature, salinity, and density biases in Sect. 8. We provide a summary and our conclusions in Sect. 9. Brief model descriptions are given in Appendix A.

2 Observational Data, Participating Models, Forcing, and Methods

2.1 OSNAP Observing System

The OSNAP observing system is designed to provide a continuous record of the full-water column, trans-basin transports of volume, heat, and freshwater in the subpolar North Atlantic (Lozier et al., 2017). It consists of two sections: OSNAP-West, which runs from the southeastern Labrador shelf to the southwestern tip of Greenland, and OSNAP-East, which runs from the southeastern tip of Greenland to the Scottish Shelf (Fig. 1). We will refer to these sections as OW and OE, respectively. OSNAP uses a combination of ~ 60 fixed moorings located at the continental boundaries and on both sides of the Reykjanes Ridge to obtain direct measurements

270 of velocities at the boundaries, and geostrophic and Ekman flows in the interior to estimate
meridional volume transports. In regions of complex topography, the moored arrays were
supplemented by glider surveys in the early part of the OSNAP observational period. The
gridded temperature and salinity data represent a combination of data from Argo floats in the
upper 2000 m; moorings; ship-based Conductivity-Temperature-Depth (CTD) sections for
275 regions below 2000 m without mooring observations; gliders for the Hatton-Rockall Basin; and
World Ocean Atlas monthly climatology for shallow coastal waters without data from moorings
and Argo (Li et al., 2017). The data are objectively mapped to the OSNAP sections with a 20-m
resolution in the vertical and a nominal 0.25° horizontal resolution with the original mooring
positions preserved. The OSNAP record has been recently extended to 8 years, covering the
280 August 2014 – July 2022 period (Fu et al., 2025). We refer to the OSNAP observational data
simply as OSNAP.

2.2 Models

We use 18 simulations from 9 groups run with 6 different models as summarized in Table 1. The
ocean models are the HYbrid Coordinate Ocean Model (HYCOM), the Modular Ocean Model
285 version 5 (MOM5) and version 6 (MOM6), the Model for Prediction Across Scales – Ocean
(MPAS-O), the Nucleus for European Modelling of the Ocean (NEMO), and the Parallel Ocean
Program version 2 (POP2), which are coupled to a variety of sea-ice models (see Appendix A).
The horizontal resolutions range from non-eddy-resolving resolutions of near 1° to eddy-
permitting and eddy-resolving resolutions of 0.25° - 0.05° . We denote each simulation using the
290 acronym of the group which produced the simulation followed by the nominal horizontal
resolution of a simulation in degrees. For example, NCAR1, NCAR67, and NCAR10 refer to
simulations performed by the NCAR group, using nominal 1° , 0.67° , and 0.10° horizontal
resolution, respectively. With respect to their vertical coordinates, while many of the simulations
use depth / level coordinates, a few simulations employ hybrid coordinates. Both z and z^*
295 formulations are utilized in the simulations with depth coordinates where the z^* approach
enables inclusion of large amplitude variations of the sea surface by distributing such changes
over the full water column depth (Adcroft & Campin, 2004). The number of vertical levels /
layers varies from 36 in FSU08 to 98 in CMCC06 with most models using between 46-75, with
varying placement of levels in the vertical, usually with finer resolution near the surface. Both to

300 isolate the impacts of horizontal resolution and to help reduce crowding in some of the figures,
we separate the simulations into three groups: low resolution (LR); medium resolution (MR);
and high resolution (HR). The LR group includes 5 simulations with resolutions of
approximately 1° , i.e., ANU1, FSU72, NCAR1, NCAR67, and NOC1. The MR set has 7
305 GFDL25, NOC25, and UKMO25. Finally, the HR set has the remaining 6 simulations with
resolutions of 0.1° or finer, i.e., ANU10, CMCC06, FSU08, GEOMAR05, NCAR10, and
NOC08. Brief descriptions of the models along with their configurations, parameter settings, and
references, if available, presenting evaluations of their simulations are provided in Appendix A.

2.3 Forcing Datasets

310 The FOSI simulations largely follow the OMIP protocol. They are forced with the atmospheric
datasets based on the Japanese Atmospheric Reanalysis product (JRA55; Kobayashi et al., 2015)
which were adjusted extensively to correct for biases in the reanalysis and for obtaining
reasonably balanced heat and freshwater budgets (Tsujino et al., 2018). This adjusted dataset,
referred to as JRA55-do, has a spatial resolution of 55 km with a temporal resolution of 3 hr.
315 Except for the runoff dataset, all the fields are directly from the reanalysis product, thus
representing a rather self-contained forcing dataset for the 1958-2023 period. The heat,
freshwater, and momentum fluxes needed to force the simulations are based on the bulk formulae
described in Large & Yeager (2004) and Large & Yeager (2009). We note that the OMIP protocol
was formally introduced in Griffies et al. (2016) which used the CORE-II datasets – now referred
320 to as OMIP phase 1. The protocol was later updated slightly when used with the JRA55-do
datasets and it was designated as OMIP phase 2. The simulations here follow this phase 2
approach which we simply refer to as OMIP.

The simulations apply restoring of sea surface salinity (SSS) to an observed monthly-mean
climatology. This is because FOSI simulations do not have many of the feedbacks that exist in
325 fully coupled systems with an active atmosphere, as discussed in Griffies et al. (2009) and
Danabasoglu et al. (2014). Moreover, the lack of any appreciable local feedbacks between
surface freshwater fluxes and SSS can lead to unrealistic salinities locally, mostly due to biases
in precipitation. Usually, the upper 10-m average monthly salinity climatology from the World
Ocean Atlas version 2 (WOA13; Zweng et al., 2013; Boyer et al., 2015) is used as the restoring

330 field. The OMIP protocol does not prescribe a particular restoring procedure, and the modeling
groups can choose their optimal restoring strength based on how their models represent several
key features in comparison to available observations, such as the transport and time evolution of
the AMOC to ensure that it does not get too weak or collapse. Usually SSS restoring is applied
globally, including ice covered regions, and its global mean is subtracted to ensure that the
335 restoring term does not impact the global salt content. The SSS restoring approaches and
strengths used by the participating groups are presented in Table 2.

The OMIP protocol calls for multi-century-long simulations forced with repeat cycles – usually 5
to 6 – of the forcing datasets. While an intent is to achieve quasi-equilibrated solutions to the
extent possible, this approach has a few drawbacks. One is that the repeat cycle introduces an
340 unphysical jump in forcing from the last year of a particular cycle (e.g., 2023) back to the first
year of the subsequent cycle (e.g., 1958). So, at the beginning of the next cycle, the ocean initial
state reflects that of year 2023 instead of year 1958. Consequently, it is not recommended to use
the first 15-20 years of a forcing cycle in any analysis. Second, even with multiple cycles, the
degree of repeatability of solutions from one cycle to the next is both model and variable
345 dependent (e.g., Danabasoglu et al., 2014). Third, such long simulations are usually not
affordable for HR simulations.

As detailed in Appendix A, the simulations do not strictly follow the OMIP protocol for various
reasons that include which end year was available for forcings when the simulations started.
Many simulations use a slightly shorter forcing period for the cycles before the very last cycle.
350 For example, ANU1 and ANU25 simulations go for 6 forcing cycles where the first 5 cycles use
the 1958-2018 period, and the simulations were extended to the end of 2022 only for the last
cycle. Similarly, NCAR1 and NCAR10 simulations use the 1958-2018 period for the first 4
cycles and have the last (5th) cycle extended to the end of 2023. Due to the computational costs,
most of the HR simulations are integrated only for 1 forcing cycle. In summary, the participating
355 simulations have been integrated for a range of 1 to 6 forcing cycles.

These differences in simulation lengths as well as limited availability of datasets only for specific
forcing cycles for some simulations certainly present challenges for our analysis. However,
because our analysis concerns the last decade of a forcing cycle, cycle-to-cycle differences in
overturning transports are relatively small during the last decade compared to those of the earlier

360 periods (not shown). Therefore, we are confident that use of different cycles from the participating simulations does not impact our general conclusions. Noting that we analyze the same forcing cycles for a given LR and HR set of simulations from the same group except for ANU, we use the following cycles for each simulation: cycle 1 for CMCC25, CMCC06, FSU72, FSU08, GEOMAR25, GEOMAR05, NCAR67, NOC1, NOC25, NOC12, and UKMO25; cycle 4
365 for ANU10; cycle 5 for E3SM27, NCAR1, and NCAR10; and cycle 6 for ANU1, ANU25, and GFDL25.

As indicated in Sect. 2.1, the OSNAP observations cover the August 2014 – July 2022 period. For ease of analysis, we use the full 2014 – 2022 period for model simulations. For E3SM27, GFDL25, and NCAR67, we use shorter periods from 2014 to their respective simulation end
370 years, i.e., 2020, 2018, and 2018, respectively. Finally, we employ monthly mean fields for both OSNAP and model simulations as this temporal frequency is what is available from all model simulations. Compared to use of higher frequency sampling, e.g., instantaneous, in transport calculations if they were to be available, we do not expect our results to change in any significant way for the spatial scales considered here, supported by the findings of Ballarotta et al. (2013)
375 for transport calculations in an eddy-permitting regime in the Southern Ocean.

2.4 Transport Lines

The OSNAP array is not aligned with a latitude line or models' grid lines, requiring a careful method to extract the model outputs along the OE and OW lines. For this purpose, we developed a tool to obtain the best or closest model *broken grid line* through the OSNAP mooring locations
380 for each participating model. The tool returns the grid indices along the line. These indices are then used to index a Python Xarray to extract the desired fields along this broken line for each simulation. As such, the tool provides direct access to the simulated fields across the OSNAP sections, without requiring any interpolations. As an example, the solid and dot-dash black lines in Fig. 1 show the best broken grid lines for NCAR10 and NCAR1, respectively. Because these
385 lines follow a model's grid, both zonal and meridional velocity components are used in transport calculations depending on whichever component is normal to the local grid line. We note that we chose to use this approach based on the actual simulation outputs to calculate transports instead of extracting the sections strictly following the OSNAP observation grid for two reasons. First, it is a straightforward approach, providing the actual transport simulated by each model. Second,

390 comparisons of both methods using NCAR simulations produced very similar results (not shown), providing justification for our approach.

2.5 Calculation of AMOC

The overturning streamfunction ψ is commonly calculated in both depth and density space using the following equations:

395

$$\psi(y, z, t) = - \int_{z_b}^{z'} \int_{x_w}^{x_e} v(x, y, z, t) dx dz',$$

$$\psi(y, \sigma, t) = - \int_{\sigma_b}^{\sigma'} \int_{x_w}^{x_e} v(x, y, \sigma, t) \frac{\partial z}{\partial \sigma} dx d\sigma',$$

400 where v is the plane-normal velocity, positive northwards; t is time; z is the vertical coordinate, positive upwards; x is the zonal coordinate, positive eastwards; y is the meridional coordinate, positive northwards; and σ is sigma density, either in σ_0 or σ_2 , defined as $(\rho - 1000)$ in kg m^{-3} where ρ is the seawater density. The subscripts e and w denote the eastern and western limits, respectively, of the zonal integral; the subscript b represents bottom, meaning that the
405 integrations are performed from bottom up, e.g., from the highest density in density space; and $\partial z / \partial \sigma$ is the isopycnal thickness. In these equations, v is in m s^{-1} and the lengths are in m. Thus, the transports are in $\text{m}^3 \text{s}^{-1}$, displayed in Sv ($= 10^6 \text{ m}^3 \text{ s}^{-1}$). With the sign convention used in the above equations, the negative and positive profile slopes indicate poleward and equatorward transports, respectively, in the overturning plots presented here. In our transport calculations, we
410 only use the resolved-flow velocities, i.e., the relatively small parameterized contributions are not included. We note that the bottom-up integration method used here is usually adopted in the modeling community to compute overturning transports, because the boundary condition at the bottom, i.e., a zero transport, is known. This approach, however, is in contrast with the top-down approach employed in the OSNAP observational estimates (e.g., Lozier et al., 2019). So, we
415 expect some small differences between our transport values and those published for OSNAP observations, but all our transports here are consistently calculated using the same bottom-up approach, including for OSNAP.

Overturning in density space directly connects with diapycnal water mass transformation. However, in both depth and density space, there are substantial cancellations of northward and southward flows at constant depth and density, respectively. We believe that analyzing the AMOC in both depth and density space provides complementary information – an approach also advocated by Lozier et al. (2019) and Zhang & Thomas (2021). Therefore, in our analysis here we apply both methods.

For depth-space analysis, we use each model’s native vertical discretization. For density-space analysis, we employ common density ranges and bin increments across all simulations. Specifically, σ_0 calculations are referenced to the ocean surface, and they use a density range of 24.0-28.5 kg m⁻³ with 105 density bins. The bin increments are 0.1 and 0.02 kg m⁻³ for densities less and greater than 27.0 kg m⁻³, respectively. σ_2 calculations use a reference depth of 2000 m. The density range is between 28.0 and 38.0 kg m⁻³. We use 85 bins with increments of 0.2 kg m⁻³ for 28.0-35.0 kg m⁻³, 0.1 kg m⁻³ for 35.0-36.0 kg m⁻³, and 0.05 kg m⁻³ for densities > 36.0 kg m⁻³. Also, for consistency across all simulations, we use monthly-mean potential temperature and salinity to calculate densities using the TEOS-10 equation of state (McDougall & Barker, 2011).

As discussed in Lynn & Reid (1968), there is no single potential density that can be used for all purposes. While σ_0 is useful to connect surface water mass transformations to deeper overturning transports, it does not necessarily depict an accurate representation of transports at depth because it ignores the pressure effects on density. Indeed, especially in the northern North Atlantic, potential density referenced to 4000-m depth, i.e., σ_4 , may be more appropriate. In this study, we adopt use of σ_2 as a compromise, but we also think that it is more suitable for our purposes as we focus on transports primarily between 1000 – 3500 m. Thus, effects of pressure on density and transports are appropriately included. σ_0 is employed to expedite comparisons with observations.

In OSNAP, a zero-net-mass (actually volume) transport constraint across the entire section is enforced (Lozier et al., 2019). Specifically, a mean southward transport of 1.6 Sv across OW – intended to represent long-term transport measurements across the Davis Strait – is compensated by an equivalent northward transport at OE. This is accomplished through an a posteriori application of a spatially uniform, but time dependent compensation velocity. In this approach, there is no transport into the Arctic Basin associated with the flow into the Arctic Ocean through the Bering Strait. Lozier et al. (2019) report that the OSNAP transports change very little when

450 this flow is accounted for. Therefore, when computing the simulated transports, we do not impose any constraints. As such, any non-zero transports at the surface reflect the flows in and out of the Arctic Basin associated with the Bering Strait Throughflow. We note that in most of our plots we use a lower limit for density and do not show near surface or upper-ocean transports.

455 These transport calculations employ a version of the Python-based Meridional ovErTurning DiagnostIC (METRIC) Package (Castruccio, 2021). METRIC enables consistent calculations of observed and simulated AMOC estimates at various observational sites in the Atlantic Ocean. The package can be used with different ocean models at various resolutions, and it includes a few additional, alternative approaches to calculate these transports.

3 Transport Timeseries

460 We start with the time evolution of transport profiles in depth space presented in Fig. 2 as transports per unit depth, i.e., in Sv m^{-1} . The OSNAP profiles are based on the gridded velocity datasets, and profiles only from NCAR10 and NCAR1 are shown as examples of model simulations for brevity. The OSNAP profiles at both sites exhibit a rather streaky behavior, primarily due to the methodology used to estimate basin interior geostrophic transports, which are derived from full-depth dynamic height moorings bracketing the basin interior. Temperature and salinity measurements on these moorings are typically hundreds of meters apart vertically. In general, transport magnitudes and the depth ranges of northward and southward transports are in better agreement between OSNAP and NCAR10, particularly at OE, than with NCAR1. The latter shows a very prominent, deeper-penetrating seasonal cycle at both sites which is much weaker, especially at OW, in both OSNAP and NCAR10. Nevertheless, there are differences between OSNAP and NCAR10 such as a band of northward transports between about 1700 – 470 2300 m present in OSNAP at OW but missing in NCAR10.

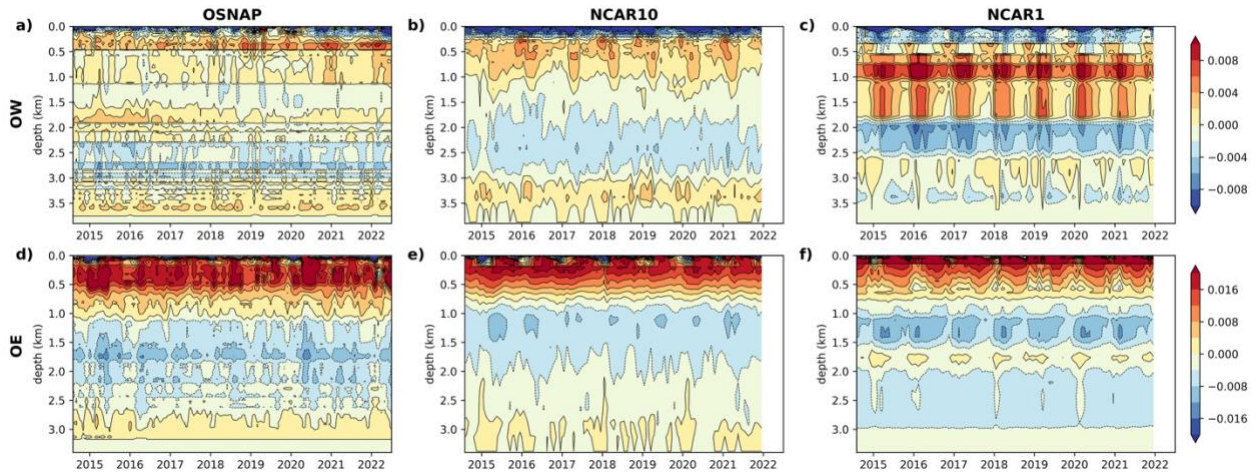
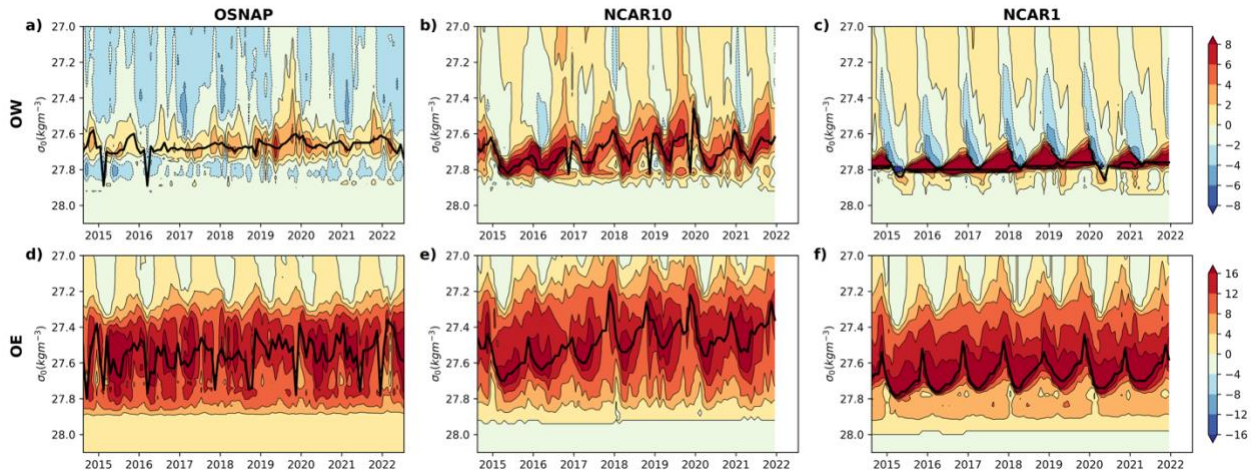


Figure 2. Transport profile timeseries in depth space from (a, d) OSNAP, (b, e) NCAR10, and (c, f) NCAR1. The top and bottom rows are for OW and OE, respectively. Positive and negative contours indicate northward and southward transports, respectively. The transports are in Sv m^{-1} . Note that different scales are used for the top and bottom panels.

The corresponding timeseries in density (σ_0) space are provided in Fig. 3. These are the integrated transports in Sv , and the streak-like features seen in depth-space OSNAP (Figs. 2a and 2d) disappear after binning. As in Fig. 2, prominent features include better agreement between OSNAP and NCAR10 than with NCAR1 and a strong seasonal cycle in NCAR1. Indeed, a seasonal cycle in OSNAP is not as pronounced as in both simulations at either site. While the magnitudes of the transports are comparable at OE among observations and model simulations, the simulated transports are larger than in OSNAP at OW, particularly so for NCAR1. The solid black lines in the panels show the density timeseries of the maximum positive transports. The details of these timeseries will be discussed below, considering all the participating simulations. Here, we note that the density at which the maximum transports occur varies considerably in time in both observations and simulations. So, even if OSNAP and simulations have similar maximum transports at a given time, the density at which this occurs can differ substantially. At OW, OSNAP has two interesting characteristics. First, the positive transport is rather weak, particularly prior to 2018, with nearly no positive transport in early 2016. Second, there are nonnegligible negative transports in density classes $< 27.6 \text{ kg m}^{-3}$ throughout the timeseries. This latter feature is somewhat present in NCAR1 but with larger magnitudes and rather strong seasonality.



495 *Figure 3.* Transport profile timeseries in density (σ_0) space from (a, d) OSNAP, (b, e) NCAR10, and (c, f) NCAR1. The top and bottom rows are for OW and OE, respectively. The solid black lines in all the panels show the density timeseries of the maximum positive transports. The transports are in Sv. Note that different scales are used for the top and bottom panels.

To provide a broader context for the observational transport estimates and their variability, annual-mean maximum transport timeseries in σ_0 space for the full forcing cycle from the
 500 simulations are presented in Fig. 4. These transports are constructed as the annual averages of the maximum monthly mean transports, where monthly mean temperature and salinity are used to compute monthly mean densities. The solid black lines represent OSNAP, while the dashed black lines indicate the respective multi-model means (MMM) for each panel. Not surprisingly, the
 505 maximum transports and their variability differ considerably among the simulations, but they show general agreement with OSNAP with their stronger transports at OE which dominate the total transports. At OW (Figs. 4a, 4d, and 4g), the simulations largely show transports of < 10 Sv. A few of the simulations, e.g., ANU1, ANU25, and FSU72, have near-zero transports during various time segments. There seems to be a slight weakening trend at OW roughly after the mid-
 510 1990s in simulated transports with the OSNAP observations coinciding with a period of low transports ($< \sim 5$ Sv) in all (but one) of the simulations. NCAR1 is a clear outlier with a mean transport of ~ 12 Sv for the 1958-2022 period with a rather large amplitude. This represents an improvement compared to a mean transport of 18.7 Sv for the 1961-2007 period reported in Li et al. (2019) for a previous version of the model that was forced with the CORE-II atmospheric

515 datasets (see Danabasoglu et al., 2014). The simulated transports at OE tend to be between 10
and 20 Sv (Figs. 4b, 4e, and 4h) with a slight weakening trend again after the mid-1990s. In
contrast with OW, OSNAP at OE is at the higher end of the simulated transport magnitudes. The
maximum total transport magnitudes (Figs. 4c, 4f, and 4i) primarily reflect those of OE, noting
that these total transports in density space do not need to reflect the sum of the OW and OE
520 transports as they are not obtained at a constant density. Among the simulations, E3SM27 shows
the lowest transport magnitudes at both OW and OE, with very little variability.

The low-frequency variations of these transports as depicted by the MMMs show roughly three
stages during the 1958-2023 period: a slight weakening until about mid-1970s; a slight
strengthening until about the mid-1990s; and a more discernable weakening until the end of the
525 simulations. While the initial weakening trend does not seem to be consistent with those of other
FOSI simulations which show rather steady AMOC transports at subpolar latitudes (Danabasoglu
et al., 2016), subsequent strengthening and weakening trends are consistent with what is seen in
other FOSI simulations and some estimates from other products (e.g., Danabasoglu et al., 2016
and Jackson et al., 2022). For example, for the 1995-2015 period, we compute weakening trends
530 of -0.21 (LR), -0.16 (MR), and -0.10 (HR) Sv yr^{-1} for the total transports – dominated by those
of OE – which are consistent with the range of -0.06 to -0.26 Sv yr^{-1} reported in Jackson et al.
(2022) for the AMOC estimates at 45°N for a similar period.

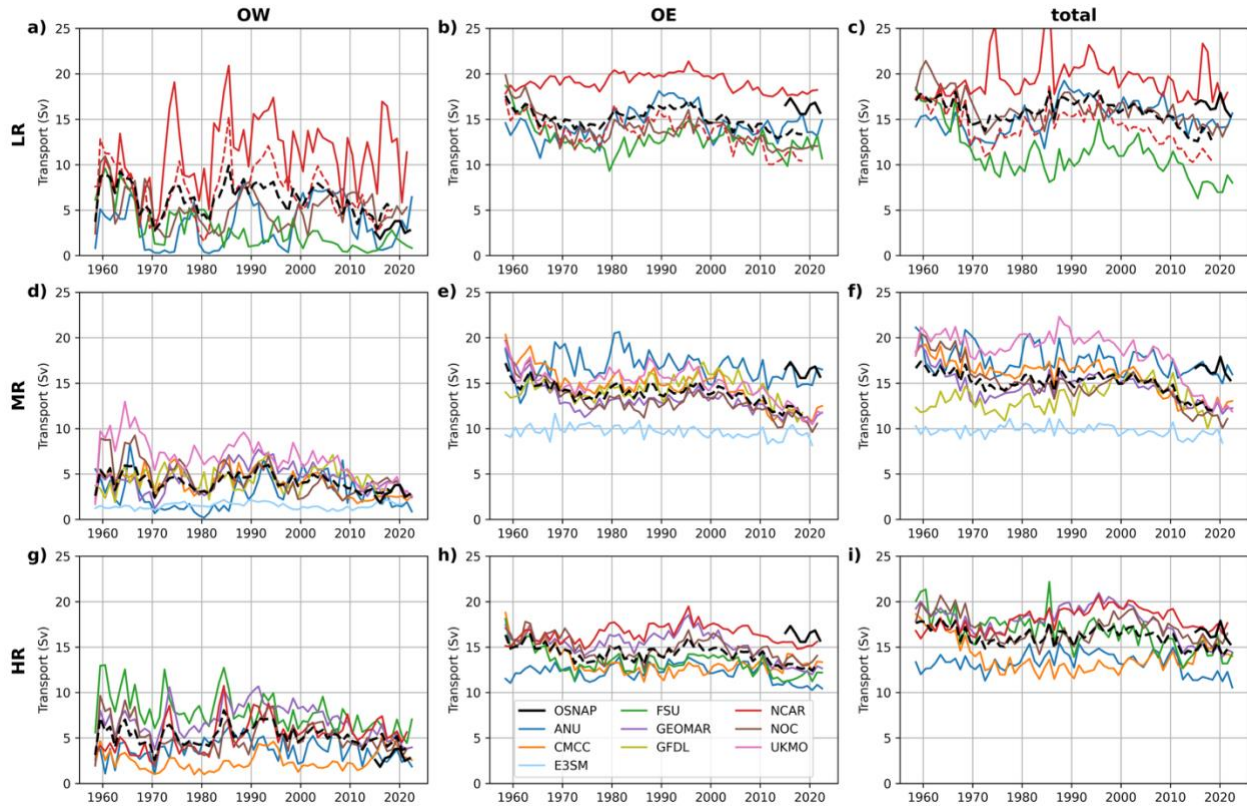


Figure 4. Annual-mean maximum transport timeseries in σ_0 space for (a, d, g) OW, (b, e, h) OE, and (c, f, i) total. The top, middle, and bottom panels are from LR, MR, and HR, respectively.

535 The solid black lines show the OSNAP transports. The dashed black lines represent the respective multi-model means. The dashed red lines are for NCAR67.

The mean seasonal cycles of maximum transports in σ_0 space from each simulation are presented in Fig. 5. The solid black lines represent OSNAP with the gray shading showing ± 1 monthly standard deviation (SD). The respective MMMs for each panel are also provided by the dashed black lines. At OW (Figs. 5a, 5d, and 5g), the seasonal cycle is relatively weak, with OSNAP showing generally larger transports in spring and smaller transports in winter, but with a minimum in September. Most of the simulations do not capture this observed phasing, also displaying differing maximum and minimum transport months among each other. Except for NCAR1, LR and MR simulations largely cluster around the OSNAP spread. NCAR1 is a clear outlier with the largest transport and seasonal cycle amplitude. In contrast, ANU25, E3SM27, and FSU72 have the lowest transports, near the lower bound of the OSNAP spread. HR simulations tend to be outside the OSNAP spread with higher magnitudes. Here, ANU10 and

540

545

CMCC06 are the closest to the OSNAP spread. At OE (Figs. 5b, 5e, and 5h), OSNAP has a better-defined seasonal cycle – compared to that at OW – with maximum transports in spring and minimum transports in winter. Arguably, the simulations capture the observed seasonal cycle phasing relatively well as reflected in the MMM. An exception is the last few months, particularly evident in HR simulations, where all HR models show an increasing transport after September in contrast with a decreasing trend in OSNAP. Most simulations have transports that are below or near the lower bound of the OSNAP spread, again as also depicted in the MMM.

Among all the simulations, only ANU25 remains within the OSNAP spread throughout the seasonal cycle, but has a somewhat different phasing than in OSNAP with a peak in July. NCAR1 has again the highest transports among all the simulations. E3SM27 among MR and ANU10 and FSU08 among HR show the lowest transports with the largest departures from OSNAP. The total transports remain below or near the lower bound of the OSNAP spread in LR and MR, reflecting those of OE (Figs. 5c and 5f). In contrast, HR transports are within the OSNAP spread except for ANU10 (Figs. 5i). We note that the large-amplitude seasonal cycles at OW and OE in NCAR1 mostly cancel each other, resulting in a much smaller amplitude for the total transport. Finally, to provide a quantitative comparison of the simulated seasonal cycles and those of OSNAP, we calculate the root-mean-square differences between MMM and OSNAP as 2.7 Sv (LR), 0.8 Sv (MR), and 2.9 Sv (HR) for OW; 2.2 Sv (LR), 3.9 Sv (MR), and 2.6 Sv (HR) for OE; and 2.4 Sv (LR), 3.6 Sv (MR), and 1.5 Sv (HR) for the total transports.

NCAR1 is a clear outlier with the largest transport and seasonal cycle amplitude at OW among the simulations. The phasing of its seasonal cycle – which is out-of-phase with OSNAP – reflects that of Fig. 3c with a minimum transport in April. This results from incursions of the negative transport cells into higher density classes. Such negative transport cell incursions are also present in both OSNAP and NCAR10, but they are less well organized, and their densities and transports remain much smaller than in NCAR1. It is also interesting to note that maximum mixed or boundary layer depths in the LS region occur in March (not shown), but the OSNAP section is not co-located with these regions of maximum mixed layer depths. Instead, the OSNAP section was purposely located near the exit of the LS to capture the bulk of the waters exported from the basin. These aspects, including such seasonal cycle features, will be investigated in detail in a follow up study, considering water mass formation and transformation analysis.

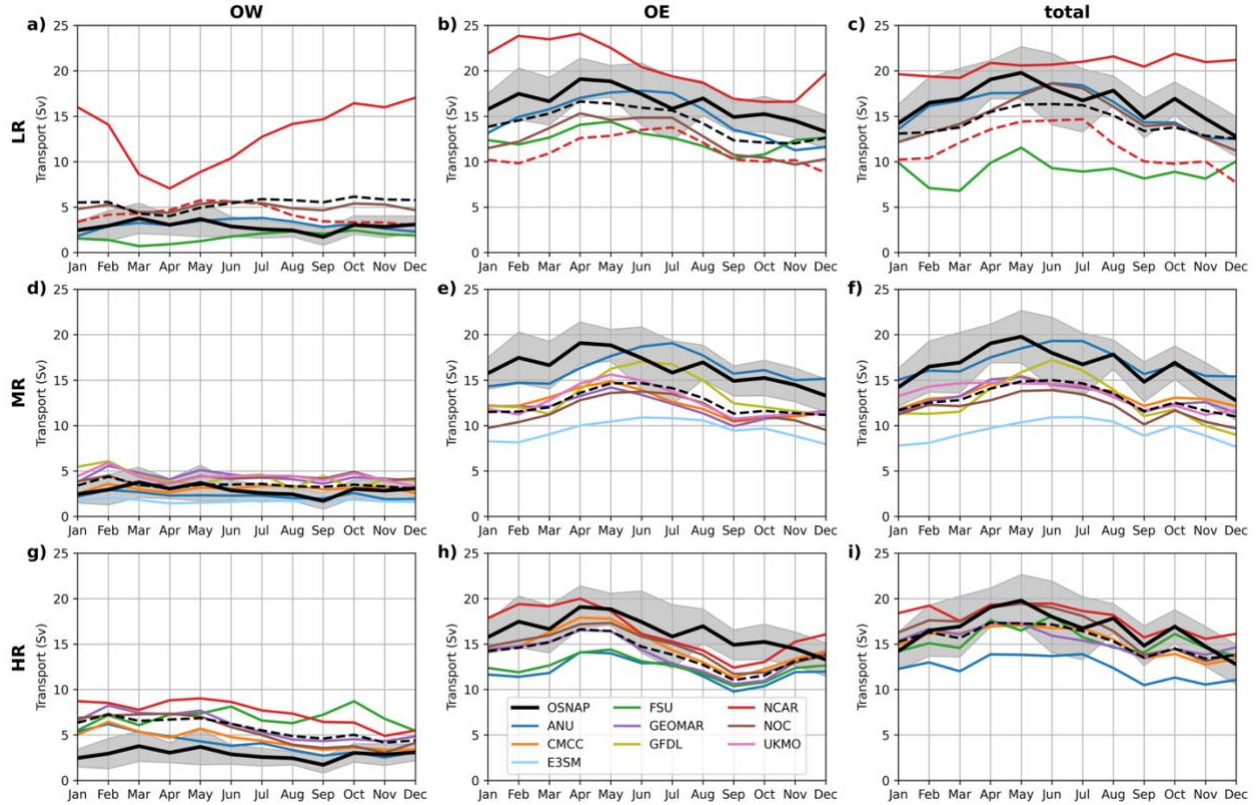
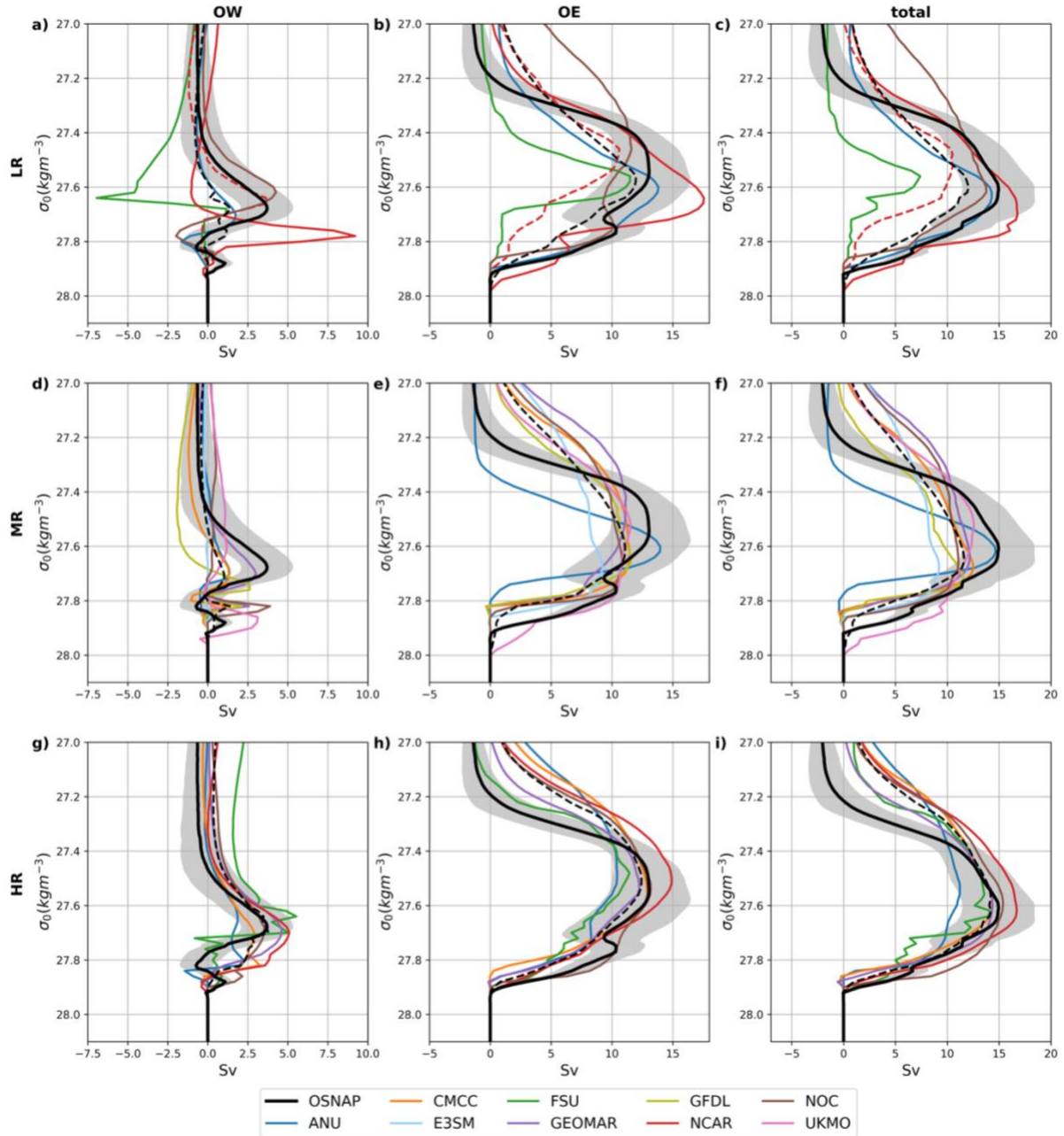


Figure 5. Time-mean maximum transport seasonal cycles in σ_0 space for (a, d, g) OW, (b, e, h) OE, and (c, f, i) total. The top, middle, and bottom panels are from LR, MR, and HR, respectively. The solid black lines show the time-mean OSNAP maximum transport timeseries with gray shading indicating ± 1 monthly standard deviation. The dashed black lines represent the respective multi-model means. The dashed red lines are for NCAR67.

4 Time-Mean Transports in σ_0 Space

Figure 6 shows the time-mean transport profiles in σ_0 density space. As in the previous figures, the solid black lines represent OSNAP with the gray shading showing ± 1 monthly SDs, and the respective MMMs for each panel are also provided by the dashed black lines. The figure clearly demonstrates that the simulated transports are much larger at OE than at OW with the total transports dominated by those of OE, all in agreement with OSNAP. At OW (Figs. 6a, 6d and 6g), the simulations largely follow the OSNAP profile. However, at high density classes ($\sigma_0 > \sim 27.7 \text{ kg m}^{-3}$), there are differences from observations as well as among the simulations. While these high-density transports are relatively small, they can play an outsized role in downstream AMOC variability on decadal timescales (Yeager et al., 2021). NCAR1 has the largest maximum

transport with about 9 Sv. While FSU72 shows the highest negative transport magnitude with a distinct peak around 27.65 kg m^{-3} , a feature not present either in OSNAP or other simulations, 595 FSU08 deviates the most from observations and the other simulations at density classes $< 27.5 \text{ kg m}^{-3}$. At OE (Figs. 6b, 6e, and 6h), a large majority of the simulations have positive transports with negative slopes for densities $< \sim 27.3 \text{ kg m}^{-3}$. This contrasts with OSNAP that shows a much steeper negative density slope for $\sim 27.2 < \sigma_0 < \sim 27.4 \text{ kg m}^{-3}$ and nearly no net flow for densities $< 27.2 \text{ kg m}^{-3}$ (see also Fig. 3d). Several factors may contribute to this discrepancy between the 600 simulations and OSNAP, including differences in current pathways and their temperature and salinity properties, and possible under-sampling of Greenland shelf waters in OSNAP. For $\sim 27.3 < \sigma_0 < \sim 27.8 \text{ kg m}^{-3}$, the simulations tend to agree better with OSNAP with most within the observed range, particularly for HR. Here, ANU25, FSU72, and NCAR67 show lower transport magnitudes, and NCAR1 has the largest magnitude with a transport of $\sim 18 \text{ Sv}$. Observed 605 transports at high density classes ($> 27.8 \text{ kg m}^{-3}$) appear to be shifted to somewhat lower densities in the simulations. The total transport features are mostly similar to those at OE (Figs. 6c, 6f, and 6i). FSU72 has the smallest maximum transport with $\sim 7 \text{ Sv}$ due to its large negative transport at OW. The maximum transport is $< 10 \text{ Sv}$ for E3SM27 as well. HR profiles, in general, show better agreement with OSNAP than those of LR and MR for $\sigma_0 > \sim 27.4 \text{ kg m}^{-3}$. Finally, we 610 note that all FSU08 profiles are noisy, particularly at high densities, which may be due to a mismatch between σ_0 increments used in the analysis and the resolution of the model σ_2 coordinates. Specifically, with relatively small σ_0 increments at high density classes, transports within a σ_2 model layer can be binned into different σ_0 layers, thus leading to some noise.



615 *Figure 6.* Time-mean transport profiles in σ_0 space for (a, d, g) OW, (b, e, h) OE, and (c, f, i) total. The top, middle, and bottom panels are from LR, MR, and HR, respectively. The solid black lines show the OSNAP transports with gray shading indicating ± 1 monthly standard deviation. The dashed black lines represent the respective multi-model means. The dashed red lines are for NCAR67.

620 The details of the time-mean, west-to-east cumulative volume transports for the upper and lower limbs and their total across the OSNAP sections are presented in Fig. 7. Here, the upper (lower) limb is defined as the transport between the ocean surface (bottom) and the density surface of the maximum transports. Again, the solid black lines represent OSNAP with the gray shading showing ± 1 monthly SDs. In the plots, the negative and positive slopes indicate southward and northward transports, respectively.

625 The observations show strong boundary transports in the LS with southward and northward transports narrowly confined to the western and eastern boundaries of the basin, respectively. There are no appreciable transports within the interior of the basin, indicating little, if any, density transformation or overturning there. The upper- and lower-limb boundary current transports are about 7 and 30 Sv, respectively. Across OSNAP East, there are again strong
630 boundary currents. The lower-limb transports clearly show the southward flowing Denmark Strait overflow waters to the east of Greenland and the Faroe Bank Channel overflow waters along the eastern flank of the Reykjanes Ridge. The total southward transports reach ~ 30 and ~ 15 Sv, respectively, in these regions (e.g., Fig. 7g). In contrast to the Labrador Basin, there are compensating, i.e., northward, transports in the interiors of the Irminger and Iceland Basins.

635 Arguably, many of these observed transport features are much better reproduced in the HR simulations (Figs. 7g-i) than in LR (Figs. 7a-c) and MR (Figs. 7d-f), likely due to better representation of boundary currents in HR with its higher resolution. Nevertheless, there are a few notable differences between HR and OSNAP, including more spatial variability in the LS in the simulations in the lower limb with CMCC06 and GEOMAR05 showing somewhat smaller
640 transports. The simulated Faroe Bank Channel overflow transports are also smaller than OSNAP. In the upper limb, CMCC06 has a slightly larger transport magnitude compared to OSNAP and the other simulations. We note that HR shows a bump around 2500 km to the east of the Iceland Basin – a feature also present in MR, indicating a strong northward transport followed by a modest southward transport. Such a feature is absent in OSNAP.

645 Both MR and LR show large discrepancies with OSNAP in both lower- and upper-limb transports with no apparent advantage for MR. These differences are particularly obvious in the LS with simulated boundary current transports ranging between about -5 to about -40 Sv in the lower limb. Here, NCAR1 and NOC25 show transports comparable to those of OSNAP, with

NCAR1 tending to be larger than in OSNAP. The simulation spreads are also large in the
 650 Irminger and Iceland Basins. We note that FSU72 and UKMO25 have mostly weaker and
 stronger lower-limb transports, respectively, across the sections compared to OSNAP and the
 other models.

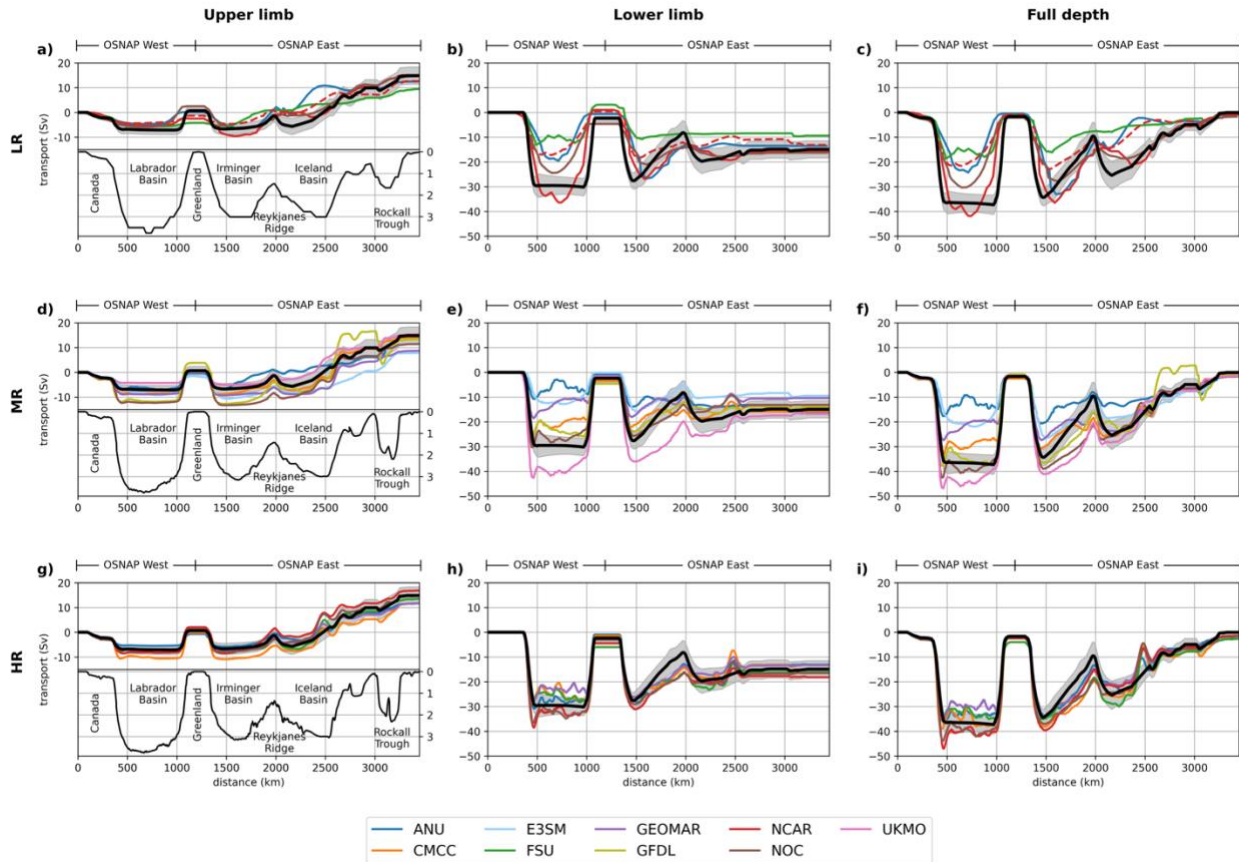


Figure 7. Time-mean west-to-east cumulative transports across the OSNAP sections for the (a, d,
 g) upper limb, (b, e, h) lower limb, and (c, f, i) full depth. The upper, middle, and bottom rows
 655 are for LR, MR, and HR, respectively. The solid black lines show the OSNAP transports with
 gray shading indicating ± 1 monthly standard deviation. The positive and negative slopes
 indicate northward and southward transports, respectively. Typical representations of the
 topographic features for each grid resolution from one of the respective models are also provided
 in the left panels with depth given on the right y-axis in km.

660

5 Time-Mean Transports in Depth and σ_2 Space

The time-mean overturning transports in both depth and σ_2 density space from OSNAP and all the simulations at OW and OE are provided in Figs. 8-9 and Figs. 10-11, respectively. In these
665 figures (as well as in those in Sect. 7), an alphabetical ordering of simulations is adopted to expedite comparisons within a set of simulations from the same group, except for swapping GFDL and GEOMAR simulations to keep the GEOMAR pair on the same figures. In each set of plots, the main panels (color shading) show southward (blue) and northward (red) transports as a function of density and depth. These are transports in Sv, calculated using the common σ_2 bins,
670 listed in section 2.5, and each model's vertical grid. We prefer to use Sv for this purpose, rather than transport per unit depth, i.e., Sv m^{-1} , because this way the transports can be summed easily in either depth or density space. As such, the profile panels on the right then show the summed transports in depth space. Specifically, the thin blue, red, and black lines display the summed transports in depth space for the southward, northward, and total, i.e., the sum of the southward
675 and northward, transports, respectively. When the total transports are aggregated (or integrated) in the vertical, starting from the bottom, the familiar overturning transport profiles in depth space are obtained (thick black lines). Similarly, when the transports of the main panels are summed across constant density bins, the top plots are obtained, showing the transport profiles in density space. The thick black lines show the overturning transports in density space, aggregated starting
680 from the densest bin class. These are essentially the same profiles shown in Fig. 6, but they are now calculated in σ_2 space instead of σ_0 . Therefore, calculated maximum transports differ as noted below. We note that this analysis can be easily extended to depth – temperature or depth – salinity space to obtain respective transports (not shown). As Figs. 8-11 contain a lot of information, we only discuss a few notable features for brevity.

685 In OSNAP, the OE transports are more distinctly organized in comparison to those of OW, with continuous southward and northward transport bands occurring at higher and lower density classes, respectively, throughout all depths. At OW, the structure is a bit more complex. A continuous southward transport band between about 1000 – 3500-m depth splits two northward bands occurring at mid-depth and abyssal ocean. With rather similar high-density waters, OE
690 exhibits broader density ranges at all depths due to the presence of lighter density waters compared to OW. At both sections, the transports can exceed 0.5 Sv in both directions. The

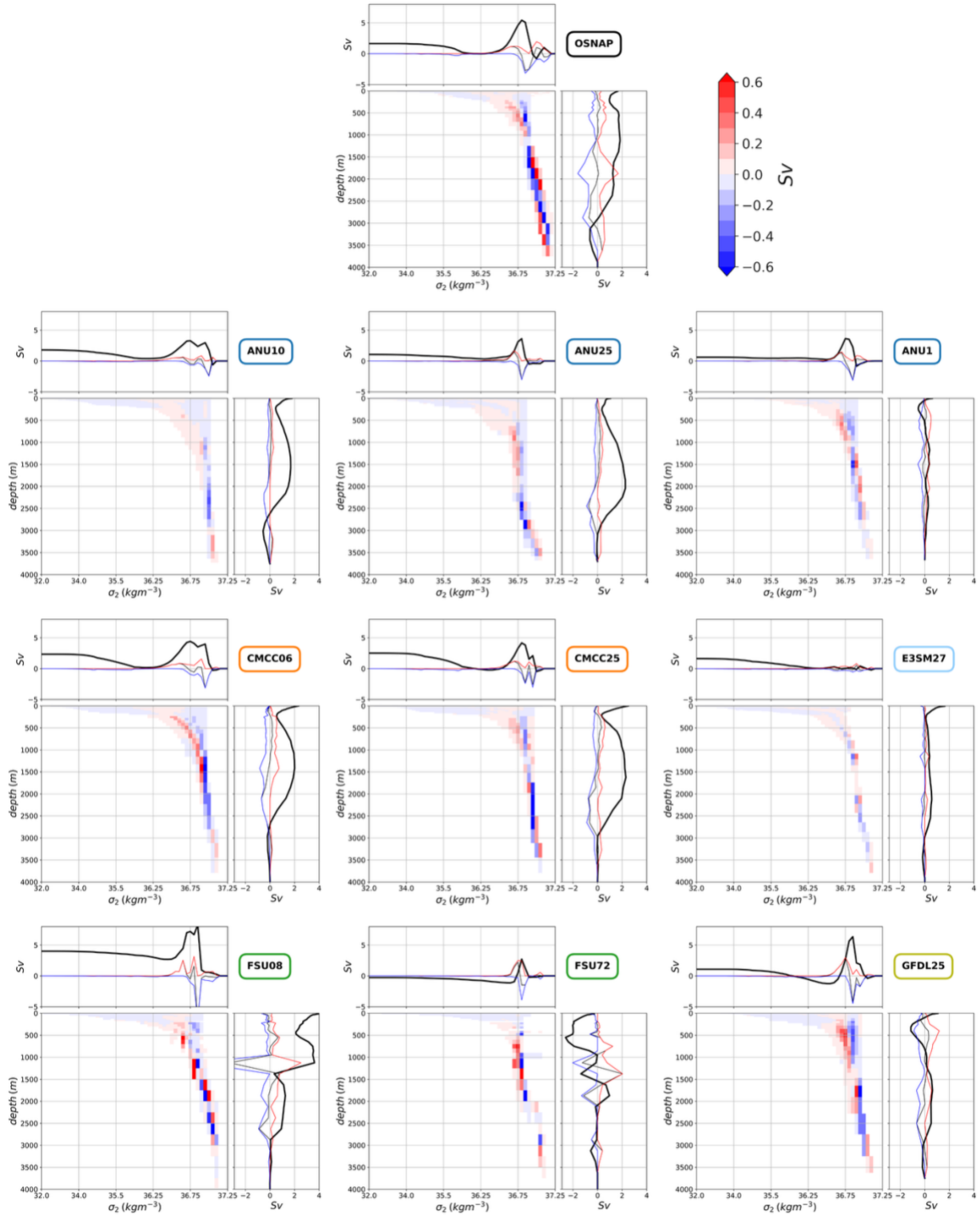
summed transports (right panels) reveal substantial cancellations of southward and northward flows in depth space, producing relatively small total transports, at both sections. These profiles have some noise in the upper 500 m. The integrated overturning profile in depth space has a rather odd shape at OW without a well-defined maximum or flow structure, essentially reflecting the noisy velocity bands of Fig. 2a. Nevertheless, its maximum transport is slightly less than 2 Sv. In contrast, the depth-space overturning profile at OE is well-defined, with a maximum transport of about 8.2 Sv. There are cancellations of southward and northward transports in density space as well (top panels). The maximum transports are 5.3 and 14.0 Sv for OW and OE, respectively. We note that these transports in σ_2 space are larger than the corresponding transports of 3.8 and 12.9 Sv in σ_0 space presented in Fig. 6. These indicate that while the ratio of the transports at OE and OW is 3.4 in σ_0 , it drops to 2.6 in σ_2 space, representing a 25% reduction. We will come back to this point later in the manuscript.

It is interesting to note that some degree of cancellation of northward and southward flows in OSNAP occurs at all depths. In density space, these cancellations are less uniform, especially at OW where they are pronounced for $\sigma_2 > 36.9 \text{ kg m}^{-3}$. At OE, any cancellation is confined to intermediate density classes with not much cancellation of northward flow of $\sigma_2 < 36.4 \text{ kg m}^{-3}$ in the upper 1000 m and the southward flow of $\sigma_2 > 37.1 \text{ kg m}^{-3}$ below $\sim 2000 \text{ m}$.

Arguably, the simulations capture observed transport features better at OE (Figs. 10 and 11) than at OW (Figs. 8 and 9). In all simulations, a well-defined southward transport band at high density classes that extends through almost the entire depth and an upper-ocean northward transport region extending from the surface to about 1500-m depth and diagonally in density from roughly 35.5 to 36.75 kg m^{-3} are captured at OE. However, the northward transport band at deeper levels and at higher densities seen in OSNAP is largely missing in all simulations except for FSU08 and UKMO25. Consequently, summed northward transports do not cancel much of southward transports below about 1500-m depth and in high density classes. In depth space, the maximum aggregated transports at OE are between 4.5 Sv (GFDL25) and 8.9 Sv (ANU25 and ANU1) occurring between 750 – 1250 m, but mostly around 1000-m depth, noting that the OSNAP estimate is $\sim 8.2 \text{ Sv}$. In σ_2 space, the maximum aggregated transports range from about 10 Sv in E3SM27 to about 15 Sv in ANU1, ANU25, CMCC06, NCAR10, and NCAR1, bracketing the OSNAP transport of 14 Sv. While most simulations show a density range of 35.75 to 37.25 kg m^{-3}

³ for the positive transport segment in σ_2 profiles in agreement with OSNAP, this range is much narrower in ANU25 and FSU72, remaining between about 36.25 and 36.75 kg m⁻³ (top panels for all simulation sets). The secondary peak near 36.9 kg m⁻³ seen in OSNAP is present in FSU08, 725 NCAR1, and NOC1, likely due to larger northward flows near this density in these simulations compared to the other simulations. Among the simulations, FSU08 and FSU72 exhibit somewhat noisier transports in depth – density binned transports, likely due to the choice of their hybrid vertical levels.

At OW, the simulations appear to struggle to capture observed binned transport features in depth 730 – σ_2 panels with notable differences among the simulations as well. Although these binned transports show similar transport magnitudes to those at OE, their summed and aggregated transport magnitudes are smaller than at OE, consistent with observations. There are cancelling southward and northward transports in both depth and σ_2 space and most simulations reproduce the observed structure of the aggregated transports reasonably well. In depth space, the 735 maximum aggregated transports are mostly around 2 Sv within 1000-2000-m depth range, with a few exceptions. Specifically, ANU1, E3SM27, and GFDL25 have rather weak transports of about < 0.5 Sv. In E3SM27, there is essentially no significant transport at OW. In ANU1 and GFDL25, there are significant cancellations between southward and northward transports. While 740 some simulations exhibit noise in their summed southward and northward transport profiles which are cancelled in the aggregated transports, such noise is particularly large and remains in aggregated transport profiles in FSU08 and FSU72. In density space, E3SM27 does not show any notable transports for $\sigma_2 > \sim 36$ kg m⁻³. At the opposite end, NCAR1 has the highest transport with 13.1 Sv (off scale in Fig. 9).



745 *Figure 8.* Time-mean transports at OW in depth and density (σ_2) space from OSNAP and from ANU10, ANU25, ANU1, CMCC06, CMCC25, E3SM27, FSU08, FSU72, and GFDL25. In each set, the bottom left panels show southward (blue) and northward (red) transports in Sv. The

bottom right panels are the summed transports in depth space with the thin blue, red, and black lines displaying the southward, northward, and total, i.e., the sum of the southward and northward, transports, respectively. Similarly, the top panels show the summed transports in density space. In the right and top panels, the thick black lines are the respective overturning transports with aggregation (integration) starting from the bottom and the densest bin for depth and density space, respectively.

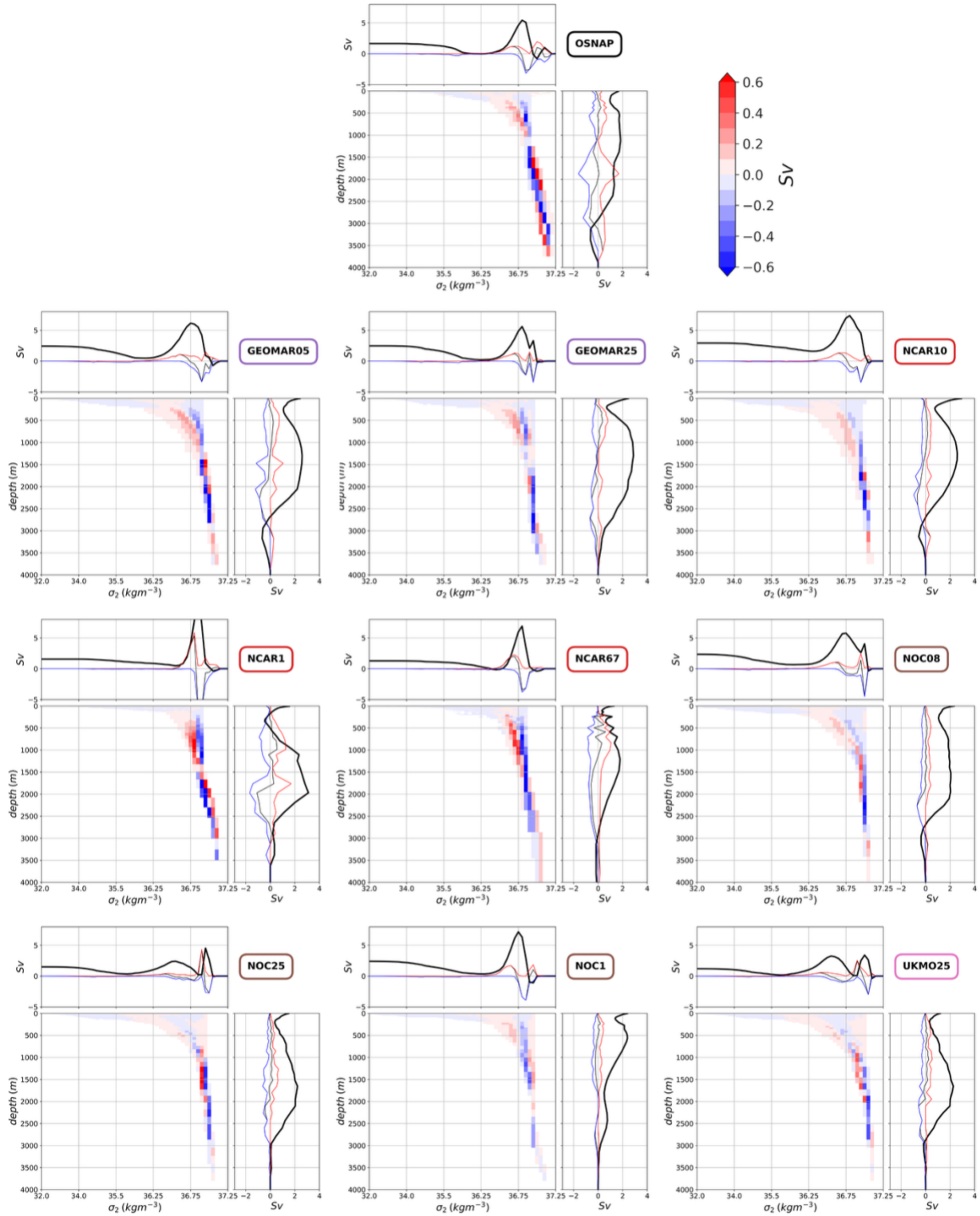


Figure 9. Same as in Fig. 8, but for GEOMAR05, GEOMAR25, NCAR10, NCAR1, NCAR67, NOC08, NOC25, NOC1, and UKMO25. The density-space aggregated maximum transport in

755 NCAR1 is 13.1 Sv.

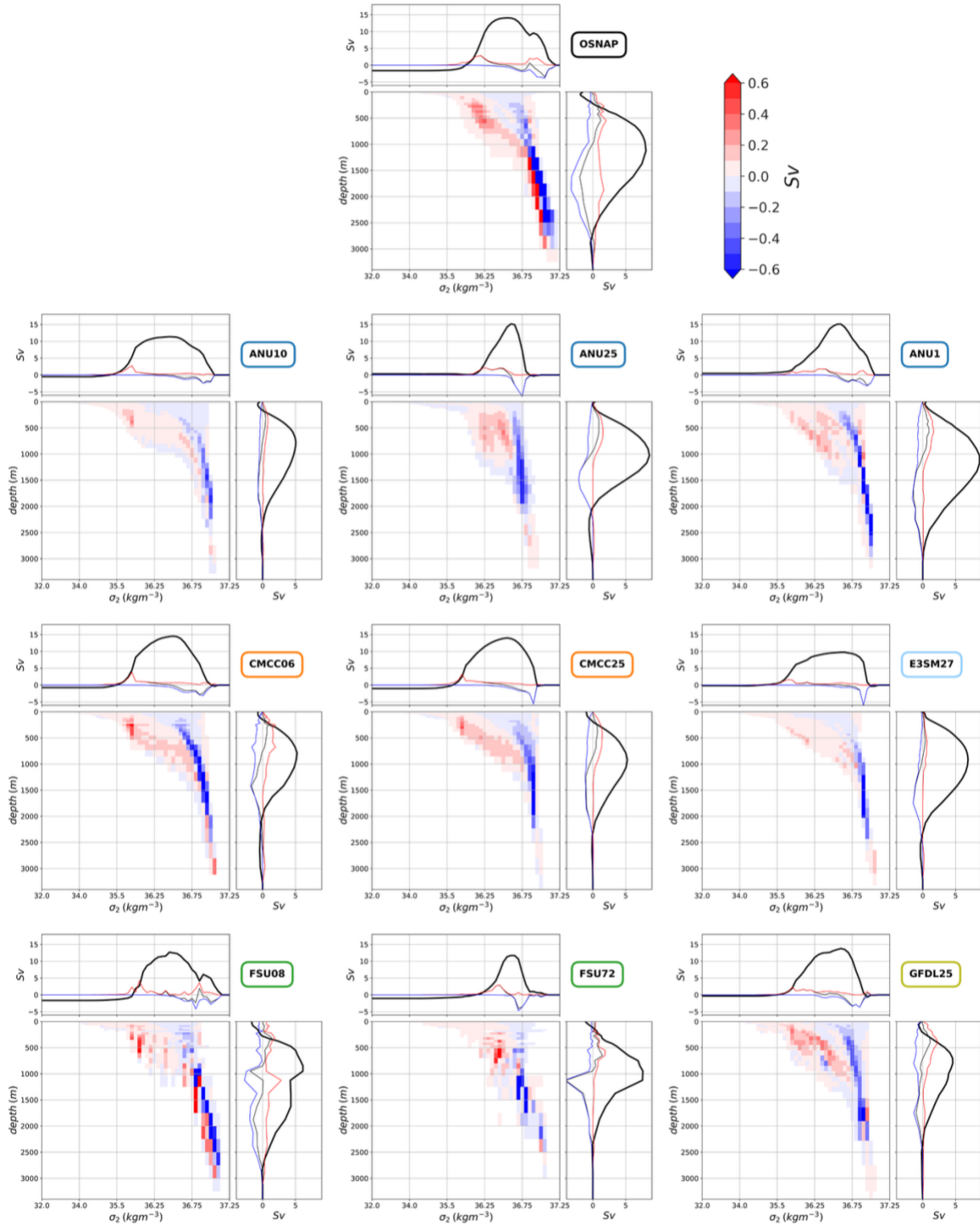


Figure 10. Same as in Fig. 8, but for transports at OE.

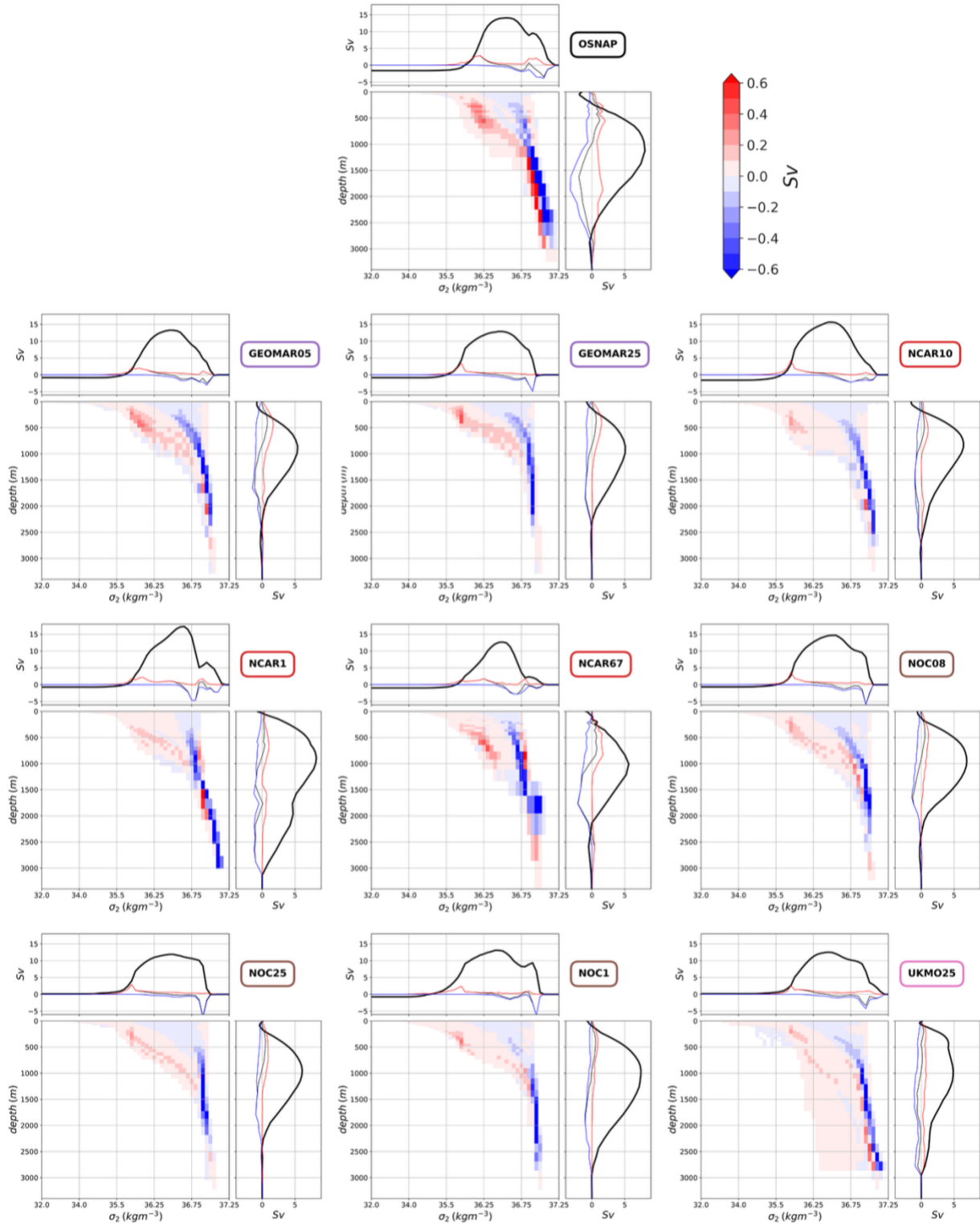


Figure 11. Same as in Fig. 9, but for transports at OE.

To expand upon our earlier discussion, we assess the impacts of using different potential
760 densities on overturning transports considering the scatter plots presented in Fig. 12. Panels a-c
show the time-mean maximum transport magnitudes as a function of σ_0 and σ_2 densities for the
OW, OE, and total transports, respectively. For OW and the total, the σ_2 transports are
consistently higher than those in σ_0 in all simulations, on average, by 2.52 Sv and 1.73 Sv,
respectively. At OE, all but one simulations are larger in σ_2 than in σ_0 with an average increase
765 of 1.18 Sv which is smaller than those for OW and the total. To quantify these transport changes,
we first compute the ratios of OW and OE transports for σ_0 and σ_2 separately which can be
denoted as R_{σ_0} and R_{σ_2} , respectively. We then produce a scatter plot of $R_{\sigma_2}/R_{\sigma_0}$ presented in
Fig. 12d. This measure considers the relative changes in the maximum transports with density at
both OW and OE. The figure shows that this ratio exceeds unity for all simulations, with most of
770 them clustering roughly between 1.2 – 1.5, indicating larger OW contributions in σ_2 space
compared to those of σ_0 . ANU25 and FSU72 have the largest ratios with ~ 1.9 and 2,
respectively. We note that the spread of the LR and MR simulations is much larger than that of
the HR simulations, which cluster around a ratio of 1.3. These model-based findings are
consistent with the OSNAP observations which are included as black dots in all the panels,
775 showing roughly a middle-of-the-pack value of ~ 1.4 in Fig. 12d.

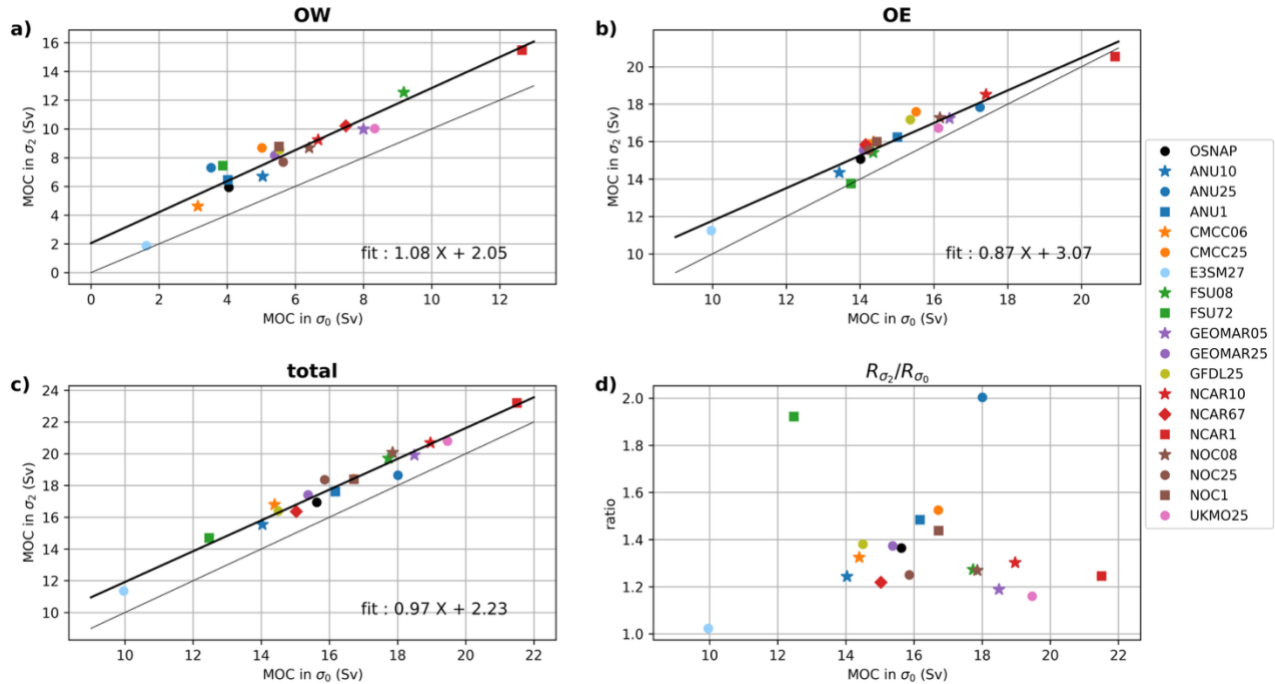


Figure 12. Scatter plots of time-mean maximum transports in σ_0 vs. σ_2 space for (a) OW, (b) OE, and (c) total. (d) Scatter plot of $R_{\sigma_2}/R_{\sigma_0}$ (see text) as a function of the total transport in σ_0 space. The LR, MR, and HR simulations are indicated by squares, circles, and stars, respectively. NCAR67 is shown as a diamond. The black regression lines (excluding OSNAP) along with their coefficients are included in each panel. The gray one-to-one lines are also shown for reference in (a-c).

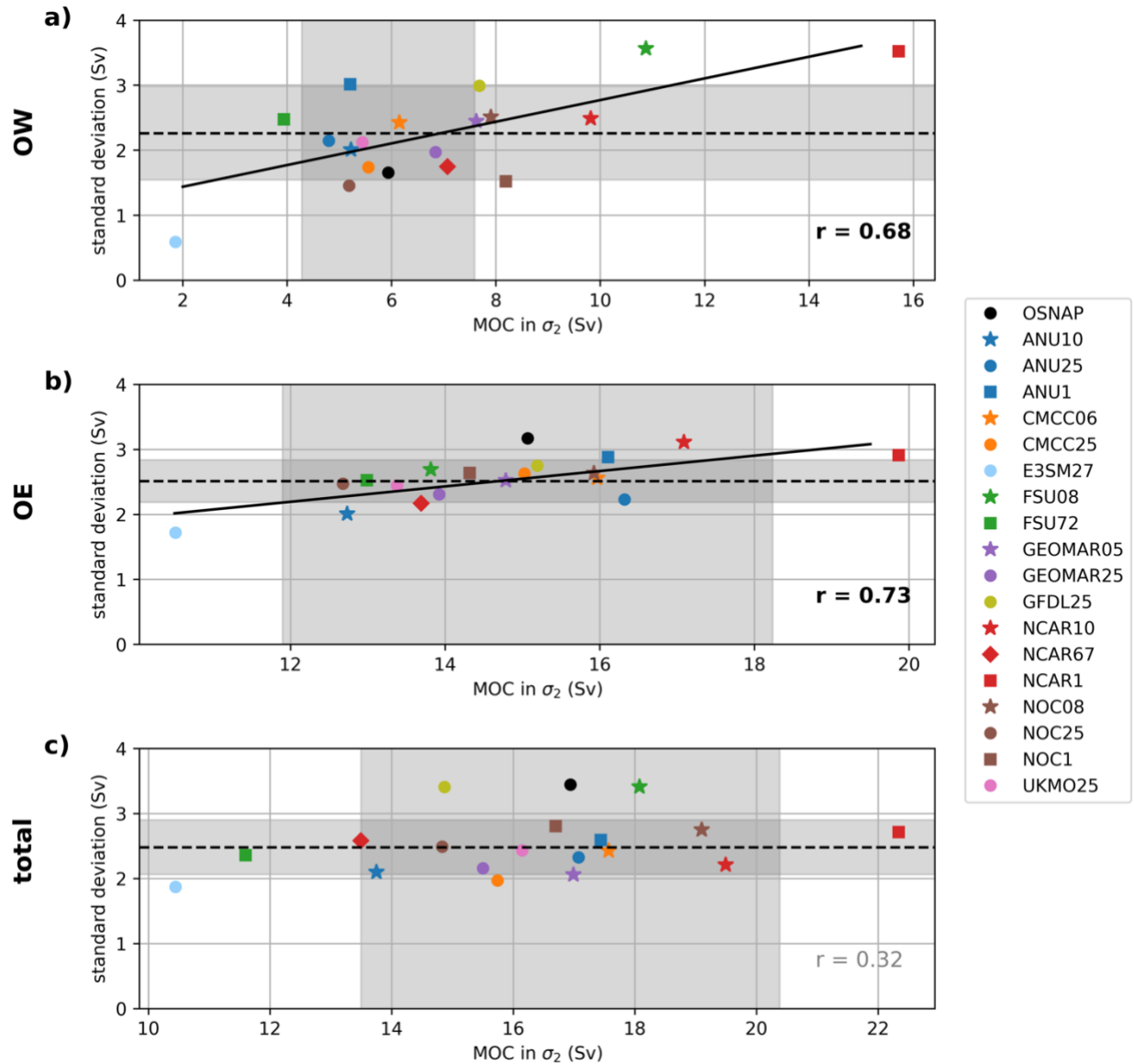
6 Transport Standard Deviations in σ_2 Space

We examine the variability of maximum transports, considering the scatter plots of time-mean maximum transports and their monthly SDs given in Fig. 13 for OW, OE, and their total.

785 Obtained in σ_2 space, these plots show statistically significant correlations between the strength of the maximum transports and the amplitudes of variability at both OW and OE, with larger transports associated with larger variability. While all the simulations are subject to the same external variability, their SDs differ considerably due to differing internal variabilities, primarily in response to buoyancy forcings: especially at high latitudes, convective / deep-water formation

790 events can differ across simulations. The simulated ensemble mean SDs are slightly higher at OE than at OW, but the spread of the simulated SDs is larger at OW than at OE. While OSNAP SD (= 1.64 Sv) at OW is lower than those of most simulations, OSNAP SD (= 3.18 Sv) at OE is

larger than in all simulations. Relatedly, there are 9 and 16 simulations within 1 SD of the observational maximum transports at OW and OE, respectively. At OW, CMCC25, NCAR67, NOC1, and NOC25 are the closest to OSNAP SD. Here, FSU08 and NCAR1 have the largest SDs (> 3.5 Sv), and E3SM27 shows the smallest SD with ~ 0.5 Sv. At OE, SDs of ANU1, NCAR10, and NCAR1 are in better agreement with that of OSNAP, and E3SM27 SD of < 2 Sv is the lowest among the simulations. For the total transports, OSNAP SD is again larger than those of nearly all simulations, with FSU08 and GFDL25 closest to it. E3SM27 and CMCC25 have the lowest SDs with slightly lower than 2.0 Sv.



805 *Figure 13.* Scatter plots of time-mean maximum transports vs. their monthly standard deviations (SDs) in σ_2 space for (a) OW, (b) OE, and (c) total. The horizontal dashed lines show the respective ensemble mean SDs with shading indicating their ± 1 SDs. The vertical shaded areas indicate ± 1 SD ranges for OSNAP maximum transports. The LR, MR, and HR simulations are indicated by squares, circles, and stars, respectively. NCAR67 is shown as a diamond. The correlation coefficients (excluding OSNAP) are included in each panel with the bold font indicating statistical significance at the 95% confidence level, calculated using a 2-sided Student's t-test. The regression lines are also shown for (a, b) with statistically significant correlations.

810 7 Temperature – Salinity Diagrams

We next consider (potential) temperature – salinity (T-S) diagrams for depths > 500 m as depicted in Figs. 14-17. These are based on monthly mean data and densities are in σ_2 space. We note that some of the differences in the spread of T and S values among the panels, especially at mid-depths, are due to the use of each model’s native vertical grid. We further note that because
815 we are primarily interested in deep and abyssal ocean properties, we choose to use a 500-m cutoff depth here to exclude even larger spreads in the upper ocean which result from the models’ fine vertical resolutions near the surface.

For OW (Figs. 14 and 15), T-S diagrams span 1 – 7 °C in temperature and 34.5 – 35.2 psu in salinity to cover the spread of the simulations. As with the previous figures, we only highlight
820 several key features for brevity. In OSNAP, S is rather uniform around 34.9 psu for depths > ~1500 m. As such, waters with $\sigma_2 > 37.0 \text{ kg m}^{-3}$ show densification with depth associated with cooling from roughly 3 °C to about 1.5 °C. We note that these T-S diagrams do not necessarily identify mechanisms driving these T and S properties which can result from various processes both locally and remotely, including mixing and advection. All the simulations also show dense
825 waters with $\sigma_2 > 37 \text{ kg m}^{-3}$ at depth, consistent with OSNAP, but there are differences in their T and S properties. Except for FSU08 and UKMO25, the simulations have a rather thin, line-like, diagonal structure at high density classes. Most simulations show densification through high-to-low T and S. However, in ANU25, CMCC25, FSU08, GEOMAR25, NOC25, and UKMO25 densification occurs primarily through cooling at relatively constant S. In contrast with all the
830 other simulations, and indeed OSNAP, NCAR67 has densification due to both lower T and higher S values. The discontinuous nature of T and S properties in FSU08 and FSU72 reflect the HYCOM’s discrete isopycnic coordinates. We also note that FSU27 does not appear to show much density distribution at depth. Among the simulations, UKMO25 attains densities greater than 37.0 kg m^{-3} with the highest S and warmest T values likely due to too high S associated with
835 the overflow waters (see below).

At OE (Figs. 16 and 17), we employ wider ranges than at OW for both T and S, i.e., 1 – 12 °C and 34.5 – 36.0 psu, respectively. The observations show a diagonal band extending from high T (~10 °C) and S (~35.4 psu) to lower T (~1.2 °C) and S (~34.9 psu) values with a maximum density of ~37.2 kg m^{-3} around 3000-m depth. Like OW, the deep ocean has a rather uniform S,

840 and densification is due to colder T. This diagonal structure is reproduced by all the simulations. However, all but three have maximum densities of about 37.0 kg m^{-3} . In FSU08, NCAR1, and UKMO25, the maximum densities are closer to the observed values, but with slightly saltier and warmer waters. FSU08, FSU72, and NCAR67 show a discontinuous (banded) T and S structure, reflecting their density layers. Again, FSU72 does not seem to capture high-density classes.

845 High density classes at OE are thought to be associated with the properties of the Denmark Strait (DS) and Faroe Bank Channel (FBC) overflows. Observational estimates of the product water T and S are $2.1 \text{ }^\circ\text{C}$ and 34.84 psu for DS (Legg et al., 2009; Girton & Sanford, 2003) and $3.3 \text{ }^\circ\text{C}$ and 35.1 psu for FBC (Legg et al., 2009; Mauritzen et al., 2005). OSNAP shows much colder water masses than the above estimates for DS and FBC overflows. This discrepancy may be due

850 to different observational periods that these estimates are based on. As stated above, among all the simulations, only FSU08, NCAR1, and UKMO25 reach maximum densities closest to the observed values at OE. Among these, NCAR1 uses an overflow parameterization to represent the DS and FBC overflows. In NCAR1, the parameterization (Danabasoglu et al., 2010) appears to maintain distinct properties of the two overflow waters. In UKMO25, the overflow waters are

855 warmer and saltier than observed. This is probably due to a synergy between their hybrid vertical coordinate system and the large-scale T and S biases affecting their North Atlantic subtropical and subpolar gyres. While their hybrid vertical grid is able to significantly reduce numerical diapycnal mixing when simulating the Nordic overflows, this inevitably results in transporting the density-compensated T and S biases of the upper water column down to greater depths (see

860 Bruciaferri et al. (2024) for the details). FSU08 is the only simulation that has minimum temperatures colder than $2 \text{ }^\circ\text{C}$, closer to those observed at OE.

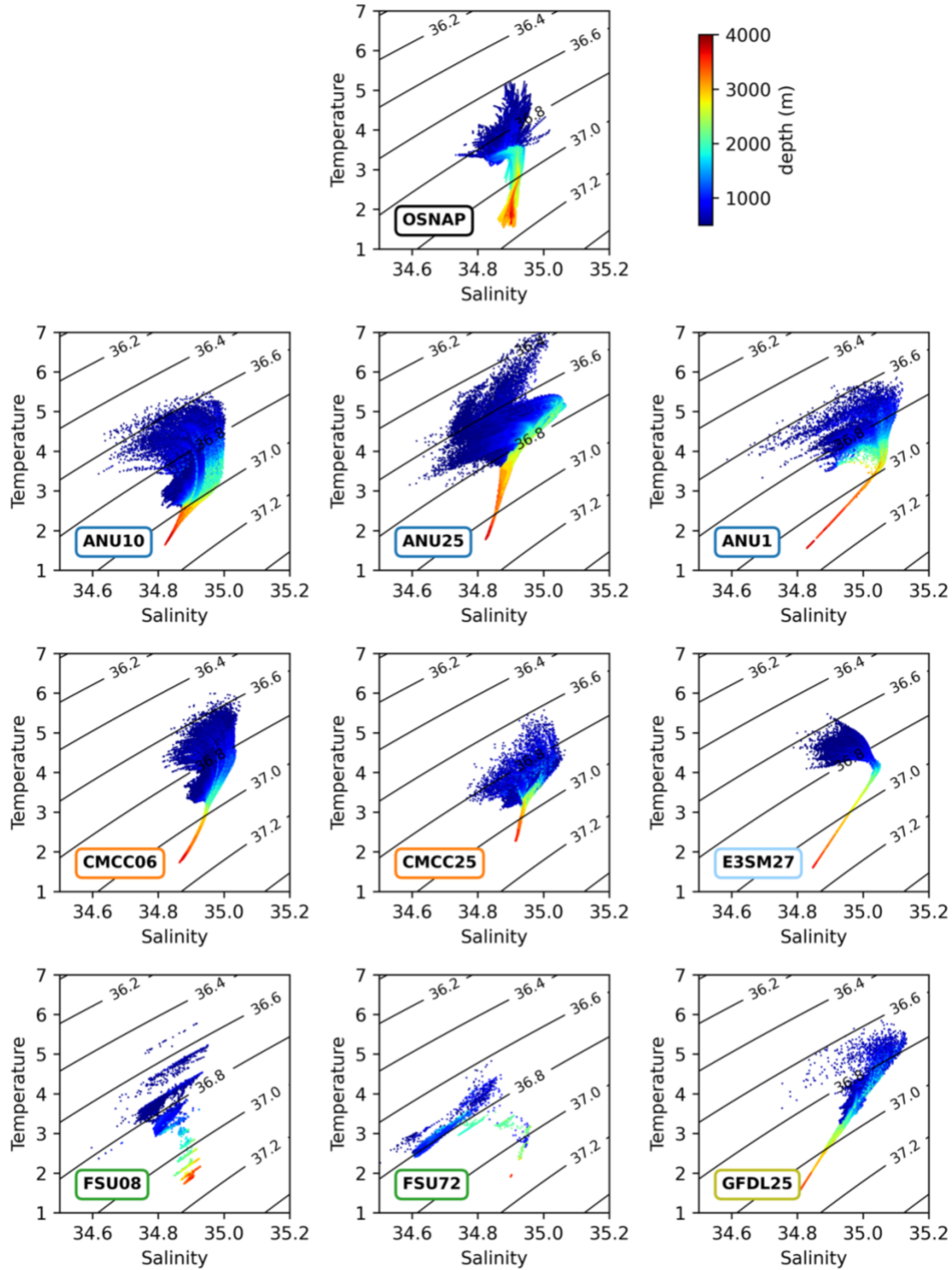


Figure 14. Monthly mean potential temperature – salinity diagrams at OW for depths > 500 m from OSNAP and from ANU10, ANU25, ANU1, CMCC06, CMCC25, E3SM27, FSU08, FSU72, and GFDL25. The background density contours are based on σ_2 densities. The colors represent depth.

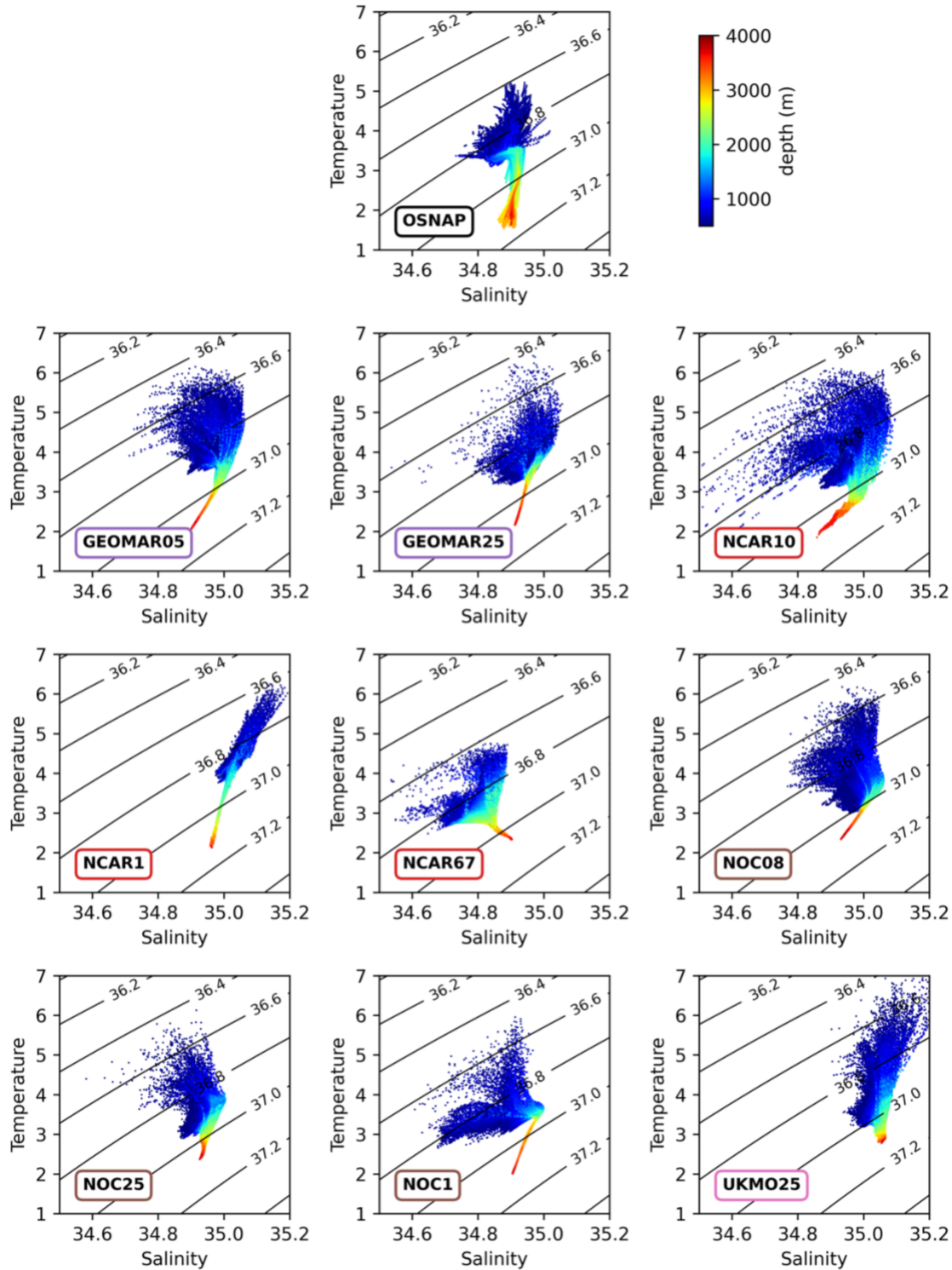


Figure 15. Same as in Fig. 14, but for GEOMAR05, GEOMAR25, NCAR10, NCAR1, NCAR67, NOC08, NOC25, NOC1, and UKMO25.

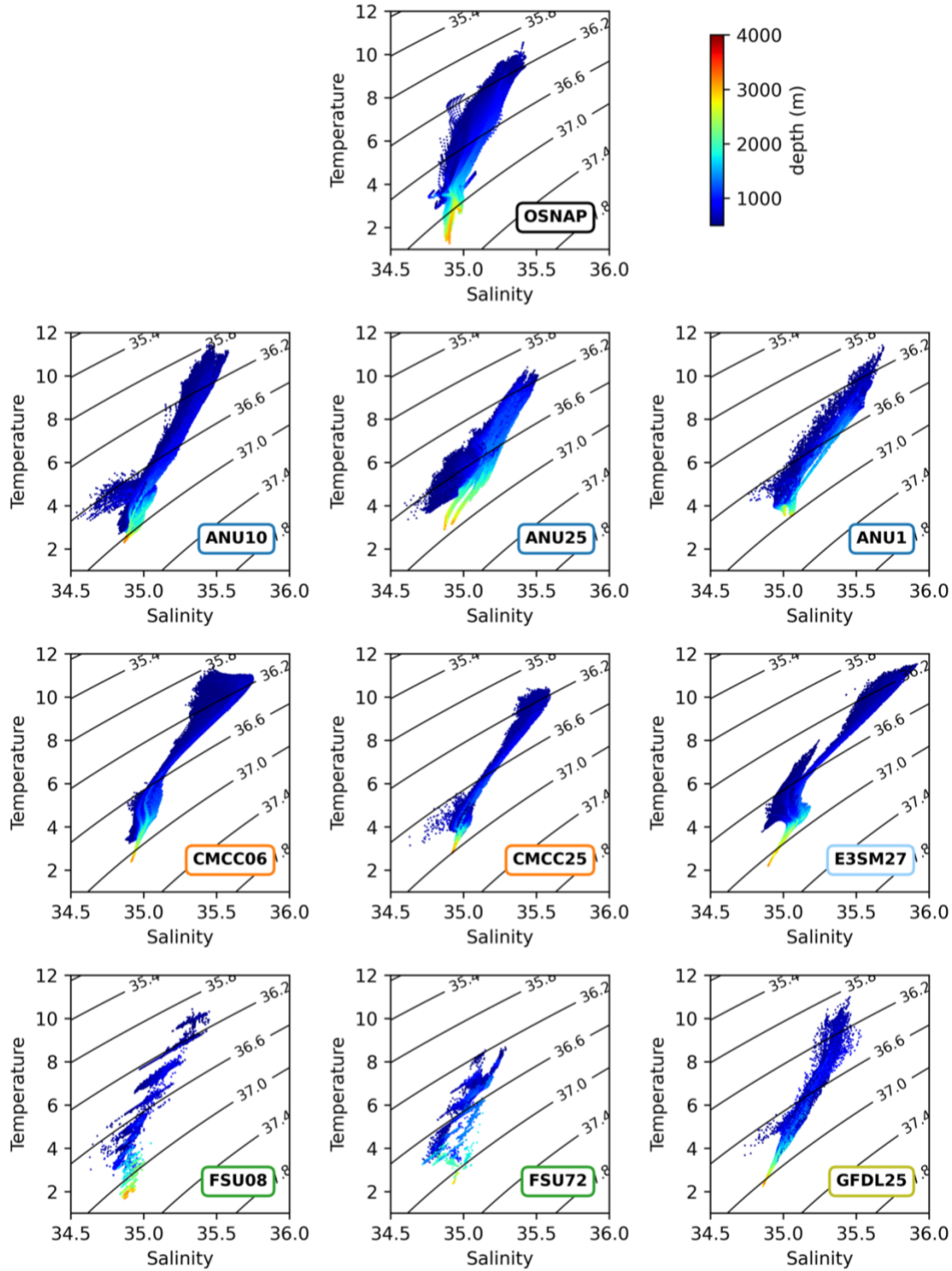


Figure 16. Same as in Fig. 14, but for potential temperature – salinity at OE.

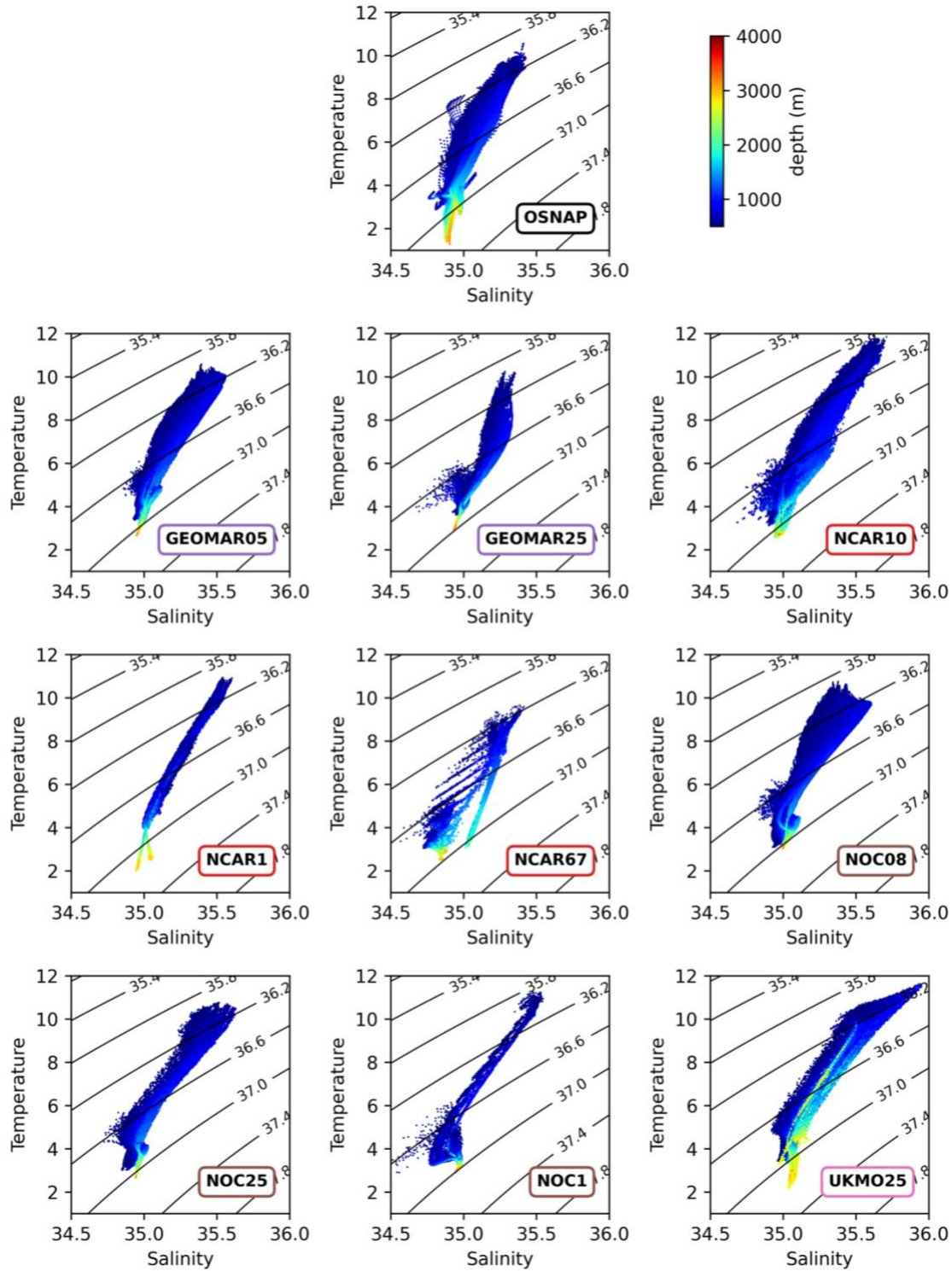


Figure 17. Same as in Fig. 15, but for potential temperature – salinity at OE.

8 Temperature, Salinity, and Density Biases

Because upper-ocean hydrographic properties can significantly affect mixed layer depths and deep convection, impacting overturning transports, we present the scatter plots of the upper-ocean (0 – 700 m) and section-average T, S, and σ_2 biases against the respective maximum transports in σ_2 space at OW and OE in Fig. 18. Thus, the figure is intended to provide a quantitative assessment of these biases and their relationships with the overturning transports. The biases are computed with respect to the gridded T and S data from the OSNAP observations (Sect. 2.1). At OW, the number of simulations with negative and positive T biases is roughly evenly split with all, but two, within a range of -0.5 and $+0.5$ °C (Fig. 18a). The exceptions are FSU72 and NCAR1 with respective biases of about -1.15 and 0.70 °C. There is no statistically significant relationship between these T biases and the transports. In contrast, the relationship between the S biases and the transports is significant, showing generally larger (smaller) transports with positive (negative) S biases (Fig. 18b). Many of the simulations have biases within a range of -0.1 and $+0.1$ psu, but most (12) have a salty bias. While the largest fresh biases occur in ANU25 and FSU72 with -0.21 psu, the largest salty bias is in NCAR1 with $+0.22$ psu. In density, except for ANU25 and E3SM27, the biases are within a range of about -0.03 and $+0.10$ kg m^{-3} , with no significant relationship with the transports (Fig. 18c). ANU25 and E3SM27 show negative density biases of about -0.21 and -0.15 kg m^{-3} , respectively. In more than half of the simulations, T and S biases compensate each other in their contributions to density. At OE, both T and S biases are strongly correlated with the transports, indicating generally larger transports with warmer and saltier biases (Figs. 18d and e). However, a large majority of the simulations has cold biases of up to about -0.9 °C, with negative and positive S biases evenly split. NCAR1 has the largest warm ($\sim +1.1$ °C) and salty (0.22 psu) biases among all the models. ANU1 is a close second with warm and salty biases of $> +0.5$ °C and about $+0.2$ psu, respectively. All these biases substantially compensate each other in density, producing no significant relationship between the density biases and the transports (Fig. 18f). Most of the simulations show a positive density bias of $< +0.1$ kg m^{-3} . We note that the sign and magnitude of these T, S, and σ_2 biases do not reveal any systematic dependencies on model resolution.

Finally, we show the scatter plots of the spatial-averaged T, S, and σ_2 density biases against the maximum total transport in σ_2 space in Fig. 19, where the biases are with respect to the EN4

dataset (Good et al., 2013). A goal is to briefly explore if the above relationships between the overturning transports and the upper-ocean hydrographic properties change when broader regions are considered – as done in previous studies (e.g., Danabasoglu et al., 2014). So, the biases are calculated in the upper 700 m separately for the Labrador Sea (60°-45°W and 50°-65°N) and Irminger Sea (45°-25°W and 50°-65°N) regions (see Fig. 1 for these regions), chosen as two representative areas. In the LS, there are generally larger (smaller) overturning transports with positive (negative) T and S biases, with most simulations showing warm and salty biases (Figs. 19a and b). While FSU72 has the largest cold bias with -0.75 °C, GEOMAR05, NCAR1, and UKMO25 are the warmest models with biases of slightly larger than $+0.5$ °C. In salinity, ANU25 and E3SM27 are the freshest models – both with biases of around -0.2 psu, while UKMO25 has the largest salty bias with 0.4 psu. These T and S biases partially compensate each other in their contributions to density in 13 simulations, but the resulting density biases in the LS are all positive except for ANU25 and E3SM27 (Fig. 19c). These positive biases primarily reflect those of S as density changes are largely determined by S at low temperatures. No statistically significant relationship exists between the LS density biases and the transports for the LS. In the Irminger Sea, the simulations show generally cold biases, with an even split of fresh and salty biases among the simulations (Figs. 19d and e). There is a tendency towards larger (smaller) overturning transports with positive (negative) T and S biases, but this relationship is statistically significant only for S. ANU10 and FSU72 have the largest cold and warm biases with about -0.85 °C and $+0.65$ °C, respectively. E3SM27 and UKMO25 bracket the S biases on opposite sides with bias magnitudes of ~ 0.2 psu. As in the LS, T and S biases partially compensate each other in their contributions to density in 12 simulations in the Irminger Sea (Fig. 19f). The resulting density biases are largely positive, due either to negative T or positive S biases. Again, there is no statistically significant relationship between the Irminger Sea density biases and the transports. As in Fig. 18, the sign and magnitude of these broader region T, S, and σ_2 biases do not show any systematic dependencies on model resolution.

The result that generally larger transports are associated with positive S biases appears to be a robust feature of model simulations as also documented in, e.g., Danabasoglu et al. (2014) and Lin et al. (2023) for a large set of FOSI and coupled simulations, respectively. Furthermore, Jackson & Petit (2022) also report stronger mean overturning and larger variability in saline models in the LS, compared to those with a fresher LS. Partial compensation of T and S biases in

their contributions to density has been reported also in previous studies, e.g., Danabasoglu et al. (2014). Recently, Zou et al. (2020) and Lozier (2023) provided observation-based evidence for similar compensations for the LS (or OW) region. Thus, while such compensations seem to be a robust finding, the degree of compensation varies considerably among simulations as discussed above. Biases in simulations arise from various model deficiencies due to, e.g., flow pathways, lateral and vertical mixing, missing process, and surface fluxes. It is likely that the resulting T and S biases significantly impact the degree of density compensation among the simulations.

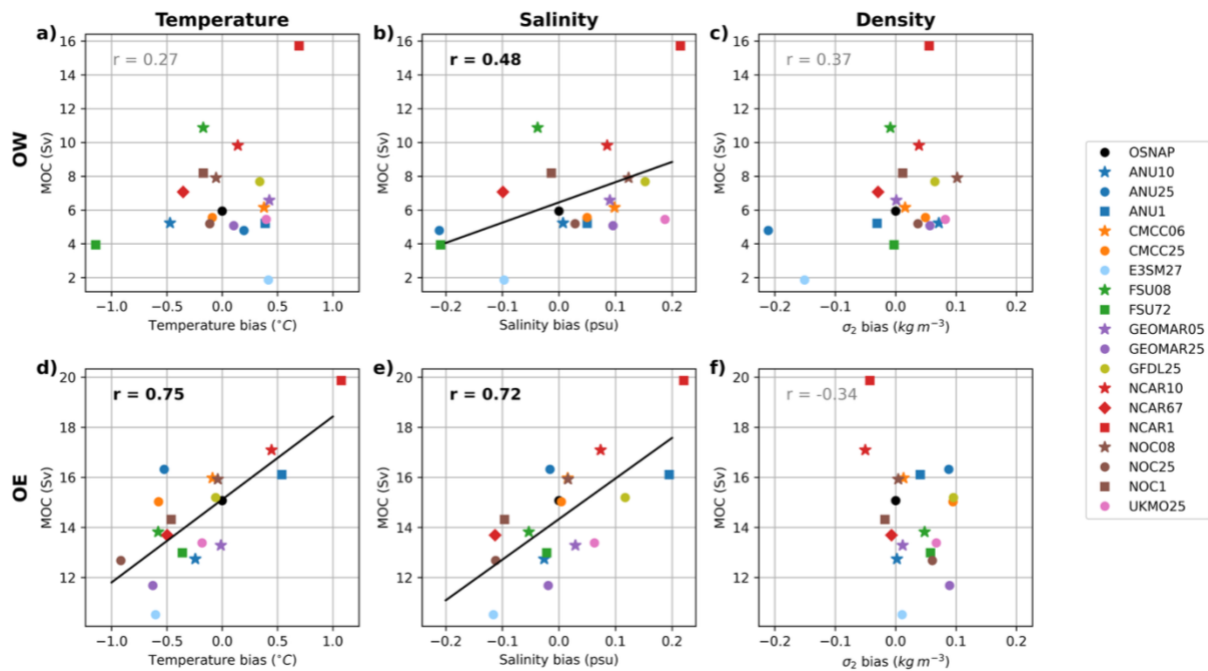
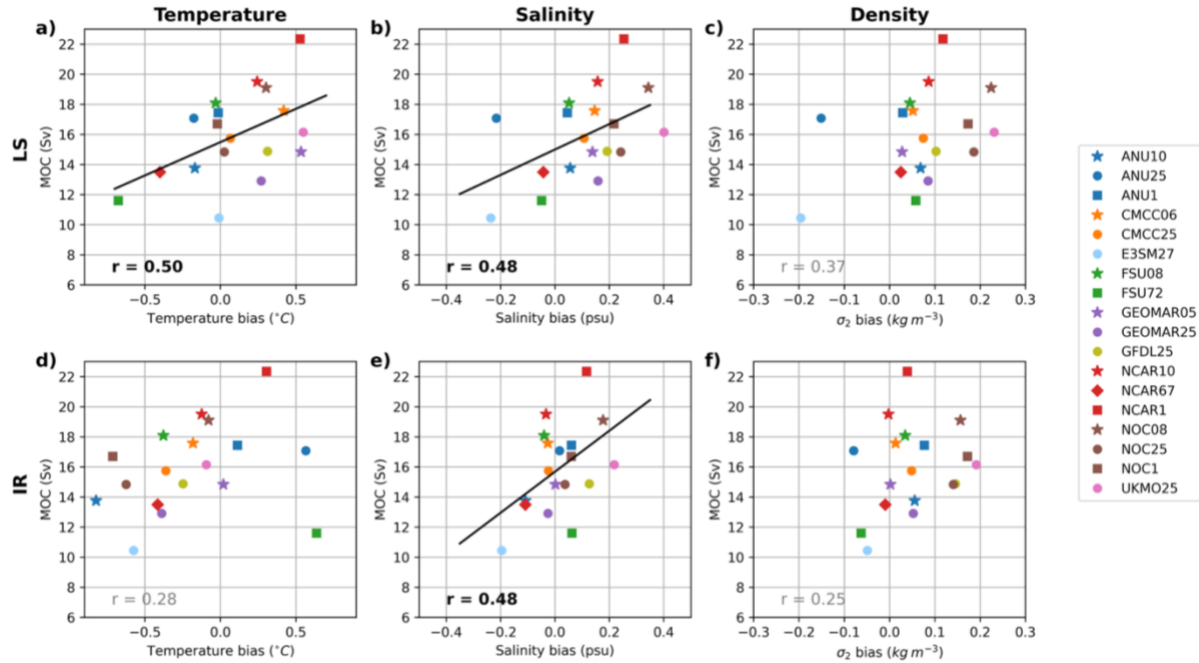


Figure 18. Scatter plots of the upper-ocean (0-700 m) and section average, time-mean (a, d) temperature, (b, e) salinity, and (c, f) σ_2 density biases against the time-mean maximum transports in σ_2 space at OW (top panels) and OE (bottom panels). The black dots in each panel show the OSNAP transports plotted against no bias. The LR, MR, and HR simulations are indicated by squares, circles, and stars, respectively. NCAR67 is shown as a diamond. The correlation coefficients (excluding OSNAP) are included in each panel with the bold font indicating statistical significance at the 95% confidence level, calculated using a 2-sided Student's t-test. The regression lines are also shown in panels with statistically significant correlations.



950 *Figure 19.* Scatter plots of the Labrador Sea (LS; upper panels) and the Irminger Sea (IR; lower panels) upper-ocean (0–700 m average), time-mean (a, d) temperature, (b, e) salinity, and (c, f) σ_2 density biases against the time-mean maximum total transport in σ_2 space. The Labrador and Irminger Sea regions are bounded by 60°–45°W and 50°–65°N, and 45°–25°W and 50°–65°N, respectively (the dark and light purple boxes in Fig. 1, respectively). The LR, MR, and HR simulations are indicated by squares, circles, and stars, respectively. NCAR67 is shown as a diamond. The correlation coefficients (excluding OSNAP) are included in each panel with the bold font indicating statistical significance at the 95% confidence level, calculated using a 2-sided Student’s t-test. The regression lines are also shown in panels with statistically significant correlations.

960 **9 Summary and Conclusions**

We have presented a comparison of simulated and observed transports and related properties, including hydrographic characteristics, across the OSNAP sections for the ~2014-2022 observational period. Our effort aims to provide a benchmark for the modeling community for evaluations of their simulations at OSNAP, considering both depth and density space transports.

965 There are 9 participating groups from around the world providing 18 simulations with 6 different ocean models. These FOSI simulations use a common set of atmospheric datasets, largely

following the OMIP protocol. The horizontal resolutions of the simulations range from coarse nominal 1° to eddy-resolving resolutions of 0.1° - 0.05° . In the vertical, many of the simulations use depth / level coordinates, but a few simulations employ hybrid coordinates. The number of
970 vertical levels / layers varies from 36 to 98, with most models using between 46 and 75.

Our analysis clearly demonstrates that the simulated transports are, in general, in broad agreement with those of observational estimates. Specifically, the transports are larger at OE than at OW with the total transports dominated by those of OE. There are, of course, many differences between the simulations and observations as well as among the individual simulations in details
975 of the transport properties. These include differences (or biases) in the maximum transport densities, transport directions and magnitudes in a given density class or depth, phase of the seasonal cycle of the transports, and T and S properties. A notable difference from OSNAP occurs at OE where a large majority of the simulations have positive transports with negative slopes for densities $< \sim 27.3 \text{ kg m}^{-3}$ (in σ_0 space), contrasting with observations which show a
980 much steeper negative density slope and nearly no net flow for densities $< 27.2 \text{ kg m}^{-3}$ (Fig. 6). There are also seemingly small differences in high density classes at OW. While these high-density transports are themselves relatively small, they can play an outsized role in downstream low-frequency AMOC variability (Yeager et al., 2021). NCAR1 seems to be an outlier in its representation of transports at OW with its rather large maximum transport magnitude.

985 Analyzing overturning circulations in both depth and density space together provides a more complete picture of overturning properties and features. Our preferred approach uses binned southward and northward transports in Sv as a function of depth and density as a starting point, similar to that used in Zhang & Thomas (2021). These depictions provide a clear view of how these transports are distributed across both depth and density space. They can then be summed or
990 aggregated either in depth or density space to produce the familiar overturning transport profiles. In both the simulations and observations, northward and southward flows substantially cancel each other at a given depth or density, producing much smaller net transports. Such cancellations tend to be much more prominent (larger) in depth space than in density space. As discussed in Zhang & Thomas (2021), these cancellation differences in depth- and density-space depend on
995 density differences of horizontally circulating water masses, i.e., isopycnal slopes. In general, the simulations seem to capture the observed transport features better at OE than OW. Not surprisingly, the total velocity and transport profiles tend to agree better between the simulations

and observations due to summations involved. However, actual binned transports show large differences in their depth and density ranges among the simulations and with the observations, i.e., similar-looking northward or southward transports may occur at differing depths and / or densities.

The simulations show T and S biases of both signs in the upper ocean at both OW and OE. Statistically significant relationships exist between overturning transports and S biases at OW, and transports and both T and S biases at OE. Specifically, larger (smaller) transports are associated with positive (negative) T and S biases. In about half of the simulations, T and S biases compensate each other in their contributions to density, and there is no evident relationship between density biases and the corresponding section transports. When broader regions are considered for such bias calculations, i.e., the LS and the Irminger Sea rather than just the OSNAP sections, we again find larger (smaller) overturning transports with positive (negative) T and S biases, but no such clear relationship with density biases. The LS typically shows warm and salty biases. In contrast, the simulations show mostly cold biases in the Irminger Sea region, with roughly an even split of fresh and salty biases among the simulations. While the LS density biases are largely determined by those of salinity, both temperature and salinity biases contribute to the density biases in the Irminger Sea. For both the OSNAP sections and the broader regions considered here, the sign and magnitude of T, S, and σ_2 biases do not show any systematic dependencies on model resolution.

We note that generally larger transports associated with positive salinity biases seem to be a robust result, supported by previous modeling studies. Similarly, presence of density compensating T and S biases (or anomalies) is also supported by several earlier modeling and observation-based studies. However, the degree of such compensations obviously depends on the magnitudes of the respective T and S biases which arise from various model deficiencies. If the amount of the newly formed dense water exported out of the LS is crucially determined by a very delicate compensation of T and S contributions to density as argued by Zou et al. (2020) and Lozier (2023), it will be rather challenging for models to get that balance *right* in the presence of many deficiencies.

The transport profiles from high-resolution simulations show better agreement with OSNAP than those of the low- and medium-resolution simulations, particularly in the high-density classes.

There are also significant improvements in the representation of the seasonal cycle of the transports as well as the transports at OW with the high-resolution version of the NCAR model compared to its low-resolution counterpart. However, for some of the other metrics considered in our analysis, the high-resolution simulations face similar challenges as the low- and medium-resolution ones, with no obvious improvements. These issues may be related to different levels of bias compensations or to differences in the representation of certain processes, such as overflows and (sub)meso-scale eddies, across resolutions.

1035 An important finding is that when transports are calculated in σ_2 space, rather than the σ_0 space used in observations, transports at both OW and OE increase. Specifically, in observations, the OE transport increases by 1.1 Sv from 12.9 to 14.0 Sv, while the OW transport increases by 1.5 Sv from 3.8 to 5.3 Sv, representing a reduction of the OE / OW transport ratio from 3.4 to 2.6. On average, model simulations show increases of 2.53 and 1.18 Sv for OW and OE, respectively.

1040 A comparative measure of these changes, also taking the changes in the OE transports into consideration, indicates that the relative contribution of OW transports increase by about 35% in both observations and simulations. As discussed in Section 2.5, we think that using potential densities referenced to a depth of 2000 m provides a more accurate depiction of deep transports relevant for our analysis, better representing effects of pressure on density. Therefore, we
1045 recommend employing σ_2 densities going forward.

When transports are reported in density space, it is important to provide details of exactly how they are obtained for apples-to-apples comparisons. Specifically, the density space overturning timeseries usually use maximum transports obtained from monthly mean transport profiles. Then, these monthly maximum transports are averaged to produce, say, annual-mean values. Due
1050 to the inherent nonlinearity of this process, when annual-mean transports are calculated as averages of the monthly mean transport profiles, maximum transports based on these annual-mean transports differ modestly from those obtained with the former approach. This difference results from substantial changes of the density at which the maximum transport occurs each month. In contrast, such a problem with the nonlinearity of the overturning strengths is much
1055 more muted in depth space calculations as the depth of the maximum transport does not change substantially from month to month (see Fig. S1 of Lozier et al., 2019). Transports computed from averaged profiles will be always smaller than those derived from averaging the monthly

maximum transports. Indeed, these differences can be ~ 2 Sv for the OE and total transports in observations (~ 15 Sv vs. ~ 13 Sv) as reported in Lozier et al. (2019).

1060 The OSNAP observations have been incredibly valuable in providing separate overturning transport estimates for the eastern subpolar gyre and the LS sides. These datasets have been used in evaluation of model simulations as described in this manuscript. Now available for the 8-year period from August 2014 to July 2022, the OSNAP observations provide a comprehensive view of the respective roles of the eastern and western sections on inter-annual (or sub-decadal) time
1065 scales. While the model simulations are in general agreement with the OSNAP observations regarding the respective transport magnitudes during this observational period, studies that attribute a prominent role for the LS primarily focus on decadal-to-multi-decadal time scales, which cannot be evaluated against observations yet. Therefore, it is important to continue the OSNAP observational program so that they can provide future guidance on longer time scales.

1070 **Table 1.** Summary of the ocean and sea-ice models in alphabetical order according to the
participating group name (first column). The table includes, in order, the label used in this study
for the listed configuration and resolution; the name of the combined ocean – sea-ice
configuration (if any); the ocean model name and its version number; the sea-ice model name
and its version number; vertical coordinate and number of layers / levels in parentheses; and the
1075 nominal horizontal resolution in degrees.

Group	Label	Configuration	Ocean Model	Sea-ice Model	Vertical Grid (number of levels)	Nominal Horizontal Resolution (°)
ANU	ANU10	ACCESS-OM2-01	MOM 5.1	CICE 5.1.2	z^* (75)	0.1
	ANU25	ACCESS-OM2-025	MOM 5.1	CICE 5.1.2	z^* (50)	0.25
	ANU1	ACCESS-OM2	MOM 5.1	CICE 5.1.2	z^* (50)	1
CMCC	CMCC06	GLOB16	NEMO 3.6	LIM 2	z (98)	0.0625
	CMCC25	ORCA025	NEMO 3.6	CICE 4.1	z (50)	0.25
FSU	FSU08		HYCOM	CICE 4	hybrid (36)	0.08
	FSU72		HYCOM	CICE 4	hybrid (41)	0.72
GEOMAR	GEOMAR05	VIKING20X	NEMO 3.6	LIM 2	z (46)	0.05 / 0.25 ^a
	GEOMAR25	ORCA025	NEMO 3.6	LIM 2	z (46)	0.25
GFDL	GFDL25	OM4	MOM 6	SIS 2	hybrid (75)	0.25
LANL	E3SM27		MPAS-Ocean	MPAS-SeaIce	z^* (64)	~0.27 (~30 km) ^b
NCAR	NCAR10		POP 2	CICE 4	z (62)	0.1
	NCAR1		POP 2	CICE 4	z (60)	1
	NCAR67		MOM 6	CICE 6	hybrid (75)	0.67
NOC	NOC08	GO8p7	NEMO 4.0.4	SI3	z^* (75)	0.08

	NOC25	GO8p7	NEMO 4.0.4	SI3	z^* (75)	0.25
	NOC1	GO8p7	NEMO 4.0.4	SI3	z^* (75)	1
UKMO	UKMO25	GO8p7	NEMO 4.0.4	SI3	z^* (75) ^c	0.25

^a Uses a 0.05° Atlantic grid (33.5°S to ~65°N), two-way nested within a global 0.25° grid (ORCA025).

1080 ^b Uses an unstructured grid with a nominal horizontal resolution of 30 km which is roughly 0.27° at the Equator.

^c Uses embedded hybrid terrain-following layers only in the Nordic overflow regions via localized multi-envelope generalized vertical coordinates.

Table 2. Summary of the surface freshwater / salt fluxes and sea surface salinity (SSS) restoring choices for each model configuration (first column). The salt vs. water column indicates the type of surface fluxes used for hydrological forcing with water and salt denoting real freshwater and virtual salt fluxes, respectively. The SSS restoring time scales are given in days over a 50 m length scale. The NEMO-based models convert salinity restoring to a freshwater flux (denoted as fw in the column). The other groups apply salinity restoring as a salt flux. The region column indicates the region over which the salinity restoring is used. An asterisk denotes that a limit of 0.5 psu is imposed to constrain the magnitude of mismatch between the model and observed SSS. A superscript + indicates that surface restoration is capped to not exceed 4 mm day⁻¹ in magnitude. The under sea ice column shows whether restoring is applied under sea-ice covered areas. The remove global-mean restoring column indicates whether the model subtracts the global mean of restoring fluxes. Finally, the normalize freshwater fluxes column refers to whether some sort of normalization to the sum of precipitation, evaporation, and runoff fluxes is applied to reduce drift.

Label	Freshwater Fluxes via Virtual Salt vs. Water	SSS Restoring Time Scale (day)	SSS Restoring Region	SSS Restoring Under Sea Ice	Remove Global-Mean SSS Restoring	Normalize Freshwater Fluxes
ANU10 ^a	Water	455	Global*	Y	Y	Y
ANU25 ^a	Water	455	Global*	Y	Y	Y
ANU1 ^a	Water	455	Global*	Y	Y	Y
CMCC06	Water	365 (fw)	Global	N	N	Y
CMCC25	Water	182.5 (fw)	Global	N	N	Y
E3SM27	Water	365	Global	Y	Y	N
FSU08 ^b	Salt	60	Global*	Y	Y	N
FSU72 ^b	Salt	60	Global*	Y	Y	N
GEOMAR05	Water	365	Global*, c	N	N	Y
GEOMAR25	Water	365	Global*, c	N	N	Y
GFDL25	Salt	300	Global	Y	Y	Y
NCAR10	Salt	365	Global	Y	Y	Y
NCAR1	Salt	365	Global	Y	Y	Y
NCAR67	Salt	300	Global	Y	Y	Y
NOC08	Water	1500 (fw)	Global ⁺	Y	N	N
NOC25	Water	1500 (fw)	Global ⁺	Y	N	N
NOC1	Water	1500 (fw)	Global ⁺	Y	N	N
UKMO25	Water	1500 (fw)	Global ⁺	Y	N	N

- 1100 ^a The restoring dataset is based on the 0.25° World Ocean Atlas 2013 v2 decav monthly climatology, filled into land via a conjugate gradient method. The 0-m and 10-m data are then averaged, horizontally smoothed, and smoothly interpolated onto the model grid.
- ^b The Generalized Digital Environmental Model (GDEM4) monthly climatology is used as the restoring dataset.
- 1105 ^c Salinity restoring is suppressed where runoff is applied as well as within an 80-km wide band around Greenland to not interfere with enhanced freshwater input from melting ice sheets.

Appendix A: Model descriptions

A1 Australian National University (ANU)

ACCESS-OM2, ACCESS-OM2-025, and ACCESS-OM2-01 are global coupled ocean – sea-ice model configurations at nominal horizontal grid spacings of 1° , 0.25° , and 0.1° , respectively, developed by the Consortium for Ocean - Sea Ice Modelling in Australia. The configurations are respectively labeled as ANU1, ANU25, and ANU10 in this manuscript. They are based on those described by Kiss et al. (2020) but updated with several improvements described below and in the Supporting Information of Solodoch et al. (2022). The two coarser resolutions also comprise the ocean and sea-ice components for Australia’s ACCESS-CM2 (Bi et al., 2020) and ACCESS-CM2-025 (Huneke et al., 2025) coupled climate models.

The ocean model is MOM5.1 (Griffies, 2012) and the sea-ice model is CICE5.1.2 (Hunke et al., 2015); these are coupled every ocean baroclinic timestep (equal to the sea ice thermodynamics timestep) via OASIS3-MCT v.2.0 (Valcke et al., 2013). At each resolution, the configurations use a common tripolar (Murray, 1996) horizontal B-grid for MOM and CICE. Grid lines are aligned with latitude and longitude south of 65°N , with Mercator spacing between 65°N and 65°S in ANU25 and ANU10, and they have a more complicated latitudinal dependence with a meridional refinement to $1/3^\circ$ near the Equator in ANU1 (Bi et al., 2013). The ocean vertical coordinate is z^* , with a smoothly varying spacing chosen to optimize the resolution of baroclinic modes (Stewart et al., 2017). There are 50 levels ranging from 2.3-m thick at the surface to 219.6 m in the abyss in ANU1 and ANU25, and 75 levels ranging from 1.1 to 198.4-m thick in ANU10. Bathymetry is represented with partial cells (Adcroft et al., 1997; Pacanowski & Gnanadesikan, 1998). The topography at all three resolutions is based on GEBCO 2014 v20150318 30 arc-second data (replacing the legacy topography files used at 1° and 0.25° in Kiss et al., 2020), with hand-edits in ANU1 to improve the flow in some straits, e.g., the Denmark Strait, Iceland-Faroe Strait, the Strait of Gibraltar, the Lombok, Ombai, Timor, Makassar Straits, the Caribbean, and the Drake Passage.

The configurations are designed to be as similar as possible at the three resolutions, but there are some unavoidable differences due to the differing resolution of eddies. The Gent and McWilliams (GM; 1990) scheme is used in ANU25 and ANU1 to parameterize advective transports due to unresolved eddies via a skew diffusive implementation (Griffies, 1998). The

GM diffusivity has a spatial structure determined according to the baroclinic zone setting of Griffies et al. (2005) and has a maximum value of $200 \text{ m}^2 \text{ s}^{-1}$ in ANU25 and $600 \text{ m}^2 \text{ s}^{-1}$ in ANU1. A neutral diffusivity for tracers (Griffies et al., 1998) is included with a horizontal scaling according to Hallberg (2013) with a maximum value of $200 \text{ m}^2 \text{ s}^{-1}$ in ANU25 and a constant value of $600 \text{ m}^2 \text{ s}^{-1}$ in ANU1. Neither of these parameterizations are active in ANU10. The K-profile parameterization (KPP; Large et al., 1994), Lee et al. (2006) barotropic tidal drag and mixing, and the Simmons et al. (2004) bottom intensified mixing schemes are used, with background vertical viscosities of $10^{-4} \text{ m}^2 \text{ s}^{-1}$ in all configurations and background vertical diffusivities following Jochum (2009) for ANU1, no background vertical diffusivity in ANU25, and a constant value of $10^{-6} \text{ m}^2 \text{ s}^{-1}$ in ANU10. ANU1 also uses downslope mixing (Beckmann and Doscher, 1997; Doscher and Beckmann, 2000; Campin and Goosse, 1999). The Fox-Kemper et al. (2008) parameterization of submesoscale eddy-driven mixed-layer restratification is used in all configurations.

In all three configurations, the ocean equations of state and freezing temperature are from Jackett et al. (2006). The prognostic salinity and temperature variables are practical salinity and conservative temperature (converted from potential temperature initial conditions via TEOS-10). Sea surface salinity is restored to World Ocean Atlas 2013 v2 (WOA13) monthly climatology with a piston velocity of 50 m over 455 days (including under sea ice) in all 3 simulations. The ocean albedo is latitude dependent (Large and Yeager, 2009). The CICE configuration uses 5 thickness categories, with four ice layers and one snow layer for the thermodynamics, and an ice salinity (for the purposes of coupling) of 5 psu. The wind stress calculation uses relative velocity over both the ocean and sea ice.

Runs at all three resolutions started from initial temperature and salinity from the WOA13 January-mean climatology. ANU1, ANU25, and ANU10 were forced by 6, 6, and 4 consecutive 61-year cycles, respectively, of the JRA55-do v1.4.0 atmospheric datasets for the 1958-2018 period. The final cycle was then extended through 2019 using JRA55-do v1.5.0, and then through 2020-2022 inclusive using JRA55-do v1.5.0.1. This last cycle constitutes the data used in this study. Output from ANU1 and ANU25 were contributed to CMIP6 through the OMIP2 experiments (see Mackallah et al., 2022).

1165 The performance of ACCESS-OM2 at different resolutions is assessed and compared to other models and / or to available observations for the Arctic Ocean in Wang et al. (2024); for mixed layer depths in Treguier et al. (2023); for the deep Atlantic multidecadal variability in Yang et al. (2024); and (for the older Kiss et al. (2020) configurations) for the AMOC in Hirschi et al. (2020).

1170 **A2 Centro Euro-Mediterraneo sui Cambiamenti Climatici (CMCC)**

The CMCC foundation provided the global ocean – sea-ice model configurations, both built on the NEMO modeling framework, at nominal horizontal grid spacings of 0.25° (ORCA025) and 0.0625° (GLOB16). The configurations are respectively labeled as CMCC25 and CMCC06 in this manuscript. Details of the latter configuration and an evaluation of its simulation are given in
1175 Iovino et al. (2023).

CMCC06 is a global, eddying configuration of the ocean and sea-ice system. The model is based on its first implementation documented in Iovino et al. (2016), where the ocean component is upgraded from version 3.4 to version 3.6 stable (Madec and the NEMO Team, 2016). Its high computational cost does not permit long evaluation simulations and, therefore, it is simply set up
1180 using our best practices based on a forecasting application (Cipollone et al., 2020; Masina et al., 2021).

This eddy-rich configuration makes use of a non-uniform tripolar grid with a nominal 1/16° horizontal resolution (6.9 km at the Equator, reducing poleward). The grid consists of an isotropic Mercator grid between 60°S and 20°N and a non-geographic quasi-isotropic grid north
1185 of 20°N. The minimum grid spacing is ~2 km around Victoria Island, and the meridional scale factor is fixed at 3 km south of 60°S. Ocean and sea ice are on the same horizontal grid. The vertical coordinate system is based on fixed depth levels and consists of 98 vertical levels with a grid spacing increasing from approximately 1 m near the surface to 160 m in the deep ocean.

The ocean component is a finite-difference, hydrostatic, primitive-equation general circulation
1190 model, with a linearized free sea surface, a free-slip lateral friction condition, and an Arakawa C-grid. A biharmonic viscosity scheme with a coefficient of $-0.5 \times 10^{10} \text{ m}^4 \text{ s}^{-1}$ is used in the horizontal directions. Lateral tracer diffusion, set at $80 \text{ m}^2 \text{ s}^{-1}$, is along isoneutral surfaces using a Laplacian mixing. Tracer advection uses a total variance dissipation (TVD) scheme (Zalesak,

1195 1979). Vertical mixing is achieved using a turbulent kinetic energy (TKE) closure scheme
(Blanke & Delecluse, 1993). Background coefficients of vertical diffusion and viscosity are 1.2×10^{-5} and $1.2 \times 10^{-4} \text{ m}^2 \text{ s}^{-1}$, respectively. Vertical eddy mixing of both momentum and tracers is enhanced in case of static instability. The turbulent closure model does not apply any specific modifications in ice-covered regions. Bottom friction is quadratic, and a diffusive bottom boundary layer scheme is included. All configurations use the EOS80 equation of state (Fofonoff & Millard, 1983), with potential temperature and practical salinity as prognostic state variables.

1200 The ocean component is coupled to the Louvain-la-Neuve sea Ice Model version 2 (LIM2; Timmermann et al., 2005) for its smaller computational cost compared to the more complex LIM3 code (Rousset et al., 2015; Uotila et al., 2017) available in NEMOv3.6. LIM2 is integrated as an internal module in NEMO. It uses a three-layer model for the vertical heat conduction
1205 within snow and ice, featuring a single sea ice category. The ice dynamics are calculated according to external forcing from wind stress, ocean stress, and sea surface tilt and internal ice stresses using a C-grid elastic–viscous–plastic rheology (Bouillon et al., 2013).

The eddy-permitting ORCA025 configuration used here is the ocean and sea-ice components of the CMCC coupled climate model (CMCC-CM2; Cherchi et al., 2019) and Earth system model (CMCC-ESM2; Lovato et al., 2022). This framework is based on the Community Earth System Model (CESMv1.2), in which we replaced the original ocean component with NEMOv3.6 (Fogli & Iovino, 2014). The ocean component is coupled to the Community Ice Code CICEv4.1 (Hunke & Lipscomb, 2010). CMCC25 has a nominal resolution of 0.25° , with 50 vertical levels, ranging from 1 to 400 m. The ORCA025 physical core as implemented for this OMIP simulation
1215 is similar to the lower resolution configuration described in Tsujino et al. (2020), except for resolution-dependent features, such as the eddy-induced tracer advection term which is not used in ORCA025. This configuration uses a biharmonic horizontal viscosity of $-1.8 \times 10^{11} \text{ m}^4 \text{ s}^{-1}$, a Laplacian tracer diffusivity of $300 \text{ m}^2 \text{ s}^{-1}$, and a background vertical diffusivity and viscosity of 1.2×10^{-5} and $1.2 \times 10^{-4} \text{ m}^2 \text{ s}^{-1}$, respectively. The sea-ice model includes energy-conserving
1220 thermodynamics (Bitz & Lipscomb, 1999), multi-category ice thickness (Bitz et al., 2001) with five thickness categories, and elastic–viscous–plastic ice dynamics (Hunke & Dukowicz, 1997). It is solved on the Arakawa B-grid, with the tracer points aligned with the ocean grid. The coupling interface between NEMO and CICE is described in Cherchi et al. (2019) and references therein (Fogli & Iovino, 2014).

1225 Sea surface salinity is restored to the WOA13 v2 monthly climatology. Salinity restoring is applied globally via an equivalent-surface freshwater flux using restoring time scales of 365 and 182.5 days over 50 m in CMCC25 and CMCC06, respectively. There is no salinity restoring under sea-ice-covered areas. The two sea-ice models used in the two systems employ different bulk ice salinity values that affect the salt release from the sea ice to the ocean. In CICE, a reference sea-ice salinity value of 4 psu is used for computing the ice–ocean exchanges. In our version of LIM2, the freshwater (salinity) fluxes between the ice and the ocean assume a constant salinity of 6 psu. Over a sea ice formation and melt cycle, this produces stratification differences among runs and might have an impact on the large-scale ocean circulation. In wind stress calculations, relative winds are used over both ocean and sea ice.

1235 Liquid runoff is deposited along the coast and distributed in the upper 20 m in CMCC25 and at the ocean surface in CMCC06, with no specific enhancement of the mixing in either case. The runoff interpolation in both configurations makes use of a globally conserving method, which also spreads the runoff along the coast, to compute offline remapping weights.

1240 Following the OMIP protocol, the ocean is initially at rest, with a sea level of 0 m and with temperature and salinity from the World Ocean Atlas 2013 v2 (WOA13; Locarnini et al., 2013; Zweng et al., 2013) decav product (averaged from 1955–2012) interpolated on a 0.25° grid. For CMCC25, the initial sea-ice properties are taken from spin-up experiments, while initial ice concentration and thickness for CMCC06 are fixed to 100% with thicknesses of ~3 m north of 70°N and ~1 m south of 60°S.

1245 CMCC25 was integrated for six 61-year cycles (1958-2018) of JRA55-do, while CMCC06 was integrated over a single cycle. Only the first JRA55-do cycle is used for both simulations in this paper which were extended to 2022.

A3 Florida State University (FSU)

1250 FSU-HYCOM is a global configuration of the HYbrid Coordinate Ocean Model (HYCOM) (Bleck, 2002; Chassignet et al., 2003). The vertical coordinate is isopycnic in the stratified open ocean and makes a dynamically smooth and time-dependent transition to terrain following in the shallow coastal regions and to fixed pressure levels in the surface mixed layer and unstratified seas. The sea-ice component uses version 4 of the Community Ice Code (CICE4; Hunke &

Lipscomb, 2010). Two simulations, one with a coarse resolution of 0.72° and the other with an
1255 eddying resolution of 0.08° , are performed. They are referred to as FSU72 and FSU08,
respectively, in the manuscript. The configurations and general features of these simulations are
described in Chassignet et al. (2020). An in-depth evaluation of the Antarctic Circumpolar
Current (ACC) and the AMOC in the South Atlantic Ocean are provided in Xu et al. (2020;
2022).

1260 In FSU72, the resolution is refined to 0.33° near the Equator, and a vertical grid of 41 hybrid
coordinate layers is used. Vertical mixing uses the KPP (Large et al., 1994) with a background
diffusivity of $3 \times 10^{-5} \text{ m}^2 \text{ s}^{-1}$. For horizontal mixing, the simulation uses a combination of a
Laplacian diffusive velocity of 3 cm s^{-1} and a biharmonic diffusive velocity of 5 cm s^{-1} for
1265 interface height smoothing corresponding to the GM isopycnal mixing parameterization, using a
biharmonic operator with a diffusive velocity of 2 cm s^{-1} everywhere, except in the North Pacific
and North Atlantic where a Laplacian operator with a velocity scale of 1 cm s^{-1} is used.

FSU08 has 36 hybrid layers in the vertical. This vertical layer set up was retained to enable
comparisons with previous simulations performed with other atmospheric forcing datasets.

1270 While the vertical resolution in both FSU72 and FSU08 is lower than recommended by Stewart
et al. (2017) for z-coordinate models, the vertical resolution is adequate to represent the first five
baroclinic modes in the mid-latitudes and the large-scale circulation of key water masses in the
Atlantic Ocean (Xu et al., 2023). As in the coarse resolution counterpart, vertical mixing in the
eddying simulation uses the KPP with a background diffusivity of $3 \times 10^{-5} \text{ m}^2 \text{ s}^{-1}$. For horizontal
1275 mixing, the simulation uses a combination of a Laplacian viscosity of $20 \text{ m}^2 \text{ s}^{-1}$ and a biharmonic
diffusive velocity of 1 cm s^{-1} for momentum, a Laplacian diffusive velocity of 0.5 cm s^{-1} for
tracers, and a biharmonic diffusive velocity of 1.5 cm s^{-1} for layer interfaces.

Both simulations are initialized using potential temperature and salinity from the Generalized
Digital Environmental Model (GDEM4; Teague et al., 1990; Carnes, 2009) and are integrated
1280 using the JRA55-do datasets from 1958 to 2022 for one cycle. The Large & Yeager (2009) bulk
formulation is used for turbulent air–sea fluxes. Wind stress is calculated without surface ocean
currents (i.e., using absolute winds). No restoration is applied on the sea surface temperature.
The surface salinity is restored to the monthly GDEM4 climatology over the global domain with

a piston velocity of 50 m over 60 days. In addition, the salinity flux at each time step is adjusted
1285 to ensure a zero net global-mean flux.

A4 GEOMAR

The VIKING20X model configuration is based on NEMO version 3.6. It consists of a 0.05°
Atlantic nest extending from 33.5°S to about 65°N, which is embedded using grid refinement
(AGRIF; Debreu et al., 2008) into a global curvilinear 0.25°-grid ORCA025 configuration with
1290 46 vertical levels. The model discretizes the ocean variables on an Arakawa C-grid and the sea-
ice component LIM2 (Fichefet & Morales Maqueda, 1997) on a B-grid. A parallel ORCA025
configuration without grid refinement in the Atlantic Basin but otherwise with identical settings
as those of the coarse grid in VIKING20X, accompanies the eddy-rich simulations. In this
manuscript, these simulations are referred to as GEOMAR05 and GEOMAR25, respectively.

1295 Numerics include a momentum advection scheme in vector form which conserves both energy
and enstrophy (Arakawa and Hsu, 1990), leading to a good representation of the large-scale,
horizontal flow field (Barnier et al., 2006). Tracer advection is formulated as a two-step flux
corrected transport, total variance dissipation scheme (Zalesak, 1979), ensuring positive-definite
values. Momentum diffusion is given along geopotential surfaces in a bi-Laplacian form with a
1300 viscosity of $15 \times 10^{10} \text{ m}^4 \text{ s}^{-1}$. Tracer diffusion is along iso-neutral surfaces in Laplacian form
with an eddy diffusivity of $300 \text{ m}^2 \text{ s}^{-1}$. Diffusion parameters are adjusted for the nest grid to take
advantage of the increased resolution. As such, the Laplacian parameter for tracers is $60 \text{ m}^2 \text{ s}^{-1}$
and the bi-Laplacian parameter for momentum is $6 \times 10^9 \text{ m}^4 \text{ s}^{-1}$. In both simulations, the
background vertical eddy diffusivity and viscosity are set to $1 \times 10^{-5} \text{ m}^2 \text{ s}^{-1}$ and $1 \times 10^{-4} \text{ m}^2 \text{ s}^{-1}$,
1305 respectively.

Both simulations were run for 6 forcing cycles for the 1958-2019 period. However, at the end of
each cycle, the simulations were extended to 2023. This study uses the solutions from the first
cycles as described in Biastoch et al. (2021) where they are referred to as VIKING20X-JRA-
OMIP and ORCA025-JRA-OMIP. A surface salinity restoring with a piston velocity of 50 m
1310 over 365 days is applied together with a freshwater budget correction that balances the global
surface freshwater fluxes to zero. Specifically for GEOMAR05, the freshwater budget is
calculated on the parent grid, and it is then applied to both the parent and nest grids individually,
in proportion to their respective restoring fluxes. Runoff is provided by JRA55-do and enters the

ocean in the upper-most grid cell in a 0.25° band along the coast with a slightly wider
1315 distribution for the largest rivers. Salinity restoring is suppressed where runoff is applied as well
as within an 80-km wide band around Greenland to not interfere with enhanced freshwater input
from melting ice sheets.

Because the grid resolution is eddy-rich through the whole Atlantic, VIKING20X simulates well
the large-scale circulation including realistic representations of western boundary currents, the
1320 path of the North Atlantic Current into the Northwest Corner, convection in the subpolar North
Atlantic, pathways of deepwater, and the AMOC (Biaostoch et al., 2021; Fox et al., 2022; Rühls et
al., 2021; Fröhle et al., 2022; Petit et al., 2023). Böning et al. (2023) used VIKING20X and
corresponding sensitivity experiments to link Labrador Sea convection to the decadal evolution
of the AMOC.

1325 **A5 Geophysical Fluid Dynamics Laboratory (GFDL)**

The GFDL simulation is based on the OM4 configuration using the Modular Ocean Model
version 6 (MOM6) and the Sea Ice Simulator version 2 (SIS2), as documented in Adcroft et al.
(2019). MOM6 and SIS2 have identical horizontal grids (Arakawa C-grid) and employ a tri-polar
grid following Murray (1996). A Mercator grid spans from about 78°S to 65°N and matches the
1330 tri-polar grid at $\sim 65^\circ\text{N}$. MOM6 uses a vertical Lagrangian-remap algorithm (Hirt et al., 1997;
Bleck, 2002) to generate a hybrid depth-isopycnal vertical coordinate. The OM4 configuration
has a nominal 0.25° horizontal resolution and a hybrid vertical grid with 75 degrees of freedom.
The upper ocean is in the depth coordinate, from a 2-m vertical grid interval near the surface to
 ~ 20 m at 200-m depth. The isopycnal coordinate (referenced to 2,000 dbar) is employed in the
1335 region from the upper thermocline to the abyssal ocean. The ocean bathymetry is derived from a
combination of the GEBCO 30-s gridded topography (Weatherall et al., 2015) and the
International Bathymetric Chart of the Arctic Ocean (Jakobsson et al., 2012). In the manuscript,
this contribution is referred to as GFDL25.

No diffusive mesoscale eddy closure is included. The model uses the energetically constrained
1340 parameterization of the surface boundary layer (ePBL) of Reichl & Hallberg (2018) and the
submesoscale mixed-layer restratification parameterization of Fox-Kemper et al. (2011) with a
submesoscale frontal length scale of 500 m. A biharmonic viscosity is employed, which is the

maximum of the dynamic biharmonic viscosity (coefficient = 0.06) (Griffies & Hallberg, 2000) and the static biharmonic viscosity, $u_4\Delta^3$, with $u_4 = 0.01 \text{ m s}^{-1}$. Here, Δ is the local grid spacing.

1345 SIS2 has five thickness categories and uses four sea ice layers and one snow layer for the vertical thermodynamics. A radiative transfer scheme is included to simulate the vertical profile of shortwave absorption. The OM4 configuration is also used as the ocean – sea-ice component of GFDL’s 4th generation fully coupled climate model CM4 (Held et al., 2019).

The sea surface salinity is restored with a piston velocity of 50 m over 300 days. The simulation
1350 was run for 6 forcing cycles. The first 3 cycles use 60 years each (from 1958 to 2017) and the last 3 cycles are for 61 years each (from 1958 to 2018). The general evaluation of OMIP simulations across multiple ocean – sea-ice models including GFDL OM4 has been documented in Tsujino et al. (2020).

A6 Los Alamos National Laboratory (LANL)

1355 The Energy Exascale Earth System Model (E3SM) version 3 (E3SMv3) builds on previous versions of E3SM (E3SMv2.1, Smith et al., 2024; E3SMv2; Golaz et al., 2022). The ocean component, MPAS-Ocean, solves the hydrostatic, incompressible equations under the Boussinesq approximation on a staggered Arakawa C-grid, using a two-step Adams-Bashford time-stepping. The vertical grid is structured and uses an arbitrary Lagrangian-Eulerian method
1360 with several choices of vertical coordinates (Petersen et al., 2015). The production simulations use a free surface z^* coordinate and 64 vertical levels with thicknesses from 10 m at the surface to over 240 m in the deep ocean with partial bottom cells. The horizontal mesh is unstructured. The new version 3 MPAS-Ocean horizontal mesh used in this paper is an icosahedral mesh of nominal horizontal resolution of 30 km and includes sub-ice-shelf cavity geometry around
1365 Antarctica. The ocean topography is based on GEBCO 2023, updated with BedMachine Antarctica v3 (Morlighem, 2022) on the Antarctic shelves. Because the grid is unstructured and the nominal 30-km horizontal resolution is approximately 0.27° at the Equator, this contribution is referred to as E3SM27 in this manuscript.

The ocean parameterizations of mesoscale eddy effects include isoneutral diffusion following
1370 Redi (1982), tapered near the surface and slope-limited, with a diffusivity of $400 \text{ m}^2 \text{ s}^{-1}$ and a modified GM scheme following Ferrari et al. (2010) using a thickness diffusivity of $600 \text{ m}^2 \text{ s}^{-1}$.

1375 These coefficients are linearly reduced in regions where the resolution lies between 30 and 20 km, and reach zero for resolutions finer than 20 km. Restratification due to mixed layer eddies is represented by a submesoscale scheme following Fox-Kemper et al. (2011), with a minimum frontal width of 1 km and a 2-day mixing time scale. The mixed layer is represented using the KPP scheme with a critical bulk Richardson number of 0.25. A constant background viscosity and diffusivity of $1.0 \times 10^{-4} \text{ m}^2 \text{ s}^{-1}$ is applied. The prognostic volume equation includes surface fluxes from the coupler; thus, virtual salinity fluxes are not needed.

1380 Sea ice in E3SM is represented by the version 3 of the MPAS-SeaIce dynamic-thermodynamic model. MPAS-SeaIce solves the sea-ice momentum equation on the B-grid of the horizontal mesh described above. It uses the CICE Consortium's Icepack sea-ice column physics, including the mushy layer thermodynamics. From v2.1 to v3, the cut-off for dynamical sea ice modeling was reduced from a minimum concentration of 10^{-3} to 10^{-11} , and an ice mass per unit area of 10^{-2} to 10^{-10} . The ocean – sea-ice coupling uses a constant 4 psu salinity, an ice-ocean drag coefficient of 5.36×10^{-3} , and a constant ocean heat transfer coefficient 6×10^{-3} .

1390 The simulation included in this manuscript was run for 5 cycles of the 1958-2020 period. The ocean-sea ice simulation starts from rest, where the ocean hydrography is initialized from the January 1991-2020 climatology of the World Ocean Atlas 2023 (Locarnini et al., 2024; Reagan et al., 2024). The sea-ice state is initialized as a uniform 1-m-thick disk of sea ice for latitudes north of 70°N and south of 60°S , and where ocean sea surface temperature does not exceed the freezing point by 0.2°C .

A7 National Center for Atmospheric Research (NCAR)

1395 NCAR has three contributions: 2 simulations with POP2 and 1 simulation with MOM6. POP2-based simulations use nominal horizontal grid spacings of 1° and 0.1° , which are referred to as NCAR1 and NCAR10, respectively. These configurations employ the ocean and sea-ice components of the Community Earth System Model version 2 (CESM2; Danabasoglu et al., 2020). The MOM6-based configuration represents a new global coupled ocean – sea-ice model configuration with a nominal horizontal grid spacing of $2/3^\circ$ ($\sim 0.67^\circ$), noting that MOM6 is the new ocean component of the upcoming version of CESM, i.e., CESM3. This configuration, 1400 referred to here as NCAR67, is still under rapid development, and the results presented here provide a first assessment of our forced simulations.

POP2 is a level (z) coordinate model with the hydrostatic and Boussinesq approximations (Smith et al., 2010; Danabasoglu et al., 2012a). The version used here includes several physics and numerical advancements as summarized in Danabasoglu et al. (2020). These include improved
1405 treatment of continental freshwater discharge into unresolved estuaries (Sun et al., 2019) and a new parameterization of Langmuir mixing (Li et al., 2016). The sea-ice model is CICE version 5.1.2 (CICE5; Hunke et al., 2015), which features new mushy-layer thermodynamics (Turner and Hunke, 2015) with prognostic sea ice salinity and an updated melt pond parameterization (Hunke et al., 2013). CICE5 runs on the same horizontal grid (B-grid) as the ocean model.

1410 NCAR1 utilizes a dipole grid with the grid north pole displaced into Greenland. The horizontal resolution (nominal 1°) is uniform in the zonal direction at 1.125° but varies in the meridional direction from 0.27° at the Equator to $\sim 0.5^\circ$ at midlatitudes. There are 60 levels in the vertical, varying from 10 m at the surface to 250 m in the deep ocean with a maximum depth of 5500 m. NCAR1 employs the skew-flux form of GM (Griffies, 1998), with depth-dependent GM and
1415 isopycnal diffusivities varying from $3000 \text{ m}^2 \text{ s}^{-1}$ near the surface to $300 \text{ m}^2 \text{ s}^{-1}$ ($600 \text{ m}^2 \text{ s}^{-1}$ for isopycnal) in the deep ocean (Ferreira et al., 2005; Danabasoglu and Marshall, 2007). Near-surface diabatic mesoscale fluxes are parameterized following Ferrari et al. (2008) and Danabasoglu et al. (2008) with a diffusivity of $3000 \text{ m}^2 \text{ s}^{-1}$. Fox-Kemper et al. (2008; 2011) parameterization is used to include the near-surface restratification effects of submesoscale
1420 mixed-layer eddies. The KPP scheme – via the Community ocean Vertical Mixing (CVmix) framework – is employed to prescribe the vertical viscosity and diffusivity coefficients as detailed in Danabasoglu et al. (2012a) with a turbulent Pr of 10. The background values have a latitudinal structure but are constant in the vertical. A tidal mixing parameterization provides enhanced abyssal mixing from tidally generated breaking waves (Jayne, 2009). NCAR1 uses an
1425 overflow parameterization to represent the density-driven flows of the Denmark Strait, Faroe Bank Channel, the Ross Sea, and the Weddell Sea (Danabasoglu et al., 2010). Further details of this configuration can be found in Danabasoglu et al. (2012a; 2014; 2020).

NCAR10 utilizes a tripole grid with the grid north poles located in North America and Asia. It is based on versions documented in Small et al. (2014) but has been updated to the CESM2 code
1430 base. The nominal 0.1° horizontal grid varies from 11 km at the Equator to 2.5 km at high latitudes. The vertical grid is the same as the one used in NCAR1, but it extends deeper to 6000 m with 2 additional levels, i.e., there are 62 vertical levels. NCAR10 uses a partial bottom

cell formulation for more accurate representation of bathymetry, but there is no overflow parameterization. It uses a biharmonic horizontal mixing for tracers and momentum with
1435 respective coefficients of $-3.0 \times 10^9 \text{ m}^4 \text{ s}^{-1}$ and $-2.7 \times 10^{10} \text{ m}^4 \text{ s}^{-1}$. There is no additional parameterization of eddy-induced mixing in this configuration. A modified virtual salt flux formulation that uses a local reference salinity and allows redistribution of continental freshwater fluxes over several vertical layers near the surface is used in NCAR10, but the estuary model employed in NCAR1 to better represent the riverine freshwater flux is not available in NCAR10.
1440 No Langmuir mixing parameterization is used, either. Furthermore, despite using the CICE5 code base, sea-ice physics is based on its previous CICE4 version to maintain consistency with other fully coupled high-resolution simulations that were run with earlier versions of CESM. Additional details of this configuration can be found in Chassignet et al. (2020).

In both NCAR1 and NCAR10, sea surface salinity is restored to World Ocean Atlas 2013
1445 (WOA13; Zweng et al., 2013) monthly climatology with a piston velocity of 50 m over 1 year with subtraction of the global mean restoring. Both configurations use of a half-hour coupling frequency. The initial conditions are derived from the WOA13 (Locarnini et al., 2013; Zweng et al., 2013). NCAR1 and NCAR10 were integrated through 5 and 1 repeat cycles of the 1958-2018, respectively. In each, the last cycle was extended through 2023.

1450 MOM6 (Adcroft et al., 2019) is the new ocean component of the forthcoming CESM3. NCAR67 uses a tripolar grid based on the semi-analytical method of Madec & Imbard (1996). The two northern grid poles are positioned over land in Canada and Russia, resulting in a global orthogonal curvilinear ocean mesh that has no singularity point within the computational domain with an aspect ratio approaching unity throughout the ocean, and it exhibits no loss of continuity
1455 in either the grid lines or the scale factors. Tropical mesh refinement is used, bringing the meridional resolution to 0.25° at the Equator to better capture the equatorial ocean dynamics. The ocean vertical coordinate is hybrid, using z^* near the surface and potential density in deeper layers, with a total of 75 layers. The depth of transition between z^* and isopycnals is the shallowest in the tropics (~ 50 m) and deepens towards high latitudes (~ 1200 and 2000 m in the
1460 Southern and Northern Hemispheres, respectively).

Bottom topography and coastlines are derived from the Global Bathymetry and Topography Dataset (SRTM15+ version 2.4; Tozer et al., 2019), with hand edits to improve the flow in several key regions. The minimum and maximum depths are set to 10 and 6000 m, respectively.

1465 The KPP parameterization for vertical mixing is enabled via the CVMix framework. Following the work described in Large et al. (2021), KPP has been updated to account for 1) a non-local momentum flux in the wind direction when the local shear is not aligned with the wind, and 2) the mixing induced by waves following the Monin-Obukhov similarity theory expanded to include the Stokes drift. Interior mixing components include convection, double-diffusion, and vertical shear of the horizontal velocity. The latitude-dependent diapycnal diffusivity due to
1470 internal wave mixing described in Danabasoglu et al. (2012a) is included with diffusivity values in the range of $1.0 \times 10^{-4} \text{ m}^2 \text{ s}^{-1}$ (in the Banda Sea) to $1.0 \times 10^{-6} \text{ m}^2 \text{ s}^{-1}$ (background) with a turbulent Pr of 10. Energy dissipation from tidally induced breaking internal gravity waves is represented using the scheme developed by Simmons et al. (2004). The restratifying effects of baroclinic eddies in the mixed layer are represented using the parameterization developed by
1475 Bodner et al. (2023).

Mesoscale eddies are parameterized via GM in conjunction with the diffusive mixing of tracers along neutral directions (Redi, 1982). GM is applied using the streamfunction formulation of Ferrari et al. (2010). Mesoscale eddy diffusion is incorporated using the neutral diffusion algorithm described in Shao et al. (2020) below the surface boundary layer, and the horizontal
1480 diffusion algorithm described in Marques et al. (2023) within the surface boundary layer and transition zones. Both the GM and eddy diffusion coefficients are informed via the geometric formalism of Marshall et al. (2012), except that a prognostic eddy kinetic energy (Jansen et al., 2015) is employed, instead of the full (kinetic plus potential) eddy energy. The GM and Redi diffusivities have a minimum value of $50 \text{ m}^2 \text{ s}^{-1}$, typically reach $\sim 1500 \text{ m}^2 \text{ s}^{-1}$ in regions of strong
1485 eddy kinetic energy, and peak at $6500 \text{ m}^2 \text{ s}^{-1}$ in only a few locations. Further details on how mesoscale eddies are represented in this configuration are given in Marques et al. (2023).

The computation of density is corrected to account for the interaction of grid-cell averaging with nonlinearities in the equation of state using the method of Stanley et al. (2020). The stochastic implementation described by Kenigson et al. (2022) is adopted both for hydrostatic pressure and

1490 for the computation of isopycnal slopes in GM, as described by Agarwal et al. (2023). The computation of density is not corrected in any other parts of the model.

The model lateral momentum equations use a biharmonic viscosity. The coefficient of this hyper-viscous closure is modeled using the 2D Leith scheme (Fox-Kemper & Menemenlis, 2008). No backscatter is applied, but the coefficient is smoothed as described by Grooms (2023). The
1495 background biharmonic viscosity is set to $1.0 \times 10^{12} \text{ m}^4 \text{ s}^{-1}$, with increased values in the tropical regions, reaching a maximum of $\sim 3.3 \times 10^{13} \text{ m}^4 \text{ s}^{-1}$. Momentum is extracted via a quadratic drag law with a constant bottom friction coefficient of 3×10^{-3} . The non-linear equation of state for seawater defined by Wright (1997) is applied.

NCAR67 configuration uses the CICE Consortium model version 6.6 (CICE6). This includes
1500 several new physics options as well as a C-grid capability (not turned on currently). Presently, CICE6 needs POP2-style grid and topography files, but work is in progress to read the MOM6 grid and bathymetry files.

The simulation starts from rest with the initial potential temperature and salinity fields from the January-mean climatology of the World Ocean Atlas 2018 (WOA18). The sea surface salinity is
1505 restored to the monthly climatology of the upper 10-m averaged salinity from WOA18 using a piston velocity 50 m over 300 days. The simulation covers one forcing cycle for the 1958-2018 period.

A8 National Oceanography Centre (NOC)

The NOC simulations used a code and configuration denoted as GO8p7 from a late stage of the
1510 development cycle of the Joint Marine Modelling Programme (JMMP) Global Ocean Sea Ice version 9 (GOSI9; Guiavarc'h et al., 2025). The JMMP is a partnership between the UK Met Office and UK research centres: the NOC, the British Antarctic Survey, and the Centre for Polar Observation and Modelling. The 0.25° and $1/12^\circ$ simulations were delivered as part of the UK NERC-funded ACSIS Programme, and the 1° simulation was run later specifically for this study.
1515 These simulations are referred to as NOC25, NOC12, and NOC1, respectively, in this manuscript.

GO8p7 is based on NEMO v4.0.4 (Madec & System Team, 2019) and uses NEMO's new native sea-ice model, SI3. The models use the extended eORCA grids, which have 75 vertical levels

with partial steps, with level thicknesses varying from 1 m at the surface to 200 m in the abyss.
1520 The 1° (eORCA1) bathymetry is derived from the ETOPO2 data set (NOAA, 2006) with the
bathymetry on the Antarctic shelf based on IBSCO (Arndt et al., 2013). At 0.25° (eORCA025),
the bathymetry is derived from the ETOPO1 data set (Amante & Eakins, 2009), with
modifications in coastal regions based on GEBCO (IOC, IHO, & BODC, 2003) and the
bathymetry on the Antarctic shelf derived from IBSCO. Finally, at 1/12° (eORCA12), the
1525 bathymetry is derived from GEBCO_2014 (Weatherall et al., 2015).

GO8p7 uses a vector-invariant momentum advection scheme and a fourth-order TVD tracer
advection and a weak grid-scale-aware GM eddy parameterization, with a coefficient that is
scaled with the ratio of the cell size to the Rossby radius, capped at a maximum value of $70 \text{ m}^2 \text{ s}^{-1}$.
A modified version of the Gaspar et al. (1990) TKE scheme (Madec et al., 2019) is used for
1530 vertical mixing, and the parameterization of Simmons et al. (2004) for tidal mixing is applied.
We use adaptive-implicit vertical advection (Shchepetkin, 2015). Lateral mixing of tracers is
along neutral surfaces using the scheme of Redi (1982) and Cox (1987) with a coefficient equal
to the cell size multiplied by 0.011 m s^{-1} . At 1°, the viscosity is Laplacian with a lateral viscosity
coefficient of $20\,000 \text{ m}^2 \text{ s}^{-1}$, while at 0.25° and 1/12°, a bi-Laplacian viscosity is used, with the
1535 coefficient set at the Equator to -1.5×10^{11} and $-1.25 \times 10^{11} \text{ m}^4 \text{ s}^{-1}$, respectively, and reduces
with the inverse cube of the cell size. The equation of state is TEOS-10 (IOC et al., 2010).

Between GO8p7 and the official release GOSI9, some additional tuning of parameters took place
to reduce some of the larger biases. These include: a reduction of the TKE mixing depth and an
increase in the globally uniform chlorophyll concentration to improve mixed layer depth and
1540 reduce a subsurface warm bias in the 100-200 m depth range; and increases in snow
conductivity, lateral melt, heat in ice leads, and albedo parameters to improve the ice
representation.

In all cases, the model started from rest using January-mean for the 1995-2014 period from EN4
(Good et al., 2013) climatological conditions and completed one pass through the JRA55-do
1545 forcing dataset (Tsuji no et al., 2018). A sea surface salinity (SSS) restoring towards monthly
mean climatology is applied with a piston velocity of 50 m over 1500 days.

A9 UK Met Office (UKMO)

The UKMO 0.25° model simulation differs from the NOC simulations described in Appendix A8
1550 in the following four aspects. First, it uses a hybrid quasi-Eulerian vertical coordinate system
where model levels are “nearly” terrain-following in the proximity of the Greenland-Scotland
ridge area while they follow z^* -coordinates with partial steps in the rest of the domain
(Bruciaferri et al., 2018; 2024). Second, it adopts a “log-layer” formulation for the bottom drag
coefficient C_D . In NEMO, for stability reasons, the minimum and maximum values of C_D are
1555 capped. With z -coordinates, the bottom topography is represented as a series of step-like
structures, resulting in friction being exerted both at the bottom and at the lateral wall-sides via a
no-slip boundary condition. Conversely, with terrain-following levels the representation of the
bathymetry is more realistic, making the usage of lateral boundary conditions unnecessary. For
this reason, in the area where model levels are terrain-following, the simulation uses a more
1560 realistic C_D minimum value of 3×10^{-3} (see, e.g., observational estimates by Girton & Sanford
2003, Mauritzen et al. (2005), or numerical studies by Riemenschneider & Legg (2007) and
Danabasoglu et al. (2010)), while in the rest of the domain it is set to 10^{-3} , the same value of
NOC25 simulation. Third, it employs the Griffies et al. (1998) triad formulation for the iso-
neutral diffusion because it is the only available option for using iso-neutral mixing with hybrid
1565 vertical coordinates in the current release of NEMO (see Appendix D of Bruciaferri et al. (2024)
for a comparison between this formulation and the one used in the standard GOSI9). Finally, it
uses the Density Jacobian with Cubic (DJC) polynomial scheme of Shchepetkin & McWilliams
(2003) as implemented in NEMO by Bell & Bruciaferri (2022) for a more accurate calculation of
horizontal pressure forces when using steeply inclined vertical levels. This simulation is referred
1570 to as UKMO25 in the manuscript.

Code Availability. The METRIC Package is available at <https://doi.org/10.5281/zenodo.4708276>.
A copy of the Gibbs-SeaWater (GSW) Oceanographic Toolbox containing the TEOS-10
Equation of State is available at <https://doi.org/10.5281/zenodo.19955068>. For more information
on TEOS-10, we refer the reader to <https://www.teos-10.org/>, the official TEOS-10 site and the
1575 only vetted source of information about the TEOS-10, including the details of how it should be
used.

Data Availability. The simulation datasets for our analysis region are available at <https://doi.org/10.5281/zenodo.17457323> (Castruccio and Danabasoglu, 2025). For some of the simulations, entire global datasets for the full integration lengths are available as follows.

1580 ACCESS-OM2 (ANU1), ACCESS-OM2-025 (ANU25), and GFDL25 data were contributed to CMIP6 and are available on the Earth System Grid Federation (ESGF) at <https://aims2.llnl.gov/search/cmip6/>. ACCESS-OM2-01 (ANU10) data are available via the NCI Data Catalogue at <https://dx.doi.org/10.25914/608097cb3433f>. Output from the NOC25 and NOC08 simulations are available from CEDA at <https://data.ceda.ac.uk/bodc/SOC220065>. The
1585 OSNAP observations are available at Georgia Tech Digital Repository at <https://doi.org/10.35090/gatech/78023>.

Author contributions. GD and FC conceived and proposed the idea for this study. GD led writing of the manuscript. FC led the analysis of all model simulations. BB helped with the analysis. YF and MSL provided observational contributions. The following authors provided the datasets from
1590 the respective simulations along with their brief model descriptions, listed here based on their center names: AH, RMH, HH, and AEK for ANU; DI for CMCC; ABo, EPC, and XX for FSU; ABi and FUS for GEOMAR; RZ for GFDL; AMB, LvR, and JW for LANL; GD, FC, FB, IG, and GM for NCAR; ABi and AM for NOC; and DB, CG, and DS for UKMO. All authors contributed to writing and editing of the manuscript.

1595 *Competing interests.* The authors declare that they have no conflict of interest.

Acknowledgements. This effort at the US National Science Foundation (NSF) National Center for Atmospheric Research (NCAR) was supported by the contract 1947282 from the US Department of Energy (DOE) for the ImPACTS Project; by the grant NA18OAR4310429 from the US National Oceanic and Atmospheric Administration (NOAA), Climate Program Office (CPO),
1600 Climate Variability and Predictability Program; Modeling Analysis, Predictions, and Projections Program; the NOAA Global Ocean Monitoring and Observing (GOMO) Program; the DOE, Earth and Environmental System Modeling, Regional and Global Model Analysis Program; and by the grant OPP-2106228 from the US NSF Office of Polar Programs. The US NSF NCAR is a major facility sponsored by the US NSF under Cooperative Agreement No. 1852977. The project
1605 was also partly funded by the US NSF – UK Natural Environment Research Council (NERC)

project entitled “Wider Impacts of Subpolar North Atlantic Decadal Variability on the Ocean and Atmosphere (WISHBONE)”. OSNAP data were collected and made freely available by the Overturning in the Subpolar North Atlantic Program and all the national programs that contribute to it (www.o-snap.org). The authors extend gratitude to everyone involved in the OSNAP

1610 program, including those who spend many hours at sea collecting data. Dr. Alistair Adcroft and Raphael Dussin are thanked for conducting the GFDL OM4 OMIP-2 simulation. Dr. Alistair Adcroft is also thanked for his review of the manuscript. Bill Hurlin is thanked for publishing the GFDL OM4 OMIP-2 data. We acknowledge the contributions of Filipe Pereira, who passed away before completion of this manuscript. AEK was supported by the Australian Research Council

1615 (ARC) grant LP200100406. RMH was supported by the ARC grant DE21010004. AM was supported by the UK Natural Environment Research Council under the Atlantic Climate System Integrated Study (ACSIS; grant number NE/N018044/1) and the Climate Linked Atlantic Sector Science (CLASS; grant number NE/R015953/1) marine research programmes. ABI was supported by CLASS (NE/R015953/1) and the WISHBONE project (NE/T013540/1). BB was

1620 partly supported by the Turkish Scientific and Technological Research Council (TUBITAK) via an International Research Fellowship Programme for PhD Students (2214-A). MSL and YF acknowledge funding from the Physical Oceanography Program of the US NSF (OCE-1948335). The ACCESS-OM2 model runs were undertaken by the Consortium for Ocean-Sea Ice Modelling in Australia (COSIMA) (<http://www.cosima.org.au>) using computational resources

1625 provided by the Australian Government through the National Computational Infrastructure (NCI) under the National Computational Merit Allocation Scheme and ANU Merit Allocation Scheme. The GEOMAR simulations were funded by the Earth System Modelling Project (ESM) by providing computing time on the ESM partition of the supercomputer JUWELS at Jülich Supercomputing Center (JSC). The MPAS-O simulations were produced as part of the DOE

1630 Energy Exascale Earth System Model (E3SM) project funded by the DOE Earth System Model Development program area of the Earth and Environmental System Modeling program, using a high-performance computing cluster operated by the Laboratory Computing Resource Center at the Argonne National Laboratory. This effort benefited greatly from the discussions that occurred during the joint WISHBONE and SNAP-DRAGON (Subpolar North Atlantic Processes –

1635 Dynamics and Predictability of Variability in Gyre and Overturning) project meetings. Finally,

we thank our reviewers, Dr. Dmitry Sidorenko, Dr. Chuncheng Guo, and an anonymous reviewer, for their constructive comments and suggestions.

References

- 1640 Adcroft, A. and Campin, J.-M.: Rescaled height coordinates for accurate representation of free-surface flows in ocean circulation models, *Ocean Model.*, 7, 269–284, <https://doi.org/10.1016/j.ocemod.2003.09.003>, 2004.
- Adcroft, A., Hill, C., and Marshall, J.: Representation of topography by shaved cells in a height coordinate ocean model, *Mon. Wea. Rev.*, 125, 2293–2315, [https://doi.org/10.1175/1520-0493\(1997\)125<2293:ROTBSC>2.0.CO;2](https://doi.org/10.1175/1520-0493(1997)125<2293:ROTBSC>2.0.CO;2), 1997.
- 1645 Adcroft, A., Anderson, W., Balaji, V., Blanton, C., Bushuk, M., Dufour, C. O., Dunne, J. P., Griffies, S. M., Hallberg, R., Harrison, M. J., Held, I. M., Jansen, M. F., John, J. G., Krasting, J. P., Langenhorst, A. R., Legg, S., Liang, Z., McHugh, C., Radhakrishnan, A., Reichl, B. G., Rosati, T., Samuels, B. L., Shao, A., Stouffer, R., Winton, M., Wittenberg, A. T., Xiang, B., Zadeh, N., and Zhang, R.: The GFDL global ocean and sea ice model OM4.0: Model
1650 description and simulation features, *J. Adv. Model. Earth Sy.*, 11(10), 3167–3211, <https://doi.org/10.1029/2019MS001726>, 2019.
- Agarwal, N., Small, R. J., Bryan, F. O., Grooms, I., and Pegion, P.J.: Impact of stochastic ocean density corrections on air-sea flux variability, *Geophys. Res. Lett.*, 50, e2023GL104248, 2023.
- 1655 Amante, C. and Eakins, B. W.: ETOPO1 1 Arc-Minute Global Relief Model: Procedures, Data Sources and Analysis, NOAA Technical Memorandum NESDIS NGDC-24, 19 pp., 2009.
- Arakawa, A. and Hsu, Y.-J. G.: Energy conserving and potential-entropy dissipating schemes for the shallow water equations, *Mon. Wea. Rev.*, 118, 1960–1969, [https://doi.org/10.1175/1520-0493\(1990\)118<1960:ECAPED>2.0.CO;2](https://doi.org/10.1175/1520-0493(1990)118<1960:ECAPED>2.0.CO;2), 1990.
- 1660 Arndt, J. E., Schenke, H. W., Jakobsson, M., Nitsche, F. O., Buys, G., Goleby, B., Rebesco, M., Bohoyo, F., Hong, J., Black, J., Greku, R., Udintsev, G., Barrios, F., Reynoso-Peralta, W., Taisei, M., and Wigley, R.: The International Bathymetric Chart of the Southern Ocean (IBCSO) Version 1.0 – A new bathymetric compilation covering circum-Antarctic waters, *Geophys. Res. Lett.*, 40, 3111–3117, <https://doi.org/10.1002/grl.50413>, 2013.
- 1665 Ballarotta, M., Drijfhout, S., Kuhlbrodt, T., and Doos, K.: The residual circulation of the Southern Ocean: Which spatio-temporal scales are needed? *Ocean Model.*, 64, 46–55, <https://dx.doi.org/10.1016/j.ocemod.2013.01.005>, 2013.
- Bamber, J. L., Tedstone, A. J., King, M. D., Howat, I. M., Enderlin, E. M., van den Broeke, M. R., and Noel, B.: Land ice freshwater budget of the Arctic and North Atlantic Oceans: 1.
1670 Data, methods and results, *J. Geophys. Res.*, 123, 1827–1837, <https://doi.org/10.1002/2017JC013605>, 2018.
- Barnier, B., Madec, G., Penduff, T., Molines, J., Treguir, A.-M., Le Sommer, J., Beckmann, A., Biastoch, A., Böning, C., Dengg, J., Derval, C., Durand, E., Gulev, S., Remy, E., Talandier, C., Theetten, S., Maltrud, M., McClean, J., and de Cuevas, B.: Impact of partial steps and
1675 momentum advection schemes in a global ocean circulation model at eddy permitting resolution, *Ocean Dynam.*, 56, 543–567, <https://doi.org/10.1007/s10236-006-0082-1>, 2006.

- Beckmann, A. and Doscher, R.: A method for improved representation of dense water spreading over topography in geopotential-coordinate models, *J. Phys. Oceanogr.*, 27, 581–591, [http://dx.doi.org/10.1175/1520-0485\(1997\)027<0581:AMFIRO>2.0.CO;2](http://dx.doi.org/10.1175/1520-0485(1997)027<0581:AMFIRO>2.0.CO;2), 1997.
- 1680 Bell, M. J. and Bruciaferri, D.: Accurate calculation of pressure forces on cells defined by steeply sloping coordinates, EGU General Assembly 2022, Vienna, Austria, 23–27 May 2022, EGU22-5012, <https://doi.org/10.5194/egusphere-egu22-5012>, 2022.
- Bi, D., Marsland, S., Uotila, P., O’Farrell, S., Fiedler, R., Sullivan, A., Griffies, S., Zhou, X., and Hirst, A.: ACCESS-OM: the ocean and sea-ice core of the ACCESS coupled model, Australian Meteorological and Oceanographic Journal, 63, 213–232, <http://www.bom.gov.au/jshess/papers.php?year=2013>, 2013.
- 1685 Bi, D., Dix, M., Marsland, S., O’Farrell, S., Sullivan, A., Bodman, R., Law, R., Harman, I., Srbinovsky, J., Rashid, H. A., Dobrohotoff, P., Mackallah, C., Yan, H., Hirst, A., Savita, A., Dias, F. B., Woodhouse, M., Fiedler, R., and Heerdegen, A.: Configuration and spin-up of ACCESS-CM2, the new generation Australian Community Climate and Earth System Simulator Coupled Model, *J. Southern Hemisphere Earth Sy. Sci.*, 70, 225–251, <https://doi.org/10.1071%2Fes19040>, 2020.
- 1690 Biastoch, A., Schwarzkopf, F. U., Getzlaff, K., Ruhs, S., Martin, T., Scheinert, M., Schulzki, T., Handmann, P., Hummels, R., and Böning, C.: Regional imprints of changes in the Atlantic meridional overturning circulation in the eddy-rich ocean model VIKING20X, *Ocean Sci.*, 17, 1177–1211, <https://doi.org/10.5194/os-17-1177-2021>, 2021.
- 1695 Bitz, C. M. and Lipscomb, W. H.: An energy-conserving thermodynamic model of sea ice, *J. Geophys. Res.*, 104, 15669–15677, 1999.
- Bitz, C. M., Holland, M., Eby, M., and Weaver, A. J.: Simulating the ice-thickness distribution in a coupled climate model, *J. Geophys. Res. Oceans*, 106, 2441–2463, <https://doi.org/10.1029/1999JC000113>, 2001.
- 1700 Blanke, B. and Delecluse, P.: Variability of the tropical Atlantic Ocean simulated by a general circulation model with two different mixed layer physics, *J. Phys. Oceanogr.*, 23, 1363–1388, 1993.
- 1705 Bleck, R.: An oceanic general circulation model framed in hybrid isopycnic-Cartesian coordinates, *Ocean Model.*, 4, 55–88, [https://doi.org/10.1016/S1463-5003\(01\)00012-9](https://doi.org/10.1016/S1463-5003(01)00012-9), 2002.
- Bodner, A. S., Fox-Kemper, B., Johnson, L., Van Roekel, L. P., McWilliams, J. C., Sullivan, P. P., Hall, P. S., and Dong, J.: Modifying the mixed layer eddy parameterization to include frontogenesis arrest by boundary layer turbulence, *J. Phys. Oceanogr.*, 53, 323–339, <https://doi.org/10.1175/JPO-D-21-0297.1>, 2023.
- 1710 Bouillon, S., Fichefet, T., Legat, V., and Madec, G.: The elastic–viscous–plastic method revisited, *Ocean Model.*, 71, 2–12, <https://doi.org/10.1016/j.ocemod.2013.05.013>, 2013.
- Boyer, T., Locarnini, R. A., Zweng, M. M., Mishonov, A. V., Reagan, J. R., Antonov, J. I., Garcia, H. E., Baranova, O. K., Johnson, D. R., Seidov, D., Biddle, M. M., and Hamilton, M.: Changes to calculations of the World Ocean Atlas 2013 for version 2. Technical Report. NOAA, https://data.nodc.noaa.gov/woa/WOA13/DOC/woa13v2_changes, 2015.
- 1715 Böning, C. W., Wagner, P., Handmann, P., Schwarzkopf, F. U., Getzlaff, K., and Biastoch, A.: Decadal changes in Atlantic overturning due to the excessive 1990s Labrador Sea convection, *Nat. Comm.*, 14, 1–10, <https://doi.org/10.1038/s41467-023-40323-9>, 2023.

- 1720 Bruciaferri, D., Shapiro, G. I., and Wobus, F.: A multi-envelope vertical coordinate system for numerical ocean modelling, *Ocean Dynamics*, 68, 1239–1258, <https://doi.org/10.1007/s10236-018-1189-x>, 2018.
- Bruciaferri, D., Guiavarc’h, C., Hewitt, H. T., Harle, J., Almansi, M., Mathiot, P., and Colombo, P.: Localized general vertical coordinates for quasi-Eulerian ocean models: The Nordic overflows test-case. *J. Adv. Model. Earth Sy.*, 16, e2023MS003893, <https://doi.org/10.1029/2023MS003893>, 2024.
- 1725 Bryden, H. L., Longworth, H. R., and Cunningham, S. A.: Slowing of the Atlantic meridional overturning circulation at 25°N, *Nature*, 438, 655–657, <https://doi.org/10.1038/nature04385>, 2005.
- 1730 Bryden, H., Beunk, J., Drijfhout, S., Hazeleger, W., and Mecking, J.: Comparing observed and modelled components of the Atlantic Meridional Overturning Circulation at 26° N, *Ocean Sci.*, 20, 589–599, <https://doi.org/10.5194/os-20-589-2024>, 2024.
- Buckley, M. W. and Marshall, J.: Observations, inferences, and mechanisms of Atlantic meridional overturning circulation variability: A review, *Rev. Geophys.*, 54, 5–63, <https://doi.org/10.1002/2015RG000493>, 2016.
- 1735 Buckley, M. W., Lozier, M. S., Desbruyeres, D., and Evans, D. G.: Buoyancy forcing and the subpolar Atlantic meridional overturning circulation, *Philos. Trans. R. Soc, A.*, 381, 20220181, <https://doi.org/10.1098/rsta.2022.0181>, 2023.
- Caesar, L., Rahmstorf, S., Robinson, A., Feulner, G., and Saba, V.: Observed fingerprint of a weakening Atlantic Ocean overturning circulation, *Nature*, 556, 191–196, <https://doi.org/10.1038/s41586-018-0006-5>, 2018.
- 1740 Caesar, L., McCarthy, G. D., Thornalley, D. J. R., Cahill, N., and Rahmstorf, S.: Current Atlantic meridional overturning circulation weakest in last millennium, *Nature Geoscience*, 14, 118–120, <https://doi.org/10.1038/s41561-021-00699-z>, 2021.
- 1745 Campin, J.-M. and Goosse, H.: Parameterization of density-driven downsloping flow for a coarse-resolution ocean model in z-coordinate, *Tellus A: Dynam. Meteor. Oceanogr.*, 51, 412–430, <http://dx.doi.org/10.3402/tellusa.v51i3.13468>, 1999.
- Carnes, M. R.: Description and evaluation of GDEM-V3.0. Report number: NRL/MR/7330-09-9165, United States: Naval Research Laboratory, 2009.
- 1750 Castruccio, F. S.: NCAR/metric: metric v0.1. doi/10.5281/zenodo.4708277, 2021.
- Castruccio, F. and Danabasoglu, G.: Datasets to reproduce the figures in “Simulated and observed transport estimates across the Overturning in the Subpolar North Atlantic Program (OSNAP) section”, available at <https://doi.org/10.5281/zenodo.17457323>, 2025.
- 1755 Chafik, L., Holliday, N. P., Bacon, S., and Rossby, T.: Irminger Sea is the center of action for subpolar AMOC variability, *Geophys. Res. Lett.*, 49, e2022GL099133, <https://doi.org/10.1029/2022GL099133>, 2022.
- Chassignet, E. P., Smith, L. T., Halliwell, G. R., and Bleck, R.: North Atlantic simulations with the Hybrid Coordinate Ocean Model (HYCOM): Impact of the vertical coordinate choice, reference pressure, and thermobaricity, *J. Phys. Oceanogr.*, 33, 2504–2526, [https://doi.org/10.1175/1520-0485\(2003\)0332.0.CO;2](https://doi.org/10.1175/1520-0485(2003)0332.0.CO;2), 2003.
- 1760 Chassignet, E. P., Yeager, S. G., Fox-Kemper, B., Bozec, A., Castruccio, F., Danabasoglu, G., Kim, W. M., Koldunov, N., Li, Y., Lin, P., Liu, H., Sein, D., Sidorenko, D., Wang, Q., and

- 1765 Xu, X.: Impact of horizontal resolution on global ocean-sea-ice model simulations based on the experimental protocols of the Ocean Model Intercomparison Project phase 2 (OMIP-2), *Geosci. Model Dev.*, 13, 4595–4637, <https://doi.org/10.5194/gmd-13-4595-2020>, 2020.
- Cheng, W., Chiang, J. C. H., and Zhang, D.: Atlantic meridional overturning circulation (AMOC) in CMIP5 models: RCP and historical simulations, *J. Climate*, 26, 7187–7197, <https://doi.org/10.1175/JCLI-D-12-00496.1>, 2013.
- 1770 Cherchi, A., Fogli, P. G., Lovato, T., Peano, D., Iovino, D., Gualdi, S., Masina, S., Scoccimarro, E., Materia, S., Bellucci, A., and Navarra, A.: Global mean climate and main patterns of variability in the CMCC-CM2 coupled model, *J. Adv. Model. Earth Sy.*, 11, 185–209, <https://doi.org/10.1029/2018MS001369>, 2019.
- 1775 Cipollone, A., Storto, A., and Masina, S.: Implementing a parallel version of a variational scheme in a global assimilation system at eddy-resolving resolution, *J. Atmos. Ocean. Tech.*, 37, 1865–1876, 2020.
- Cox, M. D.: Isopycnal diffusion in a z-coordinate ocean model, *Ocean Modelling*, 74, 1–9, 1987.
- Cunningham, S. A., Kanzow, T., Rayner, D., Baringer, M. O., Johns, W. E., Marotzke, J., Longworth, H. R., Grant, E. M., Hirschi, J. J.-M., Beal, L. M., Meinen, C. S., and Bryden, H. L.: Temporal variability of the Atlantic meridional overturning circulation at 26.5°N, *Science*, 317, 935–938, <https://doi.org/10.1126/science.1141304>, 2007.
- 1780 Danabasoglu, G.: On multi-decadal variability of the Atlantic meridional overturning circulation in the Community Climate System Model version 3 (CCSM3), *J. Climate*, 21, 5524–5544, <https://doi.org/10.1175/2008JCLI2019.1>, 2008.
- 1785 Danabasoglu, G. and Marshall, J.: Effects of vertical variations of thickness diffusivity in an ocean general circulation model, *Ocean Model.*, 18, 122–141, <https://doi.org/10.1016/j.ocemod.2007.03.006>, 2007.
- Danabasoglu, G., Ferrari, R., and McWilliams, J. C.: Sensitivity of an ocean general circulation model to a parameterization of near-surface eddy fluxes, *J. Climate*, 21, 1192–1208, <https://doi.org/10.1175/2007JCLI1508.1>, 2008.
- 1790 Danabasoglu, G., Large, W. G., and Briegleb B. P.: Climate impacts of parameterized Nordic Sea overflows, *J. Geophys. Res.*, 115, C11005, <http://doi.org/10.1029/2010JC006243>, 2010.
- Danabasoglu, G., Bates, S. C., Briegleb, B. P., Jayne, S. R., Jochum, M., Large, W. G., Peacock, S., and Yeager, S. G.: The CCSM4 ocean component, *J. Climate*, 25, 1361–1389, <https://doi.org/10.1175/JCLI-D-11-00091.1>, 2012a.
- 1795 Danabasoglu, G., Yeager, S. G., Kwon, Y.-O., Tribbia, J. J., Phillips, A. S., and Hurrell, J. W.: Variability of the Atlantic meridional overturning circulation in CCSM4, *J. Climate*, 25, 5153–5172, <https://doi.org/10.1175/JCLI-D-11-00463.1>, 2012b.
- 1800 Danabasoglu, G., Yeager, S. G., Bailey, D., Behrens, E., Bentsen, M., Bi, D., Biastoch, A., Böning, C., Bozec, A., Canuto, V. M., Cassou, C., Chassignet, E., Coward, A. C., Danilov, S., Diansky, N., Drange, H., Farneti, R., Fernandez, E., Fogli, P. G., Forget, G., Fujii, Y., Griffies, S. M., Gusev, A., Heimbach, P., Howard, A., Jung, T., Kelley, M., Large, W. G., Leboissetier, A., Lu, J., Madec, G., Marsland, S. J., Masina, S., Navarra, A., Nurser, A. J. G., Pirani, A., Salas y Mélia, D., Samuels, B. L., Scheinert, M., Sidorenko, D., Treguier, A.-M., Tsujino, H., Uotila, P., Valcke, S., Voldoire, A., and Wang, Q.: North Atlantic simulations in Coordinated Ocean-ice Reference Experiments phase II (CORE-II). Part I: Mean states,
- 1805 *Ocean Model.* 73, 76–107. <https://doi.org/10.1016/j.ocemod.2013.10.005>, 2014.

- 1810 Danabasoglu, G., Yeager, S. G., Kim, W. M., Behrens, E., Bentsen, M., Bi, D., Biastoch, A., Bleck, R., Böning, C., Bozec, A., Canuto, V. M., Cassou, C., Chassignet, E., Coward, A. C., Danilov, S., Diansky, N., Drange, H., Farneti, R., Fernandez, E., Fogli, P. G., Forget, G., Fujii, Y., Griffies, S. M., Gusev, A., Heimbach, P., Howard, A., Ilicak, M., Jung, T., Karspeck, A., R., Kelley, M., Large, W. G., Leboissetier, A., Lu, J., Madec, M., Marsland, S. J., Masina, S., Navarra, A., Nurser, A. J. G., Pirani, A., Romanou, A., Salas y Melia, D., Samuels, B. L., Scheinert, M., Sidorenko, D., Sun, S., Treguier, A.-M., Tsujino, H., Uotila, P., Valcke, S., Voltaire, A., Wang, Q., and Yashayaev, I.: North Atlantic simulations in Coordinated Ocean-ice Reference Experiments phase II (CORE-II). Part II: Inter-annual to decadal variability, *Ocean Model.*, 97, 65–90, <https://doi.org/10.1016/j.ocemod.2015.11.007>, 2016.
- 1815 Danabasoglu, G., Landrum, L., Yeager, S. G., and Gent, P. R.: Robust and non-robust aspects of Atlantic meridional overturning circulation variability and mechanisms in the Community Earth System Model, *J. Climate*, 32, 7349–7369, <https://doi.org/10.1175/JCLI-D-19-0026.1>, 2019.
- 1820 Danabasoglu, G., Lamarque, J.-F., Bacmeister, J., Bailey, D. A., DuVivier, A. K., Edwards, J., Emmons, L. K., Fasullo, J., Garcia, R., Gettelman, A., Hannay, C., Holland, M. M., Large, W. G., Lauritzen, P. H., Lawrence, D. M., Lenaerts, J. T. M., Lindsay, K., Lipscomb, W. H., Mills, M. J., Neale, R., Oleson, K. W., Otto-Bliesner, B., Phillips, A. S., Sacks, W., Tilmes, S., van Kampenhout, L., Vertenstein, M., Bertini, A., Dennis, J., Deser, C., Fischer, C., Fox-Kemper, B., Kay, J. E., Kinnison, D., Kushner, P. J., Larson, V. E., Long, M. C., Mickelson, S., Moore, J. K., Nienhouse, E., Polvani, L., Rasch, P. J., and Strand, W. G.: Community Earth System Model version 2 (CESM2). *J. Adv. Model. Earth Sys.*, 12, e2019MS001916, <https://doi.org/10.1029/2019MS001916>, 2020.
- 1825 Debreu, L., Vouland, C., and Blayo, E.: AGRIF: Adaptive grid refinement in Fortran. *Comput. Geosci.*, 34, 8–13, 2008.
- 1830 Depoorter, M. A., Bamber, J. L., Griggs, J. A., Lenaerts, J. T. M., Ligtenberg, S. R. M., van den Broeke, M. R., and Moholdt, G.: Calving fluxes and basal melt rates of Antarctic ice shelves, *Nature*, 502, 89–92, <https://doi.org/10.1038/nature12567>, 2013.
- 1835 Doscher, R. and Beckmann, A.: Effects of a bottom boundary layer parameterization in a coarse-resolution model of the North Atlantic Ocean, *J. Atmos. Oceanic Tech.*, 17, 698–707, [http://dx.doi.org/10.1175/1520-0426\(2000\)017<0698:EOABBL>2.0.CO;2](http://dx.doi.org/10.1175/1520-0426(2000)017<0698:EOABBL>2.0.CO;2), 2000.
- 1840 Ferrari, R., McWilliams, J. C., Canuto, V. M., and Dubovikov, M.: Parameterization of eddy fluxes near oceanic boundaries, *J. Climate*, 21, 2770–2789, <https://doi.org/10.1175/2007JCLI1510.1>, 2008.
- Ferrari, R., Griffies, S. M., Nurser, A. G., and Vallis, G. K.: A boundary-value problem for the parameterized mesoscale eddy transport, *Ocean Modelling*, 32, 143–156, <https://doi.org/10.1016/j.ocemod.2010.01.004>, 2010.
- 1845 Ferreira, D., Marshall, J., and Heimbach, P.: Estimating eddy stresses by fitting dynamics to observations using a residual-mean ocean circulation model and its adjoint, *J. Phys. Oceanogr.*, 35, 1891–1910, <https://doi.org/10.1175/JPO2785.1>, 2005.
- Fichefet, T. and Morales Maqueda, M. A.: Sensitivity of a global sea ice model to the treatment of ice thermodynamic and dynamics, *J. Geophys. Res.*, 102, 12609–12646, 1997.

- 1850 Fofonoff, N. P. and Millard Jr., R. C.: Algorithms for the computation of fundamental properties of seawater, Paris, France, UNESCO, UNESCO Technical Papers in Marine Sciences, 44, 53 pp., <https://doi.org/10.25607/OBP-1450>, 1983.
- Fogli, P. G. and Iovino, D.: CMCC–CESM–NEMO: Toward the new CMCC Earth System Model, CMCC Research Paper no. 248, <https://doi.org/10.2139/ssrn.2603176>, 2014.
- 1855 Fox-Kemper, B. and Menemenlis, D.: Can large eddy simulation techniques improve mesoscale rich ocean models? *Geophys. Monograph Series*, 177, 319–337, 2008.
- Fox-Kemper, B., Ferrari, R., and Hallberg, R.: Parameterization of mixed layer eddies. Part I: Theory and diagnosis, *J. Phys. Oceanogr.*, 38, 1145–1165, <http://dx.doi.org/10.1175%2F2007JPO3792.1>, 2008.
- 1860 Fox-Kemper, B., Danabasoglu, G., Ferrari, R., Griffies, S. M., Hallberg, R. W., Holland, M. M., Maltrud, M. E., Peacock, S., and Samuels, B. L.: Parameterization of mixed layer eddies. III: Implementation and impact in global ocean climate simulations, *Ocean Model.*, 39, 61–78, <https://doi.org/10.1016/j.ocemod.2010.09.002>, 2011.
- 1865 Fox, A. D., Handmann, P., Schmidt, C., Fraser, N., Ruhs, S., Sanchez-Franks, A., Martin, T., Oltmanns, M., Johnson, C., Rath, W., Holliday, N. P., Biastoch, A., Cunningham, S. A., and Yashayaev, I.: Exceptional freshening and cooling in the eastern subpolar North Atlantic caused by reduced Labrador Sea surface heat loss, *Ocean Sci.*, 18, 1507–1533, <https://doi.org/10.5194/OS-18-1507-2022>, 2022.
- 1870 Fröhle, J., Handmann, P. V. K., and Biastoch, A.: Major sources of North Atlantic Deep Water in the subpolar North Atlantic from Lagrangian analyses in an eddy-rich ocean model, *Ocean Sci.*, 18, 1431–1450, <https://doi.org/10.5194/OS-18-1431-2022>, 2022.
- 1875 Fu, Y., Lozier, M. S., Biló, T. C., Bower, A. S., Cunningham, S. A., Cyr, F., de Jong, M. F., deYoung, B., Drysdale, L., Fraser, N., Fried, N., Furey, H. H., Han, G., Handmann, P., Holliday, N. P., Holte, J., Inall, M. E., Johns, W. E., Jones, S., Karstensen, J., Li, F., Pacini, A., Pickart, R. S., Rayner, D., Straneo, F., and Yashayaev, I.: Seasonality of the meridional overturning circulation in the subpolar North Atlantic, *Comm. Earth & Environment*, 4, 181., <https://doi.org/10.1038/s43247-023-00848-9>, 2023.
- Fu, Y., Lozier, M. S., Majumder, S., and Petit, T.: Water mass transformation and its relationship with the overturning circulation in the eastern subpolar North Atlantic, *J. Geophys. Res.: Oceans*, 129, <https://doi.org/10.1029/2024JC021222>, 2024.
- 1880 Fu, Y., Lozier, M. S., Bower, A. S., Burmeister, K., Bilo, T. C., Cyr, F., Cunningham, S. A., DeYoung, B., Dilmahamod, A. F., de Jong, M. F., Fried, N., Holliday, N. P., Fraser, N. J., Johns, W. E., Li, F., Karstensen, J., Pickart, R. S., Straneo, F., and Yashayaev, I.: Characterizing the interannual variability of North Atlantic subpolar overturning, *Geophys. Res. Lett.*, 52, e2025GL114672, <https://doi.org/10.1029/2025GL114672>, 2025.
- 1885 Gaspar, P., Grégoris, Y., and Lefevre, J.-M.: A simple eddy kinetic energy model for simulations of the oceanic vertical mixing: Tests at station Papa and long-term upper ocean study site, *J. Geophys. Res.*, 95, 16179–16193, <https://doi.org/10.1029/jc095ic09p16179>, 1990.
- GEBCO Compilation Group: GEBCO 2023 Grid, doi:10.5285/f98b053b-0cbc-6c23-e053-6c86abc0af7b, 2023.
- 1890 Gent, P. R. and McWilliams, J. C.: Isopycnal mixing in ocean circulation models, *J. Phys. Oceanogr.*, 20, 150–155, [https://doi.org/10.1175/15200485\(1990\)020<0150:imiocm>2.0.co;2](https://doi.org/10.1175/15200485(1990)020<0150:imiocm>2.0.co;2), 1990.

- 1895 Girton, J. B. and Sanford, T. B.: Descent and modification of the overflow plume in the Denmark Strait, *J. Phys. Oceanogr.*, 33, 1351–1363, [https://doi.org/10.1175/1520-0485\(2003\)033<1351:DAMOTO>2.0.CO;2](https://doi.org/10.1175/1520-0485(2003)033<1351:DAMOTO>2.0.CO;2), 2003.
- 1900 Golaz, J. C., Van Roekel, L. P., Zheng, X., Roberts, A. F., Wolfe, J. D., Lin, W., Bradley, A. M., Tang, Q., Maltrud, M. E., Forsyth, R. M., Zhang, C., Zhou, T., Zhang, K., Zender, C. S., Wu, M., Wang, H., Turner, A., K., Singh, B., Richter, J. H., Qin Y., Petersen, M. R., Mametjanov, A., Ma, P. L., Larson, V. E., Krishna, J., Keen, N. D., Jeffery, N., Hunke, E. C., Hannah, W. M., Guba, O., Griffin, B. M., Feng, Y., Engwirda, D., Di Vittorio, A. V., Dang, C., Conlon, L. A. M., Chen, C. C. J., Brunke, M. A., Bisht, G., Benedict, J. J., Asay-Davis, X. S., Zhang, Y., Zhang, M., Zeng, X., Xie, S., Wolfram, P. J., Vo, T., Veneziani, M., Tesfa, T. K., Sreepathi, S., Salinger, A. G., Eyre, J. E. J. R., Prather, M. J., Mahajan, S., Li, Q., Jones, P. W., Jacob, R. L., Huebler, G. W., Huang, X., Hillman, B. R., Harrop, B. E., Foucar, J. G., Fang, Y., Comeau, D. S., Caldwell, P. M., Bartoletti, T., Balaguru, K., Taylor, M. A., McCoy, R. B., Leung, L. R., and Bader, D. C.: The DOE E3SM model version 2: Overview of the physical model and initial model evaluation, *J. Adv. Model. Earth Sy.*, 14, e2022MS003156, <https://doi.org/10.1029/2022MS003156>, 2022.
- 1910 Good, S. A., Martin, M. J., and Rayner, N. A.: EN4: Quality controlled ocean temperature and salinity profiles and monthly objective analyses with uncertainty estimates, *J. Geophys. Res. Oceans*, 118, 6704–6716, <https://doi.org/10.1002/2013JC009067>, 2013.
- Griffies, S. M.: The Gent-McWilliams skew flux, *J. Phys. Oceanogr.*, 28, 831–841, [https://doi.org/10.1175/1520-0485\(1998\)028%3C0831:TGMSF%3E2.0.CO;2](https://doi.org/10.1175/1520-0485(1998)028%3C0831:TGMSF%3E2.0.CO;2), 1998.
- 1915 Griffies, S. M.: Elements of the Modular Ocean Model (MOM) 5 (2012 release with updates), Technical Report 7, NOAA/Geophysical Fluid Dynamics Laboratory Ocean Group, 2012.
- Griffies, S. M., Gnanadesikan, A., Pacanowski, R. C., Larichev, V., Dukowicz, J. K., and Smith, R. D.: Isonutral diffusion in a z-coordinate ocean model, *J. Phys. Oceanogr.*, 28, 805–830, [https://doi.org/10.1175/1520-0485\(1998\)028%3C0805:IDIAZC%3E2.0.CO;2](https://doi.org/10.1175/1520-0485(1998)028%3C0805:IDIAZC%3E2.0.CO;2), 1998.
- 1920 Griffies, S. M., Gnanadesikan, A., Dixon, K. W., Dunne, J. P., Gerdes, R., Harrison, M. J., Rosati, A., Russell, J. L., Samuels, B. L., Spelman, M. J., Winton, M., and Zhang, R.: Formulation of an ocean model for global climate simulations, *Ocean Sci.*, 1, 45–79, <https://doi.org/10.5194/os-1-45-2005>, 2005.
- 1925 Griffies, S. M., Biastoch, A., Böning, C., Bryan, F., Danabasoglu, G., Chassignet, E. P., England, M. H., Gerdes, R., Haak, H., Hallberg, R. W., Hazeleger, W., Jungclauss, J., Large, W. G., Madec, G., Pirani, A., Samuels, B. L., Scheinert, M., Sen Gupta, A., Severijns, C. A., Simmons, H. L., Treguier, A. M., Winton, M., Yeager, S., and Yin, J.: Coordinated Ocean-ice Reference Experiments (COREs), *Ocean Model.* 26, 1–46, <https://doi.org/10.1016/j.ocemod.2008.08.007>, 2009.
- 1930 Griffies, S. M., Danabasoglu, G., Durack, P. J., Adcroft, A. J., Balaji, V., Böning, C. W., Chassignet, E. P., Curchitser, E., Deshayes, J., Drange, H., Fox-Kemper, B., Gleckler, P. J., Gregory, J. M., Haak, H., Hallberg, R. W., Hewitt, H. T., Holland, D. M., Ilyina, T., Jungclauss, J. H., Komuro, Y., Krasting, J. P., Large, W. G., Marsland, S. J., Masina, S., McDougall, T. J., Nurser, A. J. G., Orr, J. C., Pirani, A., Qiao, F., Stouffer, R. J., Taylor, K. E., Treguier, A. M., Tsujino, H., Uotila, P., Valdivieso, M., Winton, M., and Yeager, S. G.: OMIP contribution to CMIP6: Experimental and diagnostic protocol for the physical component of the Ocean Model Intercomparison Project, *Geosci. Model Dev.*, 9, 3231–3296, <https://doi.org/10.5194/gmd-9-3231-2016>, 2016.
- 1935

- Grooms, I.: Backscatter in energetically-constrained Leith parameterizations, *Ocean Modelling*, 186, 102265, 2023.
- 1940 Guiavarc'h, C., Storkey, D., Blaker, A. T., Blockley, E., Megann, A., Hewitt, H. T., Bell, M. J., Calvert, D., Copsey, D., Sinha, B., Moreton, S., Mathiot, P., and An, B.: GOSI9: UK Global Ocean and Sea Ice configurations, *Geosci. Model Dev.*, 18, 377–403, <https://doi.org/10.5194/gmd-18-377-2025>, 2025.
- 1945 Hallberg, R.: Using a resolution function to regulate parameterizations of oceanic mesoscale eddy effects, *Ocean Model.*, 72, 92–103, <https://doi.org/10.1016/j.ocemod.2013.08.007>, 2013.
- 1950 Held, I. M., Guo, H., Adcroft, A., Dunne, J. P., Horowitz, L. W., Krasting, J., Shevliakova, E., Winton, M., Zhao, M., Bushuk, M., Wittenberg, A. T., Wyman, B., Xiang, B., Zhang, R., Anderson, W., Balaji, V., Donner, L., Dunne, K., Durachta, J., Gauthier, P. P. G., Ginoux, P., Golaz, J.-C., Griffies, S. M., Hallberg, R., Harris, L., Harrison, M., Hurlin, W., John, J., Lin, P., Lin, S.-J., Malyshev, S., Menzel, R., Milly, P. C. D., Ming, Y., Naik, V., Paynter, D., Paulot, F., Rammasswamy, V., Reichl, B., Robinson, T., Rosati, A., Seman, C., Silvers, L. G., Underwood, S., and Zadeh, N.: Structure and performance of GFDL's CM4.0 climate model, *J. Adv. Model. Earth Sy.*, 11, 3691–3727, <https://doi.org/10.1029/2019MS001829>, 2019.
- 1955 Hirschi, J. J.-M., Barnier, B., Boening, C., Biastoch, A., Blaker, A. T., Coward, A., Danilov, S., Drijfhout, S., Getzlaff, K., Griffies, S. M., Hasumi, H., Hewitt, H., Iovino, D., Kawasaki, T., Kiss, A. E., Koldunov, N., Marzocchi, A., Mecking, J. V., Moat, B., Molines, J.-M., Myers, P. G., Penduff, T., Roberts, M., Treguier, A.-M., Sein, D. V., Sidorenko, D., Small, J., Spence, P., Thompson, L., Weijer, W., and Xu, X. (2020), The Atlantic Meridional Overturning Circulation in high resolution models, *J. Geophys. Res. Oceans*, 125, e2019JC015522, <http://dx.doi.org/10.1029/2019JC015522>, 2020.
- 1960 Hirt, C. W., Amsden, A. A., and Cook, J. L.: An arbitrary Lagrangian-Eulerian computing method for all flow speeds, *J. Comput. Phys.*, 135, 203–216, <https://doi.org/10.1006/jcph.1997.5702>, 1997.
- 1965 Huneke, W. G. C., Hogg, A. McC., Dix, M., Bi, D., Sullivan, A., McGregor, S., Holgate, C., O'Farrell, S. P., and Oliveira, M. J. T.: The ACCESS-CM2 climate model with a higher resolution ocean-sea ice component (1/4°), *EGUsphere* [preprint], <https://doi.org/10.5194/egusphere-2025-1006>, 2025.
- 1970 Hunke, E. C. and Dukowicz, J. K.: An elastic–viscous–plastic model for sea ice dynamics, *J. Phys. Oceanogr.*, 27, 1849–1867, 1997.
- Hunke, E. C. and Lipscomb, W. H.: CICE: the Los Alamos Sea Ice Model documentation and software user's manual version 4.1, Technical Report, LA-CC-06-012, 76 pp., available at: <https://github.com/CICE-Consortium/CICE-svn-trunk/releases/tag/cice-4.1>, 2010.
- 1975 Hunke, E. C., Hebert, D. A., and Lecomte, O.: Level-ice melt ponds in the Los Alamos sea ice model, *CICE, Ocean Model.*, 71, 26–42, <https://doi.org/10.1016/j.ocemod.2012.11.008>, 2013.
- 1980 Hunke, E. C., Lipscomb, W. H., Turner, A. K., Jeffery, N., and Elliott, S.: CICE: the Los Alamos Sea Ice Model documentation and software user's manual version 5.1, Technical Report LA-CC-06-012, Los Alamos National Laboratory, Los Alamos, NM 87545, 2015.

- IOC, IHO and BODC: Centenary Edition of the GEBCO Digital Atlas, published on CD-ROM on behalf of the Intergovernmental Oceanographic Commission and the International Hydrographic Organization as part of the General Bathymetric Chart of the Oceans, British Oceanographic Data Centre, Liverpool, UK, 2003.
- 1985 IOC, SCOR, and IAPSO: The international thermodynamic equation of seawater – 2010: Calculation and use of thermodynamic properties, 2010.
- Iovino, D., Masina, S., Storto, A., Cipollone, A., and Stepanov, V. N.: A 1/16° eddy simulation of the global NEMO sea-ice-ocean system, *Geosci. Model Dev.*, 9, 2665–2684, <https://doi.org/10.5194/gmd-9-2665-2016>, 2016.
- 1990 Iovino, D., Fogli, P. G., and Masina, S.: Evaluation of the CMCC global eddy ocean model for the Ocean Model Intercomparison Project (OMIP2), *Geosci. Model Dev.*, 16, 6127–6159, <https://doi.org/10.5194/gmd-16-6127-2023>, 2023.
- Jackett, D. R., McDougall, T. J., Feistel, R., Wright, D. G., and Griffies, S. M.: Algorithms for density, potential temperature, conservative temperature, and the freezing temperature of seawater, *J. Atmos. Oceanic Tech.*, 23, 1709–1728, <http://dx.doi.org/10.1175/JTECH1946.1>, 2006.
- 1995 Jackson, L. C. and Petit, T.: North Atlantic overturning and water mass transformation in CMIP6 models, *Clim. Dyn.*, <https://doi.org/10.1007/s00382-022-06448-1>, 2022.
- 2000 Jackson, L. C., Dubois, C., Forget, G., Haines, K., Harrison, M., Iovino, D., Kohl, A., Mignac, D., Masina, S., Peterson, K. A., Piecuch, C. G., Roberts, C. D., Robson, J., Storto, A., Toyoda, T., Valdivieso, M., Wilson, C., Wang, Y., and Zuo, H.: The mean state and variability of the North Atlantic circulation: A perspective from ocean reanalyses, *J. Geophys. Res.: Oceans*, 124, 9141–9170, <https://doi.org/10.1029/2019JC015210>, 2019.
- 2005 Jackson, L. C., Biastoch, A., Buckley, M. W., Desbruyeres, D., Frajka-Williams, E., Noat, B., and Robson, J.: The evolution of the North Atlantic meridional overturning circulation since 1980. *Nat. Rev. Earth Environment*, <https://doi.org/10.1030/s43017-022-00263-2>, 2022.
- 2010 Jakobsson, M., Mayer, L., Coakley, B., Dowdeswell, J. A., Forbes, S., Fridman, B., Hodnesdal, H., Noormets, R., Pedersen, R., Rebesco, M., Schenke, H. W., Zarayskaya, Y., Accettella, D., Armstrong, A., Anderson, R. M., Bienhoff, P., Camerlenghi, A., Church, I., Edwards, M., Gardner, J. V., Hall, J. K., Hell, B., Hestvik, O., Kristoffersen, Y., Marcussen, C., Mohammad, R., Mosher, D., Nghiem, S. V., Pedrosa, M. T., Travaglini, P. G., and Weatherall, P.: The international bathymetric chart of the Arctic Ocean (IBCAO) Version 3.0. *Geophys. Res. Lett.*, 39, L1260, <https://doi.org/10.1029/2012GL052219>, 2012.
- 2015 Jansen, M. F., Adcroft, A. J., Hallberg, R., and Held, I. M.: Parameterization of eddy fluxes based on a mesoscale energy budget, *Ocean Modelling*, 92, 28–41, <https://doi.org/10.1016/j.ocemod.2015.05.007>, 2015.
- Jayne, S. R.: The impact of abyssal mixing parameterizations in an ocean general circulation model, *J. Phys. Oceanogr.*, 39, 1756–1775, <https://doi.org/10.1175/2009JPO4085.1>, 2009.
- 2020 Jochum, M.: Impact of latitudinal variations in vertical diffusivity on climate simulations, *J. Geophys. Res.*, 114, C01010, <https://doi.org/10.1029/2008JC005030>, 2009.
- Karspeck, A., Stammer, D., Kohl, A., Danabasoglu, G., Balmaseda, M., Smith, D. M., Fujii, Y., Zhang, S., Giese, B., Tsjino, H., and Rosati, A.: Comparison of the Atlantic meridional overturning circulation between 1960 and 2007 in six ocean reanalysis products, *Clim. Dyn.*, 49, 957–982, <https://doi.org/10.1007/s00382-015-2787-7>, 2017.

- 2025 Kenigson, J. S., Adcroft, A., Bachman, S.D., Castruccio, F., Grooms, I., Pegion, P., and Stanley, Z.: Parameterizing the impact of unresolved temperature variability on the large-scale density field: 2. Modeling, *J. Adv. Model. Earth Syst.*, 14, e2021MS002844, 2022.
- 2030 Kiss, A. E., Hogg, A. M., Hannah, N., Boeira Dias, F., Brassington, G. B., Chamberlain, M. A., Chapman, C., Dobrohotoff, P., Domingues, C. M., Duran, E. R., England, M. H., Fiedler, R., Griffies, S. M., Heerdegen, A., Heil, P., Holmes, R. M., Klocker, A., Marsland, S. J., Morrison, A. K., Munroe, J., Nikurashin, M., Oke, P. R., Pilo, G. S., Richet, O., Savita, A., Spence, P., Stewart, K. D., Ward, M. L., Wu, F., and Zhang, X.: ACCESS-OM2 v1.0: A global ocean–sea ice model at three resolutions, *Geosci. Model Dev.*, 13, 401–442, <https://doi.org/10.5194/gmd-13-401-2020>, 2020.
- 2035 Kobayashi, S., Ota, Y., Harada, Y., Ebata, A., Moriya, M., Onoda, H., Onogi, K., Kamahori, H., Kobayashi, C., Endo, H., Miyaoka, K., and Takahashi, K.: The JRA-55 reanalysis: General specifications and basic characteristics, *J. Meteor. Soc. Jpn*, 93, 5–48, <https://doi.org/10.2151/jmsj.2015-001>, 2015.
- 2040 Large, W. G. and Yeager, S. G.: Diurnal to decadal global forcing for ocean and sea-ice models: the data sets and flux climatologies, NCAR Technical Note, Boulder, Colorado, 112 pp., <https://doi.org/10.5065/D6KK98Q6>, 2004.
- Large, W. G. and Yeager, S. G.: The global climatology of an interannually varying air – sea flux data set, *Clim. Dynam.*, 33, 341–364, <https://doi.org/10.1007/s00382-008-0441-3>, 2009.
- 2045 Large, W. G., McWilliams, J. C., and Doney, S. C.: Oceanic vertical mixing: A review and a model with a nonlocal boundary layer parameterization, *Rev. Geophys.*, 32, 363–403, <https://doi.org/10.1029/94RG01872>, 1994.
- Large, W. G., Patton, E. G., and Sullivan, P. P.: The diurnal cycle of entrainment and detrainment in LES of the Southern Ocean driven by observed surface fluxes and waves, *J. Phys. Oceanogr.*, 51, 3253–3278, <https://doi.org/10.1175/JPO-D-20-0308.1>, 2021.
- 2050 Larsen, J. C. and Sanford, T. B.: Florida current volume transports from voltage measurements, *Science*, 227, 302–304, <https://doi.org/10.1126/science.227.4684.302>, 1985.
- Lee, H.-C., Rosati, A., and Spelman, M. J.: Barotropic tidal mixing effects in a coupled climate model: Oceanic conditions in the Northern Atlantic, *Ocean Model.*, 11, 464–477, <http://dx.doi.org/10.1016/j.ocemod.2005.03.003>, 2006.
- 2055 Legg, S., Briegleb, B., Chang, Y., Chassignet, E. P., Danabasoglu, G., Ezer, T., Gordon, A. L., Griffies, S., Hallberg, R., Jackson, L., Large, W., Ozgokmen, T. M., Peters, H., Price, J., Riemenschneider, U., Wu, W., Xu, X., and Yang, J.: Improving oceanic overflow representation in climate models: The gravity current entrainment climate process team, *Bull. Amer. Meteor. Soc.*, 90, 657–670, <https://doi.org/10.1175/2008BAMS2667.1>, 2009.
- 2060 Li, F., Lozier, M. S., and Johns, W. E.: Calculating the meridional volume, heat and freshwater transports from an observing system in the subpolar North Atlantic: Observing system simulation experiment, *J. Atmos. Oceanic Tech.*, 34, 1483–1500, <https://doi.org/10.1175/JTECH-D-16-0247.1>, 2017.
- 2065 Li, F., Lozier, M. S., Danabasoglu, G., Holliday, N. P., Kwon, Y.-O., Romanou, A., Yeager, S. G., and Zhang, R.: Local and downstream relationships between Labrador Sea water volume and North Atlantic meridional overturning circulation variability, *J. Climate*, 32, 3883–3898, <https://doi.org/10.1175/JCLI-D-18-0735.1>, 2019.

- 2070 Li, F., Lozier, M. S., Bacon, S., Bower, A. S., Cunningham, S. A., de Jong, M. F., de Young B., Fraser, N., Fried, N., Han, G., Holliday, N. P., Holte, J., Houpert, L., Inall, M. E., Johns, W. E., Jones, S., Johnson, C., Karstensen, J., Le Bras, I. A., Lherminier, P., Lin, X., Mercier, H., Oltsmanns, M., Pacini, A., Petit, T., Pickart, R. S., Rayner, D., Straneo, F., Thierry, V., Visbeck, M., Yashayaev, I., and Zhou, C.: Subpolar North Atlantic western boundary density anomalies and meridional overturning circulation, *Nat. Comm.*, 12:3002, <https://doi.org/10.1038/s41467-021-23350-2>, 2021.
- 2075 Li, Q., Webb, A., Fox-Kemper, B., Craig, A., Danabasoglu, G., Large, W. G., and Vertenstein, M.: Langmuir mixing effects on global climate: WAVEWATCH III in CESM, *Ocean Model.*, 103, 145–160, <https://doi.org/10.1016/j.ocemod.2015.07.020>, 2016.
- 2080 Li, Y., Liu, H., Ding, M., Lin, P., Yu, Z., Yu, Y., Meng, Y., Li, Y., Jian, X., Jiang, J., Chen, K., Yang, Q., Wang, Y., Zhao, B., Wei, J., Ma, J., Zheng, W., and Wang, P.: Eddy-resolving simulation of CAS-LICOM3 for phase 2 of the Ocean Model Intercomparison Project, *Adv. Atmos. Sci.*, 37, 1067–1080, <https://doi.org/10.1007/s00376-020-0057-z>, 2020.
- Lin, Y.-J., Rose, B. E., and Hwang, Y.-T.: Mean state AMOC affects AMOC weakening through subsurface warming in the Labrador Sea, *J. Clim.*, 36, 3895–3915, <https://doi.org/10.1175/JCLI-D-22-0464>, 2023.
- 2085 Locarnini, R. A., Mishonov, A. V., Antonov, J. I., Boyer, T. P., Garcia, H. E., Baranova, O. K., Zweng, M. M., Paver, C. R., Reagan, J. R., Johnson, D. R., Hamilton, M., and Seidov, D.: *World Ocean Atlas 2013, Vol. 1: Temperature*, NOAA Atlas NESDIS 73, <https://doi.org/10.7289/V55X26VD>, 2013.
- 2090 Locarnini, R. A., Mishonov, A. V., Baranova, O. K., Reagan, J. R., Boyer, T. P., Seidov, D., Wang, Z., Garcia, H. E., Bouchard, C., Cross, S. L., and Paver, C. R.: *World Ocean Atlas 2023, volume 1: Temperature*, 2024.
- 2095 Lovato, T., Peano, D., Butenschön, M., Materia, S., Iovino, D., Scoccimarro, E., Fogli, P. G., Cherchi, A., Bellucci, A., Gualdi, S., and Masina, S.: CMIP6 simulations with the CMCC Earth System Model (CMCC-ESM2), *J. Adv. Model. Earth Sy.*, 14, e2021MS002814, <https://doi.org/10.1029/2021MS002814>, 2022.
- Lozier, M. S.: Overturning in the subpolar North Atlantic: A review, *Philos. Trans. R. Soc. A.*, 381, <https://doi.org/10.1098/rsta.2022.0191>, 2023.
- 2100 Lozier, M. S., Bacon, S., Bower, A. S., Cunningham, S. A., de Jong, M. F., de Steur, L., DeYoung, B., Fischer, J., Gary, S. F., Greenan, B. J. W., Heimbach, P., Holliday, N. P., Houpert, L., Inall, M. E., Johns, W. E., Johnson, H. L., Karstensen, J., Li, F., Lin, X., Mackay, N., Marshall, D. P., Mercier, H., Myers, P. G., Pickart, R. S., Pillar, H. R., Straneo, F., Thierry, V., Weller, R. A., Williams, R. G., Wilson, C., Yang, J., Zhao, J., and Zika, J. D.: Overturning in the Subpolar North Atlantic Program: A new international ocean observing system, *Bull. Amer. Meteor. Soc.*, 98, 737–752, <https://doi.org/10.1175/BAMS-D-16-0057.1>, 2017.
- 2105 Lozier, M. S., Li, F., Bacon, S., Bahr, F., Bower, A. S., Cunningham, S. A., de Jong, M. F., de Steur, L., DeYoung, B., Fischer, J., Gary, S. F., Greenan, B. J. W., Holliday, N. P., Houk, A., Houpert, L., Inall, M. E., Johns, W. E., Johnson, H. L., Johnson, C., Karstensen, J., Koman, G., Le Bras, I. A., Lin, X., Mackay, N., Marshall, D. P., Mercier, H., Oltsmanns, M., Pickart, R. S., Ramsey, A. L., Rayner, D., Straneo, F., Thierry, V., Torres, D. J., Williams, R. G., Wilson, C., Yang, J., Yashayaev, I., and Zhao, J.: A sea change in our view of overturning in the subpolar North Atlantic, *Science*, 363, 516–521, doi: 10.1126/science.aau6592, 2019.

- 2115 Lozier, M. S., Bower, A. S., Furey, H. H., Drouin, K. L., Xu, X., and Zhou, S.: Overflow water pathways in the North Atlantic, *Prog. Oceanogr.*, 208, 102874, <https://doi.org/10.1016/j.pocean.2022.102874>, 2022.
- Lynn, R. J. and Reid, J. L.: Characteristics of circulation of deep and abyssal waters, *Deep-Sea Res.*, 15, 577-598, 1968.
- 2120 Mackallah, C., Chamberlain, M. A., Law, R. M., Dix, M., Ziehn, T., Bi, D., Bodman, R., Brown, J. R., Dobrohotoff, P., Druken, K., Evans, B., Harman, I. N., Hayashida, H., Holmes, R., Kiss, A. E., Lenton, A., Liu, Y., Marsland, S., Meissner, K., Menviel, L., O'Farrell, S., Rashid, H. A., Ridzwan, S., Savita, A., Srbinovsky, J., Sullivan, A., Trenham, C., Vohralik, P. F., Wang, Y.-P., Williams, G., Woodhouse, M. T., and Yeung, N.: ACCESS datasets for CMIP6: Methodology and idealised experiments. *J. Southern Hemisphere Earth Sy. Sci.*, 72, 93–116, <https://doi.org/10.1071/ES21031>, 2022.
- 2125 Madec, G. and Imbard, M.: A global ocean mesh to overcome the North Pole singularity, *Clim. Dyn.*, 12, 381–388, 1996.
- Madec, G. and the NEMO Team: NEMO ocean engine - version 3.6. Note du Pôle de modélisation, Institut Pierre-Simon Laplace, 27, 2016.
- 2130 Madec, G. and System Team: Nemo Ocean Engine - version 4.0.1, Notes du Pole de modelisation de l'Institut Pierre-Simon Laplace (IPSL), 27, <https://doi.org/10.5281/zenodo.3878122>, 2019.
- 2135 Marques, G. M., Shao, A. E., Bachman, S. D., Danabasoglu, G., and Bryan, F. O.: Representing eddy diffusion in the surface boundary layer of ocean models with general vertical coordinates, *J. Adv. Model. Earth Syst.*, 15, e2023MS003751, <https://doi.org/10.1029/2023MS003751>, 2023.
- Marshall, D. P., Maddison, J. R., and Berloff, P. S.: A framework for parameterizing eddy potential vorticity fluxes, *J. Phys. Oceanogr.*, 42, 539–557, <https://doi.org/10.1175/JPO-D-11-048.1>, 2012.
- 2140 Masina, S., Cipollone, A., Iovino, D., Ciliberti, S., Coppini, G., Lecci, R., Creti, S., Palermo, F., Viola, F., Lyubartsev, V., Baordo, F., Trotta, F., and Pinardi, N.: A global ocean eddy forecasting system at 1/16°, in *Advances in operational oceanography: expanding Europe's ocean observing and forecasting capacity. Proceedings of the 9th EuroGOOS International Conference, EuroGOOS, Brussels, Belgium, 3–5 May 2021*, 524–531, <https://doi.org/10.13155/83160>, 2021.
- 2145 Mauritzen, C., Price, J., Sanford, T., and Torres, D.: Circulation and mixing in the Faroese Channels, *Deep-Sea Res. I*, 52, 883–913, <https://doi.org/10.1016/j.dsr.2004.11.018>, 2005.
- McDougall, T. J., and Barker, P. M.: Getting started with TEOS-10 and the Gibbs Seawater (GSW) Oceanographic Toolbox, 28pp., SCOR/IAPSO WG127, ISBN 978-0-646-55621-5, 2011.
- 2150 Meehl, G. A., Goddard, L., Boer, G., Burgman, R., Branstator, G., Cassou, C., Corti, S., Danabasoglu, G., Doblas-Reyes, F., Hawkins, E., Karspeck, A., Kimoto, M., Kumar, A., Matei, D., Mignot, J., Msadek, R., Navarra, A., Pohlmann, H., Rienecker, M., Rosati, A., Schneider, E., Smith, D., Sutton, R., Teng, H., van Oldenborgh, G. J., Vecchi, G., and Yeager, S.: Decadal climate prediction: An update from the trenches, *Bull. Amer. Meteor. Soc.*, 95, 243–267, <https://doi.org/10.1175/BAMS-D-12-00241.1>, 2014.
- 2155

- Megann, A., Blaker, A., Josey, S., New, A., and Sinha, B.: 2021. Mechanisms for late 20th and early 21st century decadal AMOC variability, *J. Geophys. Res.: Oceans*, 126, e2021JC017865, <https://doi.org/10.1029/2021JC017865>, 2021.
- 2160 Meinen, C. S., Baringer, M. O., and Garcia, R. F.: Florida current transport variability: An analysis of annual and longer-period signals, *Deep Sea Research Part I: Oceanographic Res. Papers*, 57, 835–846, <https://doi.org/10.1016/j.dsr.2010.04.001>, 2010.
- 2165 Meinen, C. S., Speich, S., Piola, A. R., Ansorge, I., Campos, E., Kersalé, M., Terre, T., Chidichimo, M. P., Lamont, T., Sato, O. T., Perez, R. C., Valla, D., van den Berg, M., Le Henaff, M., Dong, S., and Garzoli, S.: Meridional overturning circulation transport variability at 34.5°S during 2009–2017: Baroclinic and barotropic flows and the dueling influence of the boundaries, *Geophys. Res. Lett.*, 45, 4180–4188, <https://doi.org/10.1029/2018GL077408>, 2018.
- 2170 Menary, M. B., Jackson, L. C., and Lozier, M. S.: Reconciling the relationship between the AMOC and Labrador Sea in OSNAP observations and climate models, *Geophys. Res. Lett.*, 47, e2020GL089793, <https://doi.org/10.1029/2020GL089793>, 2020.
- Morlighem, M.: MEaSUREs BedMachine Antarctica (NSIDC-0756, Version 3), NASA National Snow and Ice Data Center Distributed Active Archive Center, <https://doi.org/10.5067/FPSU0V1MWUB6>, 2022.
- 2175 Msadek, R., Dixon, K. W., Delworth, T. L., and Hurlin, W.: Assessing the predictability of the Atlantic meridional overturning circulation and associated fingerprints, *Geophys. Res. Lett.*, 37, L19608, <https://doi.org/10.1029/2010GL044517>, 2010.
- Murray, R. J.: Explicit generation of orthogonal grids for ocean models. *J. Comput. Phys.*, 126(2), 251–273, <http://dx.doi.org/10.1006/jcph.1996.0136>, 1996.
- 2180 NOAA: available at: <https://www.ngdc.noaa.gov/mgg/global/etopo2.html> (last access: 6 August 2018), 2006.
- Ortega, P., Robson, J. I., Menary, M., Sutton, R. T., Blaker, A., Germe, A., Hirschi, J. J.-M., Sinha, B., Hermanson, L., and Yeager, S.: Labrador Sea subsurface density as a precursor of multidecadal variability in the North Atlantic: A multi-model study, *Earth Syst. Dynam.*, 12, 419–438, <https://doi.org/10.5194/esd-12-419-2021>, 2021.
- 2185 Pacanowski, R. C., and Gnanadesikan, A.: Transient response in a z-level ocean model that resolves topography with partial cells, *Monthly Weather Rev.*, 126, 3248–3270, [http://dx.doi.org/10.1175/1520-0493\(1998\)126<3248:TRIAZL>2.0.CO;2](http://dx.doi.org/10.1175/1520-0493(1998)126<3248:TRIAZL>2.0.CO;2), 1998.
- 2190 Petersen, M. R., Jacobsen, D. W., Ringler, T. D., Hecht, M. W., and Maltrud, M.E.: Evaluation of the arbitrary Lagrangian–Eulerian vertical coordinate method in the MPAS-Ocean model, *Ocean Model.*, 86, 93–113, 2015.
- Petit, T., Lozier, M. S., Josey, S. A., and Cunningham, S. A.: Atlantic deep water formation occurs primarily in the Iceland Basin and Irminger Sea by local buoyancy forcing, *Geophys. Res. Lett.*, 47, e2020GL091028, <https://doi.org/10.1029/2020GL091028>, 2020.
- 2195 Petit, T., Lozier, M. S., Rühls, S., Handmann, P., and Biastoch, A.: Propagation and transformation of upper North Atlantic Deep Water from the subpolar gyre to 26.5°N, *J. Geophys. Res. Oceans*, 128, e2023JC019726, <https://doi.org/10.1029/2023JC019726>, 2023.
- Pickart, R. S. and Spall, M. A.: Impact of Labrador Sea convection on the North Atlantic meridional overturning circulation, *J. Phys. Oceanogr.*, 37, 2207–2227, <https://doi.org/10.1175/JPO3178.1>, 2007.

- 2200 Reagan, J. R., Seidov, D., Wang, Z., Dukhovskoy, D., Boyer, T. P., Locarnini, R. A., Baranova, O. K., Mishonov, A. V., Garcia, H. E., Bouchard, C., and Cross, S. L.: World Ocean Atlas 2023, volume 2: Salinity, 2024.
- Redi, M. H.: Oceanic isopycnal mixing by coordinate rotation, *J. Phys. Oceanogr.*, 12, 1154–1158, [https://doi.org/10.1175/1520-0485\(1982\)012<1154:OIMBCR>2.0.CO;2](https://doi.org/10.1175/1520-0485(1982)012<1154:OIMBCR>2.0.CO;2), 1982.
- 2205 Reichl, B. G. and Hallberg, R.: A simplified energetics based planetary boundary layer (ePBL) approach for ocean climate simulations, *Ocean Model.*, 132, 112–129, <https://doi.org/10.1016/j.ocemod.2018.10.004>, 2018.
- Riemenschneider, U. and Legg, S.: Regional simulations of the Faroe Bank Channel overflow in a level model, *Ocean Model.*, 17, 93–122, <https://doi.org/10.1016/j.ocemod.2007.01.003>,
2210 2007.
- Rousset, C., Vancoppenolle, M., Madec, G., Fichefet, T., Flavoni, S., Barthélemy, A., Benshila, R., Chanut, J., Levy, C., Masson, S., and Vivier, F.: The Louvain-La-Neuve sea ice model LIM3.6: Global and regional capabilities, *Geosci. Model Dev.*, 8, 2991–3005, <https://doi.org/10.5194/gmd-8-2991-2015>, 2015.
- 2215 Rühs, S., Oliver, E., Biastoch, A., Böning, C. W., Dowd, M., Getzlaff, K., and Myers, P. G.: Changing spatial patterns of deep convection in the subpolar North Atlantic, *J. Geophys. Res.*, 126, e2021JC017245, <https://doi.org/https://doi.org/10.1029/2021JC017245>, 2021.
- Send, U., Lankhorst, M., and Kanzow, T.: Observation of decadal change in the Atlantic meridional overturning circulation using 10 years of continuous transport data, *Geophys. Res. Lett.*, 38, 24606, <https://doi.org/10.1029/2011GL049801>, 2011.
- 2220 Shao, A. E., Adcroft, A., Hallberg, R., and Griffies, S. M.: A general-coordinate, nonlocal neutral diffusion operator, *J. Adv. Model. Earth Syst.*, 12, e2019MS001992, <https://doi.org/10.1029/2019MS001992>, 2020.
- Shchepetkin, A. F.: An adaptive, Courant-number-dependent implicit scheme for vertical advection in oceanic modeling, *Ocean Model.*, 91, 38–69, <https://doi.org/10.1016/j.ocemod.2015.03.006>, 2015.
- 2225 Shchepetkin, A. F. and McWilliams, J. C.: A method for computing horizontal pressure-gradient force in an oceanic model with a nonaligned vertical coordinate, *J. Geophys. Res.*, 108(C3), 3090, doi:10.1029/2001JC001047, 2003.
- 2230 Sidorenko, D., Danilov, S., Fofonova, V., Cabos, W., Koldunov, N., Scholz, P., Sein, D. V., and Wang, Q.: AMOC, water mass transformations, and their responses to changing resolution in the Finite-Volume Sea Ice-Ocean Model, *J. Adv. Model. Earth Syst.*, 12, e2020MS002317, <https://doi.org/10.1029/2020MS002317>, 2020.
- 2235 Sidorenko, D., Danilov, S., Streffing, J., Fofonova, V., Goessling, H. F., Scholz, P., Wang, Q., Androsov, A., Cabos, W., Juricke, S., Koldunov, N., Rackow, T., Sein, D. V., and Jung, T.: AMOC variability and watermass transformations in the AWI climate model, *J. Adv. Model. Earth Syst.*, 13, e2021MS002582, <https://doi.org/10.1029/2021MS002582>, 2021.
- Simmons, H. L., Jayne, S. R., Laurent, L. C. S., and Weaver, A. J.: Tidally driven mixing in a numerical model of the ocean general circulation, *Ocean Model.*, 6, 245–263, [https://doi.org/10.1016/S1463-5003\(03\)00011-8](https://doi.org/10.1016/S1463-5003(03)00011-8), 2004.
- 2240 Small, R. J., Bacmeister, J., Bailey, D., Baker, A., Bishop, S., Bryan, F., Caron, J., Dennis, J., Gent, P., Hsu, H., Jochum, M., Lawrence, D., Muñoz, E., DiNezio, P., Scheitlin, T., Tomas, R., Tribbia, J., Tseng, Y., and Vertenstein, M.: A new synoptic scale resolving global climate

- simulation using the Community Earth System Model, *J. Adv. Model. Earth Syst.*, 6, 1065–1094, <https://doi.org/10.1002/2014MS000363>, 2014.
- 2245 Smith, K., Barthel, A. M., Conlon, L. M., Van Roekel, L. P., Bartoletti, A., Golez, J. C., Zhang, C., Begeman, C. B., Benedict, J. J., Bisht, G., and Feng, Y.: The DOE E3SM version 2.1: Overview and assessment of the impacts of parameterized ocean submesoscales, *Geosci. Model Dev. Discussions*, 1–38, 2024.
- 2250 Smith, R., Jones, P., Briegleb, B., Bryan, F., Danabasoglu, G., Dennis, J., Dukowicz, J., Eden, C., Fox-Kemper, B., Gent, P., Hecht, M., Jayne, S., Jochum, M., Large, W., Maltrud, M., Norton, N., Peacock, S., Vertenstein, M., and Yeager, S.: The parallel ocean program (POP) reference manual: Ocean component of the community climate system model (CCSM) and Community Earth System Model (CESM), LANL Tech. Rep. LAUR-01853, 141 pp., 2010.
- 2255 Solodoch, A., Stewart, A. L., Hogg, A. M., Morrison, A. K., Kiss, A. E., Thompson, A. F., Purkey, S. G., and Cimoli, L.: How does Antarctic Bottom Water cross the Southern Ocean? *Geophys. Res. Lett.*, 49, e2021GL097211, <https://doi.org/10.1029/2021GL097211>, 2022.
- Spall, M. A.: Boundary currents and watermass transformation in marginal seas, *J. Phys. Oceanogr.*, 34, 1197–1213, 2004.
- 2260 Stanley, Z., Grooms, I., Kleiber, W., Bachman, S. D., Castruccio, F., and Adcroft, A.: Parameterizing the impact of unresolved temperature variability on the large-scale density field: Part 1. Theory, *J. Adv. Model. Earth Syst.*, 12, e2020MS002185, 2020.
- Stewart, K. D., Hogg, A. M., Griffies, S. M., Heerdegen, A. P., Ward, M. L., Spence, P., and England, M. H.: Vertical resolution of baroclinic modes in global ocean models, *Ocean Model.*, 113, 50–65, 2017.
- 2265 Straneo, F.: On the connection between dense water formation, overturning, and poleward heat transport in a convective basin, *J. Phys. Oceanogr.*, 36, 1822–1840, <https://doi.org/10.1175/JPO2932.1>, 2006.
- Sun, Q., Whitney, M. M., Bryan, F. O., and Tseng, Y.: Assessing the skill of the improved treatment of riverine freshwater in the Community Earth System Model (CESM) relative to a new salinity climatology, *J. Adv. Model. Earth Syst.*, 11, 1189–1206, <https://doi.org/10.1029/2018MS001349>, 2019.
- 2270 Sutton, R. T., McCarthy, G. D., Robson, J., Sinha, B., Archibald, A. T., and Gray, L. J.: Atlantic multidecadal variability and the U.K. ACSIS program, *Bull. Amer. Meteor. Soc.*, 99, 415–425, <https://doi.org/10.1175/BAMS-D-16-0266.1>, 2018.
- 2275 Suzuki, T., Yamazaki, D., Tsujino, H., Komuro, Y., Nakano, H., and Urakawa, S.: A dataset of continental river discharge based on JRA-55 for use in a global ocean circulation model, *J. Oceanogr.*, 74, 421–429, <https://doi.org/10.1007/s10872-017-0458-5>, 2018.
- Teague, W. J., Carron, M. J., and Hogan, P. J.: A comparison between the Generalized Digital Environmental Model and Levitus climatologies, *J. Geophys. Res.*, 95, 7167–7183, <https://doi.org/10.1029/jc095ic05p07167>, 1990.
- 2280 Timmermann, R., Goosse, H., Madec, G., Fichet, T., Etche, C., and Dulière, V.: On the representation of high latitude processes in the ORCA-LIM global coupled sea ice-ocean model, *Ocean Model.*, 8, 175–201, 2005.
- 2285 Toole, J. M., Curry, R. G., Joyce, T. M., McCartney, M., and Peña-Molino, B.: Transport of the North Atlantic deep western boundary current about 39°N, 70°W: 2004-2008, *Deep Sea Res.*

Part II: Topical Studies in Oceanography, 58, 1768–1780,
<https://doi.org/10.1016/j.dsr2.2010.10.058>, 2011.

- 2290 Tozer, B., Sandwell, D. T., Smith, W. H. F., Olson, C., Beale, J. R., and Wessel, P.: Global bathymetry and topography at 15 arc sec: SRTM15+, *Earth and Space Science*, 6, <https://doi.org/10.1029/2019EA000658>, 2019.
- 2295 Treguier, A. M., de Boyer Montegut, C., Bozec, A., Chassignet, E. P., Fox-Kemper, B., Hogg, A. M., Iovino, D., Kiss, A. E., Sommer, J. L., Li, Y., Lin, P., Lique, C., Liu, H., Serazin, G., Sidorenko, D., Wang, Q., Xu, X., and Yeager, S.: The mixed-layer depth in the ocean model intercomparison project (OMIP): Impact of resolving mesoscale eddies. *Geosci. Model Dev.*, 16, 3849–3872, <https://doi.org/10.5194/gmd-16-3849-2023>, 2023.
- 2300 Tsujino, H., Urakawa, S., Nakano, H., Small, R. J., Kim, W. M., Yeager, S. G., Danabasoglu, G., Suzuki, T., Bamber, J. L., Bentsen, M., Böning, C. W., Bozec, A., Chassignet, E. P., Curchitser, E., Dias, F. B., Durack, P. J., Griffies, S. M., Harada, Y., Ilicak, M., Josey, S. A., Kobayashi, C., Kobayashi, S., Komuro, Y., Large, W. G., Sommer, J. L., Marsland, S. J., Masina, S., Scheinert, M., Tomita, H., Valdivieso, M., and Yamazaki, D.: JRA-55 based surface dataset for driving ocean - sea-ice models (JRA55-do), *Ocean Model.*, 130, 79–139, <http://dx.doi.org/10.1016/j.ocemod.2018.07.002>, 2018.
- 2305 Tsujino, H., Urakawa, L. S., Griffies, S. M., Danabasoglu, G., Adcroft, A. J., Amaral, A. E., Arsouze, T., Bentsen, M., Bernardello, R., Böning, C. W., Bozec, A., Chassignet, E. P., Danilov, S., Dussin, R., Exarchou, E., Fogli, P. G., Fox-Kemper, B., Guo, C., Ilicak, M., Iovino, D., Kim, W. M., Koldunov, N., Lapin, V., Li, Y., Lin, P., Lindsay, K., Liu, H., Long, M. C., Komuro, Y., Marsland, S. J., Masina, S., Nummelin, A., Rieck, J. K., Ruprich-Robert, Y., Scheinert, M., Sicardi, V., Sidorenko, D., Suzuki, T., Tatebe, H., Wang, Q., Yeager, S. G., and Yu, Z.: Evaluation of global ocean-sea model simulations based on the experimental protocols of the Ocean Model Intercomparison Project phase 2 (OMIP-2), *Geosci. Model Dev.*, 13, 3643–3708, <https://doi.org/10.5194/gmd-13-3643-2020>, 2020.
- 2310 Turner, A. K. and Hunke, E. C.: Impacts of a mushy-layer thermodynamic approach in global sea-ice simulations using the CICE sea-ice model, *J. Geophys. Res.-Oceans*, 120, 1253–1275, <https://doi.org/10.1002/2014JC010358>, 2015.
- Uotila, P., Iovino, D., Vancoppenolle, M., Lensu, M., and Rousset, C.: Comparing sea ice, hydrography and circulation between NEMO3.6 LIM3 and LIM2, *Geosci. Model Dev.*, 10, 1009–1031, <https://doi.org/10.5194/gmd-10-1009-2017>, 2017.
- 2320 Valcke, S., Craig, T., and Coquart, L.: OASIS3-MCT User Guide: OASIS3-MCT 2.0. CERFACS/CNRS SUC URA N°1875, CERFACS TR/CMGC/13/17, CERFACS/CNRS, 2013.
- van Westen, R. M., Kliphuis, M., and Dijkstra, H. A.: Physics-based early warning signal shows that AMOC is on tipping course, *Sci. Adv.*, 10(6), eadk1189, <https://doi.org/10.1126/sciadv.adk1189>, 2024.
- 2325 Wang, Q., Shu, Q., Bozec, A., Chassignet, E. P., Fogli, P. G., Fox-Kemper, B., Hogg, A. M., Iovino, D., Kiss, A. E., Koldunov, N., Le Sommer, J., Li, Y., Lin, P., Liu, H., Polyakov, I., Scholz, P., Sidorenko, D., Wang, S., and Xu, X.: Impact of increased resolution on Arctic Ocean simulations in Ocean Model Intercomparison Project phase 2 (OMIP-2), *Geosci. Model Dev.*, 17, 347–379. <https://doi.org/10.5194/gmd-17-347-2024>, 2024.

- 2330 Weatherall, P., Marks, K. M., Jakobsson, M., Schmitt, T., Tani, S., Arndt, J. E., Rovere, M., Chayes, D., Ferrini, V., and Wigley, R.: A new digital bathymetric model of the world's oceans. *Earth and Space Science*, 2, 331-345, <https://doi.org/10.1002/2015EA000107>, 2015.
- Weijer, W., Cheng, W., Garuba, O. A., Hu, A., and Nadiga, B. T.: CMIP6 models predict significant 21st century decline of the Atlantic Meridional Overturning Circulation, *Geophys. Res. Lett.*, 47, e2019GL086075. <https://doi.org/10.1029/2019GL086075>, 2020.
- 2335 Wright, D. G.: An equation of state for use in ocean models: Eckart's formula revisited, *J. Atm. Ocean. Tech.*, 14, 735–740, [https://doi.org/10.1175/1520-0426\(1997\)014<0735:AEOSFU>2.0.CO;2](https://doi.org/10.1175/1520-0426(1997)014<0735:AEOSFU>2.0.CO;2), 1997.
- Xu, X., Chassignet, E. P., and Wang, F.: On the variability of the Atlantic meridional overturning circulation transports in coupled CMIP5 simulations, *Clim. Dyn.*, <https://doi.org/10.1007/s00382-018-4529-0>.
- 2340 Xu, X., Chassignet, E. P., Firing, Y. L., and Donohue, K.: Antarctic Circumpolar Current transport through Drake Passage: What can we learn from comparing high-resolution model results to observations? *J. Geophys. Res. Oceans*, 125, e2020JC016365, <https://doi.org/10.1029/2020JC016365>, 2020.
- 2345 Xu, X., Chassignet, E. P., Dong, S., and Baringer, M. O.: Transport structure of the South Atlantic Ocean derived from a high-resolution numerical model and observations, *Front. Mar. Sci.*, 9, 811398, <https://doi.org/10.3389/fmars.2022.811398>, 2022.
- Xu, X., Chassignet, E. P., and Wallcraft, A. J.: Impact of vertical resolution on representing baroclinic modes and water mass distribution in the North Atlantic, *Ocean Model.*, 186, <https://doi.org/10.1016/j.ocemod.2023.102261>, 2023.
- 2350 Yang, J., Li, J., and An, Q.: Deep Atlantic multidecadal variability, *Geophys. Res. Lett.*, 51, e2023GL106367, <http://dx.doi.org/10.1029/2023GL106367>, 2024.
- Yeager, S. and Danabasoglu, G.: The origins of late 20th century variations in the large-scale North Atlantic circulation, *J. Climate*, 27, 3222–3247, <https://doi.org/10.1175/JCLI-D-13-00125.1>, 2014.
- 2355 Yeager, S., Castruccio, F., Chang, P., Danabasoglu, G., Maroon, E., Small, J., Wang, H., Wu, L., and Zhang, S.: An outsized role for the Labrador Sea in the multidecadal variability of the Atlantic overturning circulation, *Sci. Adv.*, 7, eabh3592, <https://doi.org/10.1126/sciadv.abh3592>, 2021.
- 2360 Zalesak, S. T.: Fully multidimensional flux corrected transport algorithms for fluids, *J. Comput. Phys.*, 31, 335–362, 1979.
- Zhang, R. and Thomas, M.: Horizontal circulation across density surfaces contributes substantially to the long-term mean northern Atlantic meridional overturning circulation, *Comm. Earth Environment*, 2:112, <https://doi.org/10.1038/s43247-021-00182-y>, 2021.
- 2365 Zhang, R., Sutton, R., Danabasoglu, G., Kwon, Y.-O., Marsh, R., Yeager, S. G., Amrhein, D. E., and Little, C. M.: A review of the role of Atlantic meridional overturning circulation in Atlantic multidecadal variability and associated climate impacts, *Rev. Geophys.*, 57, 316–375, <https://doi.org/10.1029/2019RG000644>, 2019.
- 2370 Zhao, A., Robson, J., Sutton, R., Lai, M. W. K., Mecking, J. V., Yeager, S., and Petit, T.: Large diversity in AMOC variability across NEMO-based climate models, *Clim. Dyn.*, 62, 3355–3374, <https://doi.org/10.1007/s00382-023-07069-y>, 2024.

2375

Zou, S., Lozier, M. S., Li, F., Abernathey, R., and Jackson, L.: Density-compensated overturning in the Labrador Sea, *Nat. Geosci.*, 13, 121–126, <https://doi.org/10.1038/s41561-019-0517-1>, 2020.

Zweng, M., Reagan, J., Antonov, J., Locarnini, R., Mishonov, A., Boyer, T., Garcia, H., Baranova, O., Johnson, D., Seidov, D., and Biddle, M.: *World Ocean Atlas 2013, Vol. 2: Salinity*, NOAA Atlas NESDIS 74, 39 pp., <https://doi.org/10.7289/V5251G4D>, 2013.